Relationship between plastic flow, microcracking and solution-precipitation processes in coarse-grained rocksalt: An experimental study

By Dagmar A.S. Smit

Student number: 4141067

Master student, Utrecht University, The Netherlands

Final version: 29 January 2020

First supervisor: Prof. Dr. Chris J. Spiers

Second supervisor: Dr. Suzanne J.T. Hangx

Table of Contents

Abstract

Salt caverns have the potential to be the host rock for geological storage or they must be abandoned after production. These salt caverns always contain brine after solution mining. The stress-state of the salt caverns changes during the construction of the cavern, during the active cyclic filling and depleting of the cavern for energy storage and after abandonment. The developed effective stresses can be low enough to allow for semi-brittle deformation (plastic flow with microcracking) and/or hydrofracturing. However, little is known about what the effects of brine penetration into dilated rocksalt will be on the rates and mechanisms of plastic flow, solution-precipitation and microcracking. To this extent, triaxial and confined compression experiments were performed on coarse-grained Zechstein salt; solution mined in the Netherlands. The experiments were performed at room temperature and after loading the samples, and the corresponding dilation, dry and wet (including the injection of saturated brine) stress-relaxation followed. The results showed that the stress exponent of dry stress-relaxation phase is noticeably higher (n=9-35); implying dislocation glide; than measured during wet stress-relaxation, in which it decreases to ±3. The latter suggests a change in dominant deformation mechanism from dislocation glide to dynamic recrystallization. Microstructural evidence indicates that diffusive mass transfer processes like recrystallization are affected by the presence of the cracks. The major rheological weakening when saturated brine is present in dilated rocksalt can be explained by various factors: subcritical crack growth, activated dynamic recrystallization and the impact of microcracks on stress enhancement and enhanced pressure solution creep rate. The results of the study imply that microcracking and the geochemical environment must be taken into account when predicting the occurrence of cavern instability (i.e. crack growth), identifying the damage zones around well bores and modelling the formation of a sealing salt plug for well abandonment.

Key words: Zechstein rocksalt, microcracking, brine, stress-relaxation, recrystallization, pressure solution, well abandonment

1   Introduction

Salt domes are often mined by solution mining, in which fresh water is pumped into the ground, dissolving salt minerals and subsequently pumped out as saturated 'brine'. This process creates large caverns in the salt domes, which must be abandoned after production has finished. Through creation of these caverns, salt formations have the potential to be the host rock for geological storage of CO_2, natural gas (and other hydrocarbons) and waste materials (Hunsche & Hampel, 1999; Langer, 1999) (Figure 1). Also, energy may be stored in these caverns in the form of compressed air or hydrogen fuel ('green hydrogen'), which originates from renewable energy sources like solar, wind and/or tidal energy (Hou et al., 2010). Apart of the potential of salt caverns to serve as energy storage and that some caverns have to be abandonment after salt production, rocksalt is often the caprock of hydrocarbons. After gas/oil production the wells need to be sealed to avoid any leakage of the gas and oil. Rocksalt as caprock can serve as a natural plug due to the high sealing capacity of rocksalt. The high sealing capacity of such caverns is expected due to the salt's low porosity (generally lower than 1%) and permeability (below 10^{-20} m^2) and rheological properties, specifically its low plastic flow strength, hence ductile rather than brittle behavior, and its high solubility and rapid reaction kinetics aiding diffusive mass transfer processes, which may drive self-healing (Koelemeijer et al., 2012; Langer, 1999; Peach & Spiers, 1996; Popp et al., 2001; Silberschmidt & Silberschmidt, 2000; Urai et al., 2008).
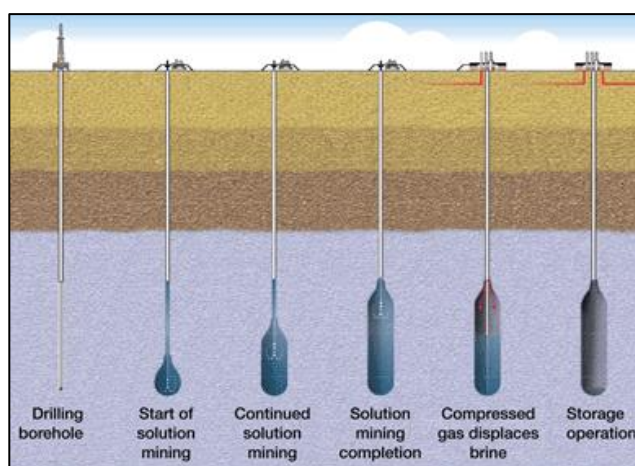

Figure 1: The development of salt caverns made by solution mining and subsequently these caverns are used for geological storage (taken from Lux (2009)).

All of the mentioned potentials of rocksalt cause a change in stress state of the rocksalt during construction of the cavern, well bore placement, production, storage and/or abandonment. During the development of a salt cavern and placement of a wellbore, the mean stress decreases and therefore the deviatoric stress (principal stresses minus mean stress) increases in the walls and roofs of the caverns and at the periphery of the wellbores (Alkan et al., 2007). If the deviatoric stress is much larger than the mean stress, semi-brittle deformation develops (plastic flow with microcracking along grain boundaries and within the grains). This leads to rocksalt with a higher porosity and permeability around the salt cavern and the wellbore, known as the damage zone (Hou, 2003). This effect can be amplified if the salt cavern is filled with gas or brine as they affect the stress state by changing the effective stress. The effective stress is the total stress minus the pore fluid pressure ($\sigma_{eff} = \sigma - P_f$), resulting in an extra decrease in the effective mean stress. Therefore, the stress state of the salt caverns also changes with the cyclic filling and depleting of the caverns with gas, e.g. hydrogen gas or pressed air, for energy storage. This leads in a constant increase and decrease in pore fluid pressure of a few MPa's (Kim et al., 2012). Note that there will always be a background pore fluid pressure when discussing energy storage as the reservoir is not completely depleted in-between cycles. Before energy storage is possible, the solution-mined cavern must be de-brined to make space for the gas and there will always be some brine left in the cavern after de-brining. During cycling of dry gas for energy storage, the brine can evaporate into the dry gas and slowly the cavern will become completely dry. This will stop diffusive mass transfer processes as the transfer medium is no longer present.

The pore pressure in the cavern can also increase by the warming up of the fluid and cavern convergence (Bérest & Brouard, 2003). The effect of the two specified mechanisms depend on the cavern shape and volume, its depth, the thermal diffusion and the temperature difference between the rocksalt and the pore fluid. The temperature effect of heating up brine can be 1 MPa extra pressure per 1°C. Furthermore, solution-mined caverns decrease in volume due to salt creep driven by the difference in stress between the salt and the pore fluid pressure. The decreasing cavern volume, and thereby volume occupied by the fluid (in this case saturated brine), enhances the pressure of the pore fluid. If the pore pressure exceeds the horizontal stress (the minimum principal stress), hydrofracturing can follow (Bérest & Brouard, 2003). This is likely to happen in the roof of the cavern as the hydrostatic pressure is lower at the top of the cavern compared to the bottom. If brine is present during hydrofracturing, it will penetrate the cracks and it can act as a transfer medium for diffusive mass transfer processes. The constant convergence of the salt cavern and the availability of a transfer medium results in a competition between crack propagation and crack growth in the cracked roof. Hydrofracturing strongly decreases the sealing capacity of the rocksalt and thereby leads to leakage of the pore fluid. The possible effect of these (micro)cracks on the type of creep of the salt is generally neglected in creep laws and thereby also in modelling of the creeping salt around wellbores e.g. by Orlic et al. (2019). Modelling often assumes intact rocksalt along the wellbore or volume-constant deformation, which is not representable of the behavior of the damage zone around the wellbore (Hou, 2003). Despite this, it is still unknown what the effects of saturated brine penetration into dilated rocksalt will be on the rates and mechanisms of solution-precipitation, plastic flow, crack growth and/or healing.

It is well known that naturally deformed, fine-grained salt rock deforms by intergranular pressure solution when a saturated solution phase is present (Hickman & Evans, 1991; Spiers et al., 1990; van Noort et al., 2008), even in very small amounts (5 ppm) (Ter Heege et al., 2005b), alongside dislocation plasticity (Carter & Hansen, 1983; Urai et al., 2008; Visser et al., 2012) and (fluid-assisted) dynamic grain boundary migration (Peach et al., 2001; Ter Heege et al., 2005a). The relative influence of these mechanisms relies upon various parameters such as temperature, grain size, confining pressure, water content and solid solution impurities (Urai et al., 2008). Nevertheless, solution-precipitation processes have not been investigated for coarse-grained, dilated natural salt such as the Permian Zechstein salt, which is solution mined in the Netherlands on a large scale. After salt production has been completed, the created salt caverns are a key candidate for energy storage or must be abandoned in the near future. Therefore, the dominant mechanism(s) of creep of dilated rocksalt filled with saturated brine must be understood sufficiently. Under natural conditions, for settings such as caverns and boreholes, natural creep strain rates can range from 10^{-8}-10^{-15} s^{-1} (Jackson & Talbot, 1986), which are difficult to achieve in the laboratory due to the limitations in resolution of the equipment and the effect of temperature fluctuations on the stiffness of the machines. The latter will influence the displacement data and thereby the strain rate of the experiment. According to Rutter et al. (1978), the in-situ strain rates that can be obtained by stress-relaxation experiments, is limited to 10^{-10} s^{-1}, where the applied stress is able to relax over the duration of the experiment at a near-constant load-point position. For natural halite, plastic flow is dominant at high strain rates and high stresses, while solution-precipitation processes like pressure solution take over at lower stresses and strain rates (Muhammad, 2015), but this is not tested including the effect of saturated brine on dilated natural coarse-grained rocksalt.

1.1 Theoretical background: diffusive mass transfer mechanisms in cracked rocksalt

To avoid any leakage out of the salt caverns, it is important to understand what processes can influence the porosity and permeability (i.e. sealing) of rocksalt and if it leads to stable (crack healing) or unstable behavior (crack propagation). Houben et al. (2013) summarizes three different physical mechanisms that can control crack healing and potentially sealing: (1) mechanical healing by pressure solution, plastic flow or elastic deformation; (2) crack healing by recrystallization and (3) surface-energy driven diffusive mass transfer. Under conditions of long-term deformation of natural rocksalt, low strain rates, low stresses and the availability of water, it has been established that diffusive mass transfer processes like fluid assisted dynamic recrystallization, surface energy driven crack healing and pressure solution are the principal deformation processes that control the flow and transport properties of rocksalt (Urai & Spiers, 2007). To investigate the interaction between mechanical behavior and healing processes in cracked natural rocksalt, it is important to understand which of the diffusive mass transfer processes is dominant. In other words which driving force in the Gibbs equilibrium condition equation (Gibbs & Bumstead, 1906; Heidug, 1991) is the largest and thereby releases the most energy:

$$\mu = f + \sigma_n + \frac{2\gamma}{r} \qquad (1)$$

where the chemical potential μ driving dissolution-precipitation is written in [J/m³]; f is Helmholtz energy in the same units, σ_n is the normal stress [Pa], γ is interfacial energy [J/m²] and r is the radius of curvature of the salt/brine interface at any point [m]. f, σ_n and $\frac{2\gamma}{r}$ can respectively be linked as the driving forces for grain boundary migration/recrystallization, pressure solution and diffusive crack healing.

Dynamic recrystallization has two end-member mechanisms: rotational and migrational recrystallization. Recrystallization includes both dislocation and diffusion creep (Ter Heege et al., 2005a), which are both driven by a difference in Helmholtz energy between grains, Δf. A change in Helmholtz energy can be related to subgrains, dislocations, elastic energy, point defects and/or grain boundary curvature, which results in the high energy grains (old and deformed) be 'eaten up' by the low energy grains (strain free) and/or grain nucleation by grain dissection by migrating boundaries. This interplay between grain growth and grain reduction by nucleation is recognized as a recovery process. The solid-state deformation includes dislocation plasticity at dry conditions resulting in polygonization due to the continuous misorientation of the subgrains. At wet conditions dynamic recrystallization is enhanced by the availability of fluid, which allows for fast diffusional transfer of the salt through the fluid film (Peach et al., 2001; Ter Heege et al., 2005a). The thickness of the fluid film will affect the relative abundance of grain boundary migration in the rock, where more narrow fluid films enhance the importance of grain boundary migration. In wet samples the migration process is recognizable by grain with irregular shapes, serrated and/or bulging boundaries (Trimby et al., 2000). Fluid assisted dynamic recrystallization (FADRX) is important when the confining pressure is high enough to prevent dilation and works against work hardening, while at lower confining pressures (<6.5 MPa at 150°C) the dilation and wide cracks allows intergranular H_2O to escape leading to more work hardening and inhibiting FADRX (Peach et al., 2001). In natural salt rock, which is wet, FADRX leads to grain boundary migration that overgrows the fluid filled cracks. This results in sub-spherical fluid inclusions located at the former grain boundaries (Figure 2a).

Pressure solution is one of the most important deformation mechanisms operating in wet salt at low temperature and low strain rates, which can be directly related to geological storage in rocksalt (Spiers et al., 1990). Pressure solution is, like recrystallization, fluid enhanced (i.e. grain boundary

diffusional creep) (Spiers et al., 1990; Urai et al., 1986). It involves both diffusion and interfacial reactions: dissolution at grain boundary interfaces due to a higher normal stress σ_n at the grain boundary contact relative to the unstressed pore wall area. The dissolved material is transferred via a fluid medium (island channel or absorbed film) to the area with lower normal stress (the pore walls), where it precipitates (Schutjens & Spiers, 1999; Spiers et al., 1990; Zhang & Spiers, 2005) (Figure 2b). The difference in chemical potential between the areas is the driving force for the dissolution, diffusion and precipitation. Pressure solution can result in healing of the cracks by mechanical closure and volumetric compaction and thereby reducing the porosity and permeability. This solution-precipitation process is recognizable at microscale by grain-to-grain indentations, grain boundary sliding, overgrowths, truncations and small grains (all µm-scale) (Schutjens & Spiers, 1999).

Diffusive crack healing is driven by surface energy reduction and involves transport of the material through adsorbed thin water films. The rate of crack healing is enhanced by extra thick adsorbed aqueous films on crack surfaces and/or the presence of liquid brine (Houben et al., 2013). For dilated rocksalt, at sufficiently low intergranular stresses, deformation can start with pressure solution/mechanical healing, subsequently slowly resulting into the flattening of the islands and thereby changing the $\frac{2\gamma}{r}$ term of the Gibbs equilibrium equation (equation 1) (Visser et al., 2012). The material at the free grain wall sites dissolves and is transported via a fluid medium to the crack tip, where it precipitates. The necking growth of the cracks (also known as crack tip migration) by diffusive mass transfer leads the formation of sub-spherical fluid inclusions at the former position of the crack (Figure 2c) and a reduction of permeability, i.e. to healing but also sealing (Peach et al., 2001; Schutjens & Spiers, 1999; Urai et al., 1986).
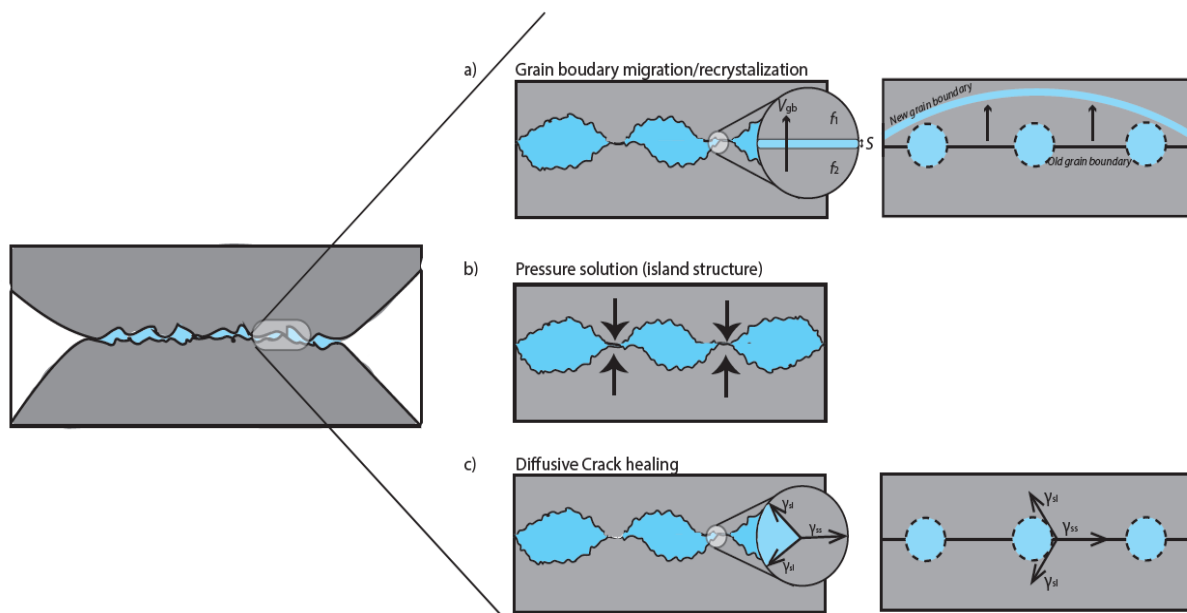

Figure 2: The three solution-precipitation processes that saturated brine can activate in coarse-grained rocksalt. a) Fluid-assisted grain boundary migration (recrystallization) overgrows the cracks producing a sequence of disconnected sub-spherical fluid inclusions which represent the former grain boundary. b) The mechanical closure of the cracks by transfer of material from the grain contact points with a high stress to the low stress pore walls (pressure solution). c) Diffusive crack healing at low intergranular stresses that includes the necking down of cracks and pores driven by surface energy and resulting into an alignment of fluid inclusions (adapted from Houben et al. (2013)).

1.2   Present aims

To further understand the inter-relationship between plastic flow, microcracking and the solution-precipitation processes at low effective stresses (e.g. simulating salt flow in abandoned caverns, salt plugs, the excavation damage zone of cavities or boreholes (Alkan et al., 2007; Hou, 2003)), this MSc project aims to investigate whether saturated brine penetrating the microcracks in coarse, dilated rocksalt leads to (1) crack healing and a stable deformation rate by dislocation mechanisms and/or pressure solution, or (2) crack growth and increasing deformation rates (unstable behaviour). This is of high importance when determining the occurrence of cavern instability and evaluating if the salt plugs are properly sealed to avoid any leakage. To investigate the interaction between mechanical behavior and healing processes in dilated rocksalt and to see which of the microstructural processes is dominant, dry and wet triaxial and unconfined compression experiments have been conducted on coarse-grained Zechstein rocksalt samples. The combination of triaxial and unconfined experiments is chosen to represent the different areas around the excavation damage zone of cavities or boreholes, in which the unconfined experiments correlate to the cavern walls (no or neglectible σ_3) and the triaxial experiments are located further away from the damage zone (including σ_3). These experiments can have up to three phases: first, compression to end up in the dilatant domain and resulting in dilation, and an increase of the permeability of the rocksalt sample (Figure 3). Secondly, the samples will undergo stress-relaxation under dry conditions until roughly steady state creep is observed and finally to subsequently allow for saturated brine to penetrate the deformed sample during the stress-relaxation phase. After deformation the samples will be prepared for microstructural observations with the Leica optical microscope. The undeformed and deformed microstructures will be described by grain size, shape, grain-to-grain contact and internal structure, which reflect the (redistribution) effect induced by the saturated brine for the deformed samples. The samples wil be tested for any change in mechanical behaviour if the geochemical environment changes, i.e. when saturated brine is introduced into the sample, and how the created microcracks influence the microstructural processes, i.e. which process is dominant and does it result in crack healing or crack growth.
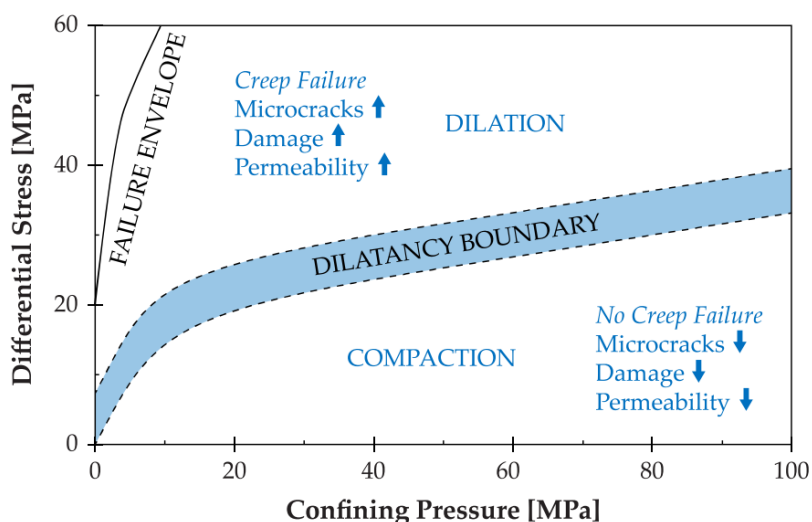

Figure 3: Differential stress versus confining pressure visualizing the deformation conditions corresponding to dilation and compaction of rocksalt for temperatures in the range of 20 to 200 °C and their effect on permeability, damage and the amount of microcracks (taken from Sinn et al. (2018)).

2   Methodology

To investigate the interaction between mechanical behavior and healing processes and to see which of the microstructural processes is dominant, confined and unconfined compression tests are performed on Leine Steinsalz, respectively with the triaxial 'Heard' apparatus and the Instron 8862 loading frame. Both types of experiments are executed at room temperature. After loading and dilation of the sample, the experiments are followed by stress-relaxation in both dry as wet environments with a duration of up to several days. Note that the wet environment refers to the injection of saturated brine. Reference experiments that have only undergone dry stress-relaxation after loading and dilation, have been performed for both experimental set-ups. All experiments were executed at the High Pressure and Temperature (HPT) Lab at Utrecht University, which supplied the required material and instruments.

2.1   Sample description

In this study, natural Leine Steinsalz from the Zechstein formation (courtesy of D. Brückner, IfG, Leipzig) was used (Figure 4). The material is a coarse-grained, colorless salt rock and the provided samples were cylindrical with a height of approximately 120 mm and a diameter of 50 mm. The porosity is consistently lower than 0.1% and the percentage of NaCl is >95%. The density of the Leine Steinsalz is 2.15 g/cm^3. The sample preparation was performed in a dry room (with a humidity lower than 20%) to reduce the effect of atmospheric water on the sample.

Figure 4: Leine Steinsalz used in the triaxial reference experiment. Note that the experiment is upside down relative to when it is loaded in the deformation apparatus
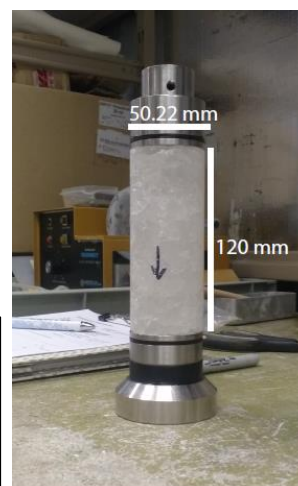
2.1.1   Undeformed Leine Steinsalz microstructural analysis

A microstructural analysis of the undeformed material is made as reference for the deformed samples. The microstructural preparation is described in Section 2.4. The halite grains are colorless, coarse (0.7-8.0 mm with a mean grain size of 4.4 mm) and have subidiomorphic to irregular, lobate shapes (Figure 5a and b). Subgrains are predominantly found along the grain boundaries and the smaller grains have a stronger subgrain structure meaning that they are completely filled with subgrains (Figure 5c). Approximately 25-40% of the grain contain a well-developed subgrain structure, with a mean subgrain size of 150 μm. Most of the grain boundaries also contain isolated subspherical fluid inclusions with a diameter of a few micrometers (Figure 5b and d), often between grains where one has a subgrain structure, while the other does not. The grain with little to no subgrain structure indents the subgrain-rich grain (Figure 5d). The fluid inclusions form a network along the grain boundaries, but not along the subgrain boundaries. Approximately 70% of the grains contain intracrystalline fluid inclusions (Figure 5b). Figure 5e shows that these fluid inclusions are forming a sub continuous network of tabular shaped inclusions or closely aligned spheres. The fluid-rich grains can be in contact with fluid-free grains with a subgrain structure, but also with an absent internal structure (Figure 5f). Overall, the grains can be divided into fluid-rich grains with no subgrains and fluid-free grains with a subgrain structure. Both of these grain types can have grain boundaries intersecting at a triple point with an angle of approximately 120°, as shown in Figures 5g and h.
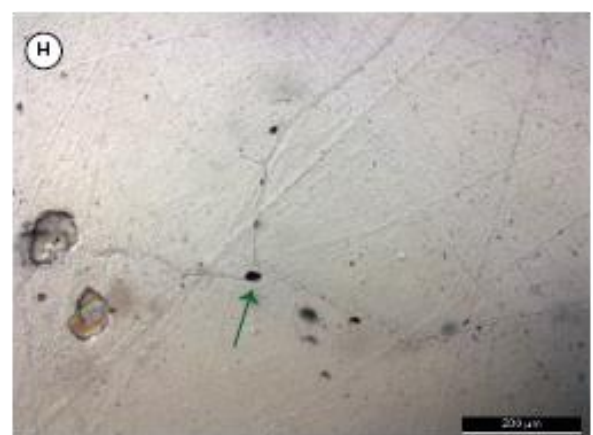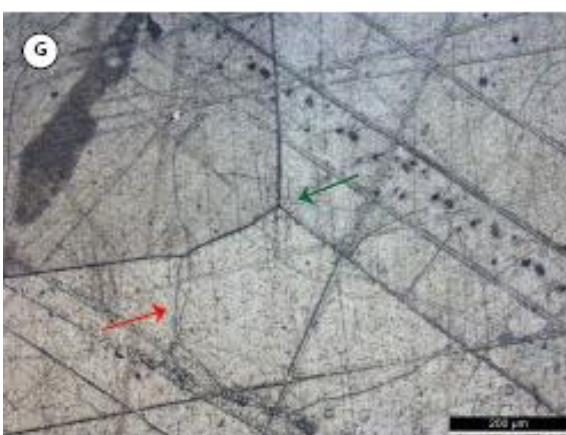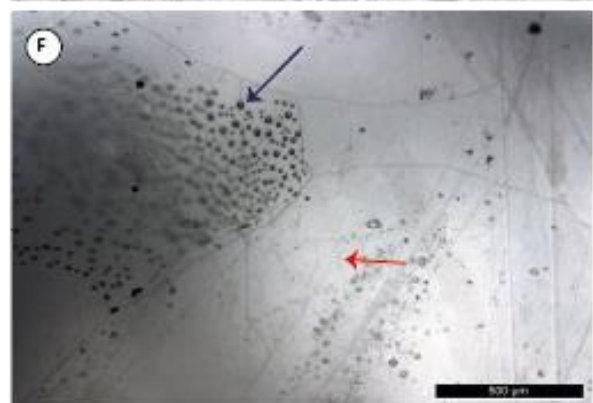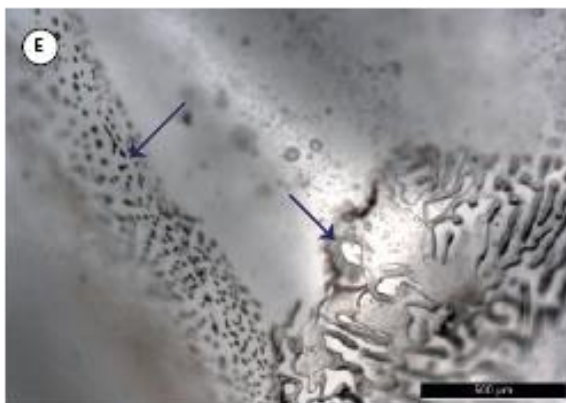
2.2   Triaxial compression experiments

2.2.1   Sample preparation

Due to coring and transport the edges of samples were discontinuous, i.e. grains fell out, which can cause the applied confining pressure to be distributed unevenly and possible puncture of the rubber sleeve leading in leaks. Therefore, a paste of NaCl (±300 µm) (MERCK) and distilled water was made. This was applied to the damaged surface to fill up the indentations. The samples were wrapped with an impermeable rubber sleeve, which was used to prevent any interaction with the confining fluid of the deformation apparatus (silicone oil). Then five layers of permeable glass fiber and two layers of Teflon were placed onto both sides of the sample for respectively enhancing the distribution of the fluid flow and to prevent the 'clamping effect' by reducing the fiction boundary effects between the piston and the sample. Note that the Teflon sheets were perforated by using a razor by making a large star in the middle of the sheet with a smaller star shape in each corner to allow fluid into the sample in a later deformation stage. Two steel deformation pistons that had a slightly larger diameter than the samples were placed on both sides the Teflon sheets (Figure 6). These pistons had a pore fluid inlet for allowing brine to penetrate the sample. Once the sample was positioned between the pistons, two wires of stainless steel were used to further seal off the sample, using a wire tourniquet against a Viton band countersunk into the piston. The wires were tightly wrapped over the rubber jacket into the grooves of the pistons.
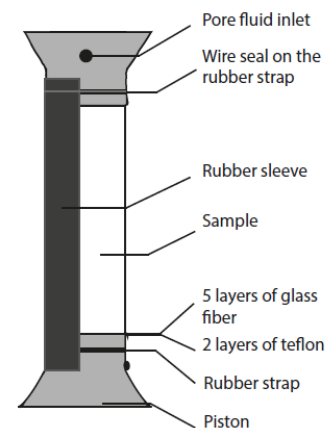
Figure 6: Schematic diagram of the sample preparation for the triaxial experiments of Figure 4. The Teflon and glass fibre sheets are on both sides of the sample.

2.2.2   Triaxial deformation and fluid flow apparatuses

The triaxial deformation apparatus used for this study is the 'Heard' machine. This machine, as described by Peach (1991), Peach and Spiers (1996) and Hangx et al. (2010), contains a main pressure vessel holding the cylindrical sample, a linked auxiliary pressure vessel and a load transmitting yoke-piston assembly driven by a motor/gearbox/ball-screw assembly (Figure 7) The main pressure vessel is covered by a furnace, which externally heats up the vessel and its contents, namely the confining medium, silicon oil, and the sample. The auxiliary pressure vessel allows for the piston movement only to be caused by the drive of the motor and not by the gradient in pressure between the two vessels, as silicon oil from the main pressure vessel to the auxiliary pressure vessel to maintain a roughly constant system volume. The upward movement of the yoke/piston assembly is used to load the sample. To achieve sealing on all of the components, seal Viton O-rings are used.

The linear potentiometer records the piston displacement of a servo-controlled volumometer pump (8 ml range, ±20 µl resolution) that is connected to both pressure vessels and keeps the confining pressure constant during the experiment. The piston displacement is measured at the yoke with a high-precision linear variable differential transformer (LVDT, 100 mm range, ±0.8 µm resolution), whereas the confining pressure is measured using a Jensen pressure transducer (100 MPa range, ±0.02 MPa resolution), A PID (proportional-integral-derivative) process controller (400°C range, ±0.02°C resolution) and a K-type (chromel/alumel) thermocouple located in the external furnace control the temperature of the sample, which is measured by two K-type thermocouples midway along the sample surface. A differential variable reluctance transformer (DVRT)-based, semi-internal load cell located at the top of the vessel is used to determine the axial load (400 kN range, ±0.035 kN resolution). The triaxial compression experiments can only be displacement-controlled.
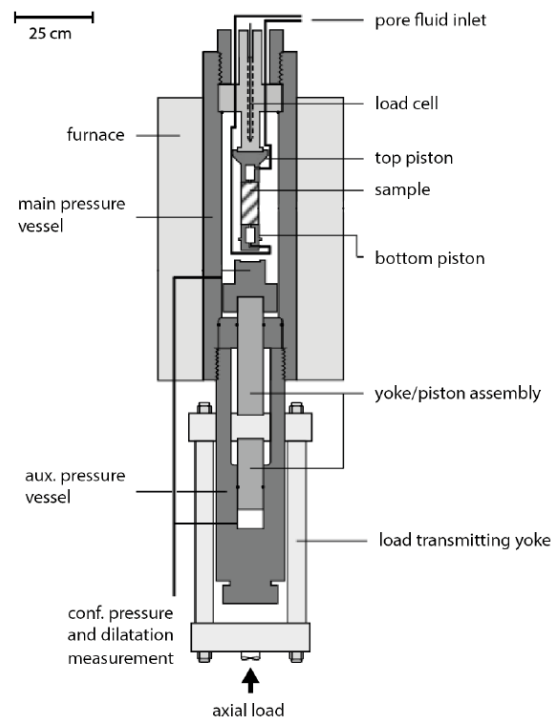
Figure 7: Schematic diagram of the 'Heard' triaxial deformation apparatus set-up (taken from Hangx et al. (2010)).
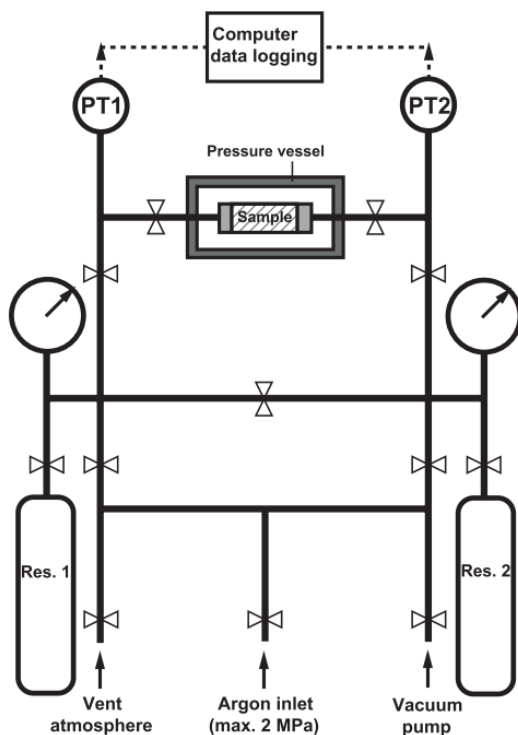
Figure 8: Schematic diagram of the transient step gas permeameter that is connected to the 'Heard' triaxial deformation apparatus (taken from Hangx et al. (2010)).

During the dry and wet phase of the experiments, pore fluid can enter (in this study respectively 99.9% pure argon or brine) the sample via inlet tubes that are connected to the pore fluid inlets positioned in the deformation pistons at the top (upstream) and bottom (downstream) of the sample. During the dry stress-relaxation phase, argon gas pressure can be applied on the ends of the sample using the transient step gas permeameter described by Peach (1991) and Peach & Spiers (1996) (Figure 8). This permeameter consists of two low volume tubing networks that are connected across the sample. The symmetrical arrangement of these pipes allows for pressure equilibration of the system through connection via the linking valve and when the linking valve is closed, the tubing systems can, independently, be pressurized with argon at pressure up to 2 MPa. The apparatus can be used for measuring permeabilities in a range of 10^{-12} m^2 - 10^{-21} m^2. There are three vents in the system; for evacuation of the system, for reducing gas pressure on one side of the sample and for the regulation of the argon supply (Hangx et al., 2010). Permeability measurements are started by equilibration with an Argon pressure by a predetermined amount. When the system is

equilibrated, the two tubing systems and the specimen are disconnected by closing off the two taps closest to the sample and the pressure of one system is dropped. The measurements start when the valves closed to the sample are reopened, allowing for the Argon to flow from the higher pressurized volume through the sample to the lower pressurized volume. If the sample already has undergone microcracking during the loading phase, Argon can enter the sample via the cracks. During the measurement, the temperature of the upstream and downstream end of the sample is computed by two temperature-compensated pressure transducers (2 MPa range, ±0.02 MPa resolution). This results in a change of effective pressure on the sample, following the law of effective stress:

$$Pe = Pc - Pf$$

where P_e, P_c and P_f are subsequently effective, confining and fluid pressure (all in MPa). The confining pressure always must be higher than the pore fluid pressure to prevent failure of the sample.

The wet phase of the experiments consists of the flushing of the experiment and the flow measurements of the control fluid. For flushing/vacuum filling of the sample with saturated brine two wash bottles, connected to the pore fluid inlets, are utilized. The fluid flow set-up for brine consists of two D-series ISCO pumps (65 ml volume). These pumps are connected to the up- and downstream side of the sample. The pumps are filled with approximately 45 ml and 17 ml for respectively the upstream (pump A) and the downstream pump (pump B). The por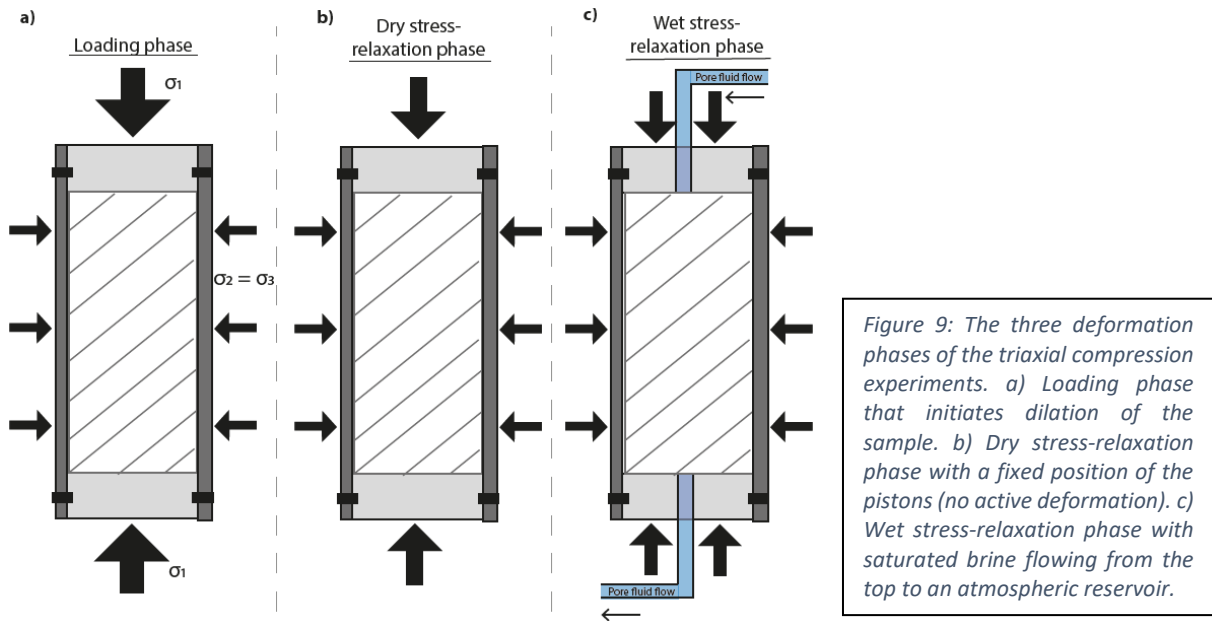e fluid is injected using the servo-controlled volumometer pump and a linear potentiometer to record piston displacement and pore volume changes. The pore fluid flows from pump A through the sample to pump B in which the fluid is collected. A Keller pressure transducer (50 MPa range, ±0.02 MPa resolution) is used to determine and control the pore fluid pressure.

2.2.3 Experiment set-up

All of the triaxial loading experiments were performed in the 'Heard' apparatus. The sample was installed in a frame including the pore fluid tubing and placed in the main pressure vessel. Before deformation could happen in the apparatus, the main vessel was pressurized up to a confining pressure (P_c) of 10 and 12 MPa for LSS001 and LSS002 respectively, then the auxiliary vessel was opened to even out the pressure in both vessels. As the confining pressure increased, the temperature of the oil also increased for which the experiment was left for a few hours to cool down. After cooling down, the sample was evacuated by using two wash bottles and a vacuum pump. This way all of the water and air were removed from the pore fluid inlets and tubing, which will optimize the stress-relaxation stage of the experiment.

During the running phase, the piston assembly moved toward the sample until the 'touch point' (contact between the pistons and sample) was detected. From this moment on, the loading phase began, where the applied force kept increasing and thereby the differential stress ($\sigma_1 - \sigma_3$) as the confining pressure was maintained constant ($P_c = \sigma_2 = \sigma_3$) (Figure 9a). The samples were deformed dry up to a strain of 10% and 17%, for respectively experiment LSS001 and LSS002, with a constant strain rate of 4.5×10^{-5} s^{-1} at room temperature. The applied strain rate is relatively fast compared to natural strain rates ($\dot{\varepsilon} = 10^{-10} - 10^{-14}$ s^{-1}). During the loading phase of LSS002, two permeability measurements were made with the transient step gas permeameter to verify the amount of dilation and subsequent permeability increase (See green zones in Figure 10). The sample was slightly unloaded to prevent any salt creep during the permeability measurement. For the permeability measurement the sample and permeameter were equilibrated with an internal Argon pressure of 21.1 bar. Once equilibrated, the permeameter halves were closed off for each other and subsequently a pressure step down of 1.0 MPa on one halve of the system was created. The permeability measurement was started just before the reopening of the two taps and over time a new pressure

Figure 9: The three deformation phases of the triaxial compression experiments. a) Loading phase that initiates dilation of the sample. b) Dry stress-relaxation phase with a fixed position of the pistons (no active deformation). c) Wet stress-relaxation phase with saturated brine flowing from the top to an atmospheric reservoir.

equilibrium develops leading to the end of the measurement. Subsequently, the pore fluid pressure was again increased to 2 MPa, which affects the effective confining pressure if the sample is permeable as ($P_e = P_c − P_f$).

The samples were deformed until a positive volumetric change of the samples (dilation) was observed. Subsequently, the displacement of the pistons was stopped, but the samples were kept loaded i.e. the pistons were kept in stable position. This allowed for the dry stress-relaxation phase (Figure 9b). The dry stress-relaxation phase continued up to approximately steady state creep. In LSS002 there was no indication for dilation after loading, and therefore the P_c was lowered from 12 to 10 MPa and from 10 to 7 MPa during dry stress-relaxation (Figure 10). Three permeability measurement were performed in the dry stress-relaxation phase, one for each confining pressure (12, 10 and 7 MPa). Note that if Argon penetrates the sample after the lowering of the confining pressure to 7 MPa, the effective confining pressure will be 5 MPa as $P_e = P_c − P_f$.

After dry steady state creep, the LSS002 sample was evacuated by using two wash bottles and a vacuum pump. For this experiment set one wash bottle (with the direct connection to the apparatus) was filled with room temperature brine to about a third of the flask. When the vacuum pump was disconnected, the sample was vacuum-saturated with the brine. The formation and/or healing of the
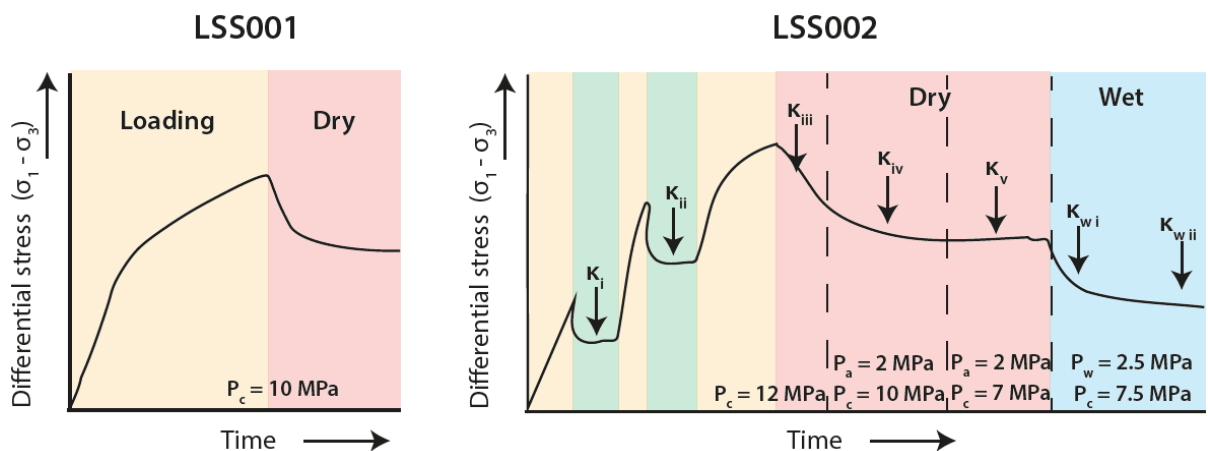
Figure 10: Schematic diagrams of the deformation history of the triaxial compression experiments LSS001 and LSS002 with differential stress vs time. The yellow, green, red and blue areas refer respectively to a loading phase, unloading and Argon permeability measurement, dry stress-relaxation and wet stress-relaxation. κ indicates permeability measurements in which $κ_i$ indicates a permeability measurement under dry conditions with the transient step gas permeameter (99.9% Argon) and $κ_w$ under wet conditions with the ISCO pumps (saturated brine). Note that the diagrams are not to scale.

cracks was investigated by flow measurements from one ISCO pump to another, the latter was kept at atmospheric pressure. The pore fluid pressure (P_f) was increased to 2.5 MPa and was kept constant during the wet phase of the experiment (Figure 9c). To achieve the same pressure state as during the dry stress-relaxation phase, the confining pressure was increased to 7.5 MPa, leading to an effective confining pressure of 5 MPa. The wet stress-relaxation phase lasted for one week. Two permeability measurements are executed at the beginning and at the end of the wet stress-relaxation phase. Finally, the sample was unloaded and prepared for microstructural analysis. The full deformation history of the triaxial compression experiments is illustrated in Figure 10.

2.2.4 Data logging and processing

2.2.4.1 Mechanical data

Variables like position of the piston, confining pressure, oil volume, internal and external force were logged every second with a 16 bit National Instruments VI Logger system during the experiment (Hangx et al., 2010). The confining pressure during loading was kept constant at 10-12 MPa. Therefore, the volume change in the silicone oil can be related to the volumetric strain of the sample ($\varepsilon_v = \frac{dV}{V_0}$), where ε_v is volumetric strain [-], dV the difference between the new and initial volume [mm^3] and V_0 the initial volume [mm^3]. The displacement of the pistons is related to the change in axial length of the sample and thereby axial strain ($\varepsilon = \frac{dl}{l_0}$), where ε is strain [-], dl the difference between the new and initial length [mm] and l_0 the initial length [mm]. The change in internal force relative to the start of the experiment and the sample area is related to the differential stress ($\sigma_1 - \sigma_3 = \frac{F_{int}}{A}$), where $\sigma_1 - \sigma_3$ is the differential stress [MPa], F_{int} the internal force [N] and A the sample area [mm^2].

But before the logged values of the triaxial compression apparatus can be put to use, a correction for the distortion has to be made. During the triaxial loading experiments the apparatus elastically deforms in small amounts caused by the stiffness of the machine and the influence of temperature fluctuation on the volumetric and displacement data has to be taken into account. A calibration procedure has been done on the 'Heard' apparatus at several confining pressures in March 2017. This calibration displays a linear trend of both apparatus distortion [mm] and volume change [ml] with increasing internal force [kN] at room temperature. After this correction, the obtained values are normalized with respect to the initial conditions at touch point of the experiment and subsequently the previously discussed formulas can be put to use.

During stress-relaxation the elastic stored energy in the salt (created during active deformation implied by the moving piston) dissipated as time-dependent creep of the sample plus apparatus (Rutter & Mainprice, 1978). The formula for the resultant axial creep strain (e_{cr}) is:

$$e_{cr} = \Delta(\sigma_1 - \sigma_3)\frac{C*A}{l_0} \qquad (2)$$

where $\Delta(\sigma_1 - \sigma_3)$ is the amount of stress-relaxation [MPa], C the compliance of the sample plus apparatus [mm/N], A the area of the sample [mm^2] and l_0 the initial length [mm]. The compliance (inverse of Youngs modulus (E)) can be determined via the linear regression of internal axial load and displacement data, both uncorrected for the distortion of the apparatus (Pijnenburg et al., 2018). The compliance is the slope of the (near-)linear part of the internal axial load vs displacement curve (i.e. up to [σ_1-σ_3] = 10 MPa in this study) The initial value of e_{cr} for each individual stress-relaxation phase is taken as 0%. The axial creep strain rate during relaxation ($\dot{\varepsilon}_{cr}$) is proportional to the stress-relaxation rate:

$$\dot{\varepsilon}_{cr} = \frac{d(\sigma_1 - \sigma_3)}{dt} \frac{C*A}{l_0} \quad \text{(Rutter \& Mainprice, 1978)} \quad (3)$$

The stress-relaxation rate was calculated using a variable window size corresponding to a fixed stress drop to minimize the scattering of the differential stress vs time values for the axial creep strain rate [s^{-1}]. The stress-relaxation data is used to gain insight in the type of creep in rocksalt at low strain rates.

For distinguishing the type of deformation mechanism, the relationship between the axial creep strain rate and the differential stress must be analyzed by using a conventional power law creep of the type (Weertman & Weertman, 1970):

$$\dot{\varepsilon} = A(T)\sigma^n \quad (4)$$

$$\log(\dot{\varepsilon}) = \log[A(T)] + n*\log(\sigma) \quad (5)$$

where $\dot{\varepsilon}$ is the axial creep strain rate [s^{-1}], σ is the differential stress [MPa], and n and A are constants (under fixed temperature conditions). The n-value is directly linked to the type of mechanism of deformation, where a high n-value (>3), implying that stress is not largely dependent on axial creep strain rate, and low n-value (±1) are respectively related to dislocation creep and solution-precipitation processes (Muhammad, 2015).

2.2.4.2   Permeability data: control fluid argon

For the transient step gas permeameter a 16-bit Keller READ30 system is used to log the temperature and pressure every five seconds of both of the tube networks. These variables are recorded until no significant pressure change in the tubing systems is noted in LSS002. We assume that there is no chemical reaction between the sample and fluid takes place, no leaks and the filled pore volume of the sample is neglectable compared to the volumes of the tubing systems of the permeameter. Sutherland & Cave (1980) provided an analysis for the pressure decay equation with time:

$$\Delta P_t = (\Delta P_0)e^{-\alpha t} \quad (6)$$

$$\log\left[\frac{\Delta P_t}{\Delta P_0}\right] = -\alpha t \quad (7)$$

$$\frac{d}{dt}(\log \Delta P_0 - \log \Delta P_t) = -\alpha \quad (8)$$

$$\text{with} \quad \alpha = \frac{\kappa.A}{\mu.\beta.L} \cdot \frac{V_1 + V_2}{V_1.V_2} \quad (9)$$

Where ΔP_t is the fluid pressure difference across the sample after time t, ΔP_0 the fluid pressure difference across sample at time t = 0, κ the permeability of the sample [m^2], A the area of the sample [m^2], L the length of the sample [m], , μ the dynamic viscosity of Argon [Pa.s], β the isothermal compressibility of Argon [Pa^{-1}] and V_1 and V_2 the volumes of reservoir 1 and 2 respectively [m^3]. t = 0 is defined as the moment the pressure step is applied. α, and therefore the permeability κ, can be determined from the slope of the graphical plot of $\log(\Delta P_t)$ vs time t (equation 8).

2.2.4.3   Permeability data: control fluid saturated brine

During the wet stress-relaxation/flow-through phase of LSS002 LabVIEW recorded the flow rate, pressure and volume of the pumps every second. Using Darcy's law, the permeability of the sample can be determined:

$$Q = \frac{-\kappa}{\mu} A \frac{dP}{dL} \qquad (10)$$

where Q is the volume flow rate per unit area [m³/s], κ the permeability of the sample [m²], μ the dynamic viscosity of saturated brine [Pa.s], A the cross-sectional area of the sample [m²] and dP/dL the pressure gradient of the fluid over the length of the sample [Pa/m]. To reduce the scatter of the recorded variables, the data set is smoothed over a window size of 10. This means that for each smoothed point the average is taken over the next ten points. The slope of the graphical plot of volume V vs time t, gives us the flow rate Q. This is done for the recorded volume values for pump A as pump B to account for any fluid loss during the flow-through phase. Therefore, the flow rate of the upstream pump A will always be higher than for the downstream pump B. The true flow rate in the sample will be between these values of pump A and pump B. Therefore, we can only calculate the maximum and minimum values for the permeability of the sample with respectively using the flow rate of upstream pump A and downstream pump B in equation (10). In this study, pump A was set to a pore fluid pressure of 2.5 MPa, while pump B was stopped and set to atmospheric pressure. This results in that we cannot calculate the lower limit of the permeabilities measurements done with the ISCO pumps.

2.3   Unconfined compression experiments

2.3.1   Deformation apparatus

An Instron 8862 servo-controlled testing machine is used for the uniaxial compression experiments. The apparatus consists of a moveable loading ram, two moveable pistons holding the cylindrical sample, all made of hardened stainless steel, and it can produce up to 100 kN of axial force. Unlike the 'Heard' apparatus, the Instron experiments can be carried out as position-control and stress-control, respectively a stress-relaxation experiment and a creep experiment. The load on the sample is applied by the upward movement of the loading ram, which is driven by an underlying motor
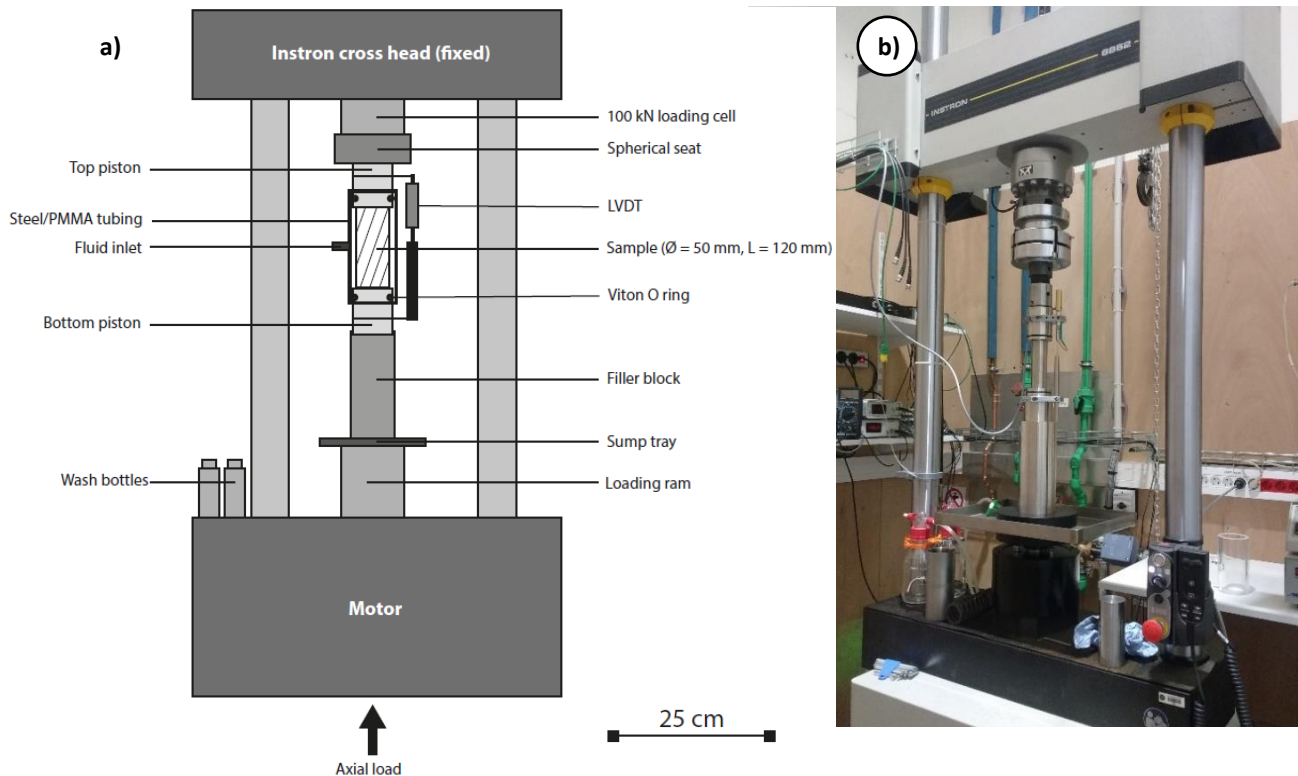

Figure 11: a) Schematic diagram of the Instron 8862 unconfined deformation set-up and b) The experimental set-up. The sample is compressed by the upwards movement of the loading ram.
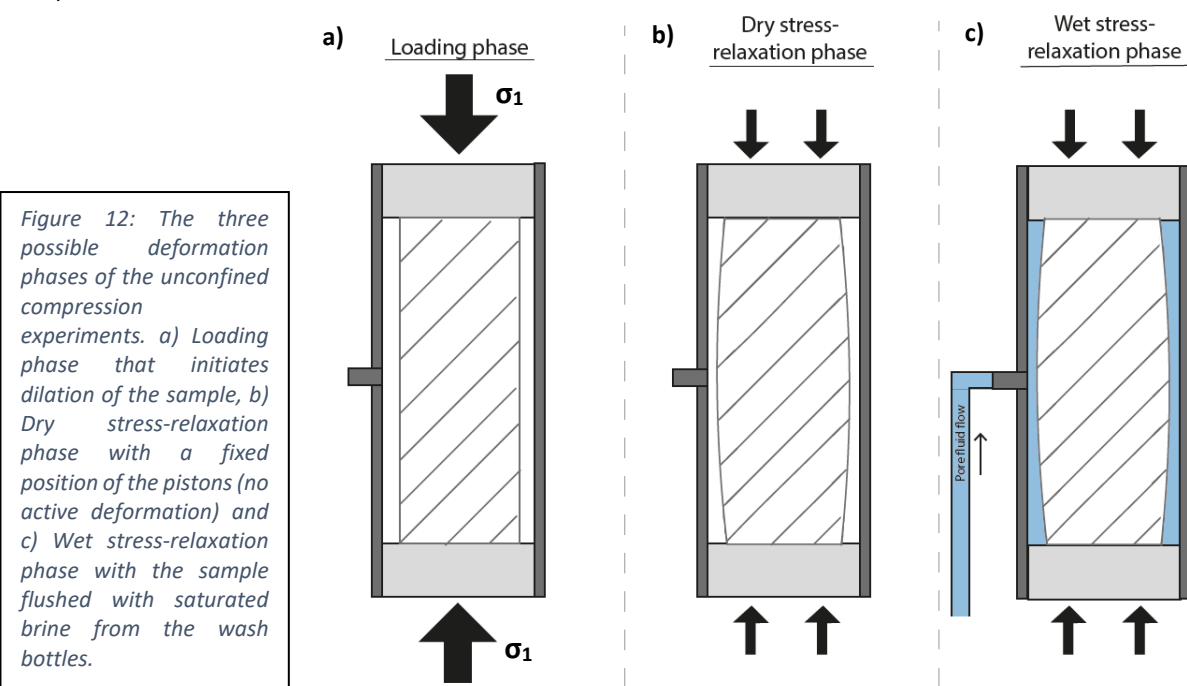
(Figure 11). This is measured externally by the Instron load cell (100 kN range, ± 1N resolution). The piston displacement is established externally adjacent to the sample with a high-precision linear variable differential transformer (20 mm range, ±0.2 µm resolution). The pistons and steel/PMMA tubing are sealed by Viton O-rings. The apparatus only supports room temperature experiments, for which the temperature of the external air is measured by a K-type thermocouple with AD595 conditioner. The fluid inlet is in connection with a steel tube connecter with two inlets that can be opened or closed for the control fluid wash bottle and vacuum pump. This is necessary for maintaining the vacuum of the sample and no water vapor is present during the dry stages of the experiment.

The Instron allows for a wet phase of the experiment. Similar to the triaxial deformation experiments, two wash bottles filled with fluid (in this study saturated brine) are used to vacuum-saturated the sample with pore fluid via the inlet tube that connects the wash bottles to the fluid inlet attached to the steel/PMMA tubing of the sample. A sump tray is positioned beneath the experimental cell to collect any spillage of the fluid.

2.3.2   Sample preparation and experiment set-up

For the unconfined compression experiments the indentations at the top and bottom of samples were not filled with a NaCl paste, as the following experiments did not include a rubber sleeve around the sample and a confining pressure that can distribute the applied stress/pressure unevenly. Similar to the triaxial experiments, two sheets of Teflon were placed between the sample and the pistons to avoid the 'clamping' effect.

The sample-tubing-piston assembly was placed between the filler block and spherical seat. After aligning of the assembly, so that the force was evenly distributed, the sample was evacuated by using two wash bottles and a vacuum pump. Load was applied by activating the screw-driven loading ram at a strain rate of $\pm 10^{-5} - 10^{-6}$ s^{-1}. The experiments were deformed by only a few percent of strain (up to 3%) to allow for semi-brittle behavior of the salt, without causing failure (Figure 12a). Less strain was necessary with unconfined experiments to dilate the sample compared to the triaxial experiments, since there were no σ_2 and σ_3 to counteract the dilation effect. After the loading stage the pistons were kept stationary, introducing the dry stress-relaxation phase of the experiment (Figure 12b).

Figure 12: The three possible deformation phases of the unconfined compression experiments. a) Loading phase that initiates dilation of the sample, b) Dry stress-relaxation phase with a fixed position of the pistons (no active deformation) and c) Wet stress-relaxation phase with the sample flushed with saturated brine from the wash bottles.

As the stress reaches a near steady state flow during the dry stress-relaxation, three different procedures are followed: 1) LSS003 is unloaded, unfortunately causing the sample to crumble apart and making thin sectioning impossible, 2) for LSS007 saturated brine is injected in the sample and the existing microcracks allow the saturated brine to enter the creeping sample (Figure 12c) and 3) LSS008 is reloaded with a similar strain rate up to the same peak stress of the first loading phase (20.8 MPa). Immediately upon reaching the peak stress the sample is flushed with saturated brine. The vacuum of LSS007 and LSS008 was poor, resulting into the top 1.26 cm and 2.5 cm of the sample respectively to be dry during the flushing of the samples. One wash bottle (with the direct connection to the apparatus) was filled with room temperature brine and was linked to an empty wash bottle and a vacuum pump. The sample was evacuated again and when the vacuum pump was disconnected the sample was flushed with the saturated brine. The sample was left untouched to undergo wet stress-relaxation. For one experiment it was chosen to not flush the sample and a second dry stress-relaxation phase was initiated. The full deformation history of the unconfined compression experiments is illustrated in Figure 13.
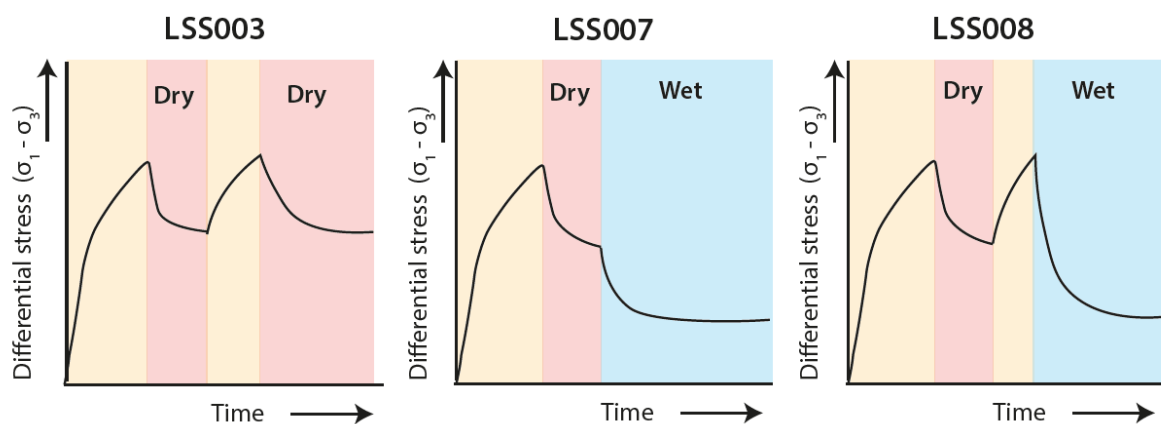
Figure 13: Schematic diagrams of the deformation history of the triaxial compression experiments LSS003, LSS007 and LSS008 with differential stress vs time. The yellow, red and blue areas refer respectively to a loading phase, dry stress-relaxation and wet stress-relaxation. Note that the diagrams are not to scale.

2.3.3 Data logging and processing

During the experiments the Instron position, temperature and load were recorded every second using a PC equipped with the digital converter 16-bit National Instruments VI Logger system. Similar to the processing of the data of the 'Heard' apparatus, the obtained data has to be corrected for the elastic distortion created by the Instron apparatus. A calibration was performed at various loads with a 304-steel dummy with known properties, while measuring the displacement. The formula describing the least-square fit of the data established that the distortion of the machine is minimal and no correction is needed. The data processing of the mechanical data (axial strain ε, differential stress $\sigma_1 - \sigma_3$ and axial creep strain rate $\dot{\varepsilon}_{cr}$) are determined analogous to the calculations used for the 'Heard' triaxial compression data (cf. Section 2.2.4)

2.4 Microstructural analyses

Microstructural analyses have been performed using the LEICA optical microscope at Utrecht University. The microstructural results will be correlated to the mechanical data obtained during the deformation in the 'Heard' and Instron 8862 apparatuses. Also, the section of undeformed Leine Steinsalz described before was made with this methodology. A general overview of the used thin section techniques for dilated coarse-grained rocksalt is given in Appendix A.

After the different stages of deformation in the 'Heard' and Instron apparatuses, the deformed samples were unloaded, removed from the machine and they were delicately removed from respectively their rubber jackets or PMMA tubing. For the microstructural preparations the samples were moved to the dry room. To prepare the samples for microstructural study, the samples were first cut dry, two times along in the plane perpendicular to the length using a metallurgical band saw, creating three sections (Figure 14). Sections 1 and 3 were sliced four times along their length with reference to the centre of the sections using a diamond wafering blade, creating two 5 mm thick sample slices. The diamond wafering blade was also used to cut the middle section, section 2, four times along the plane of the diameter. The slices were approximately 5 mm thick. The cutting with the diamond wafering blade was performed with evaporating oil (Fenela VD 201 N), using the lowest cutting force possible to minimize the damage to the sample, with the sample mounted in a screw-grip holder (Figure 15). The deformation in the sample that had only undergone dry stress-relaxation in the triaxial 'Heard' apparatus, lead to instability of the coarse salt grains, causing them to fall out at making thinner cuts. Therefore, the sections were impregnated with epoxy resin (Araldite2020, with components A and B mixed in a 100:30 ratio) and placed in a vacuum chamber to extract the remaining air from the sample before using the diamond wafering blade. Subsequently, the slices were polished by low and high grade carborundum (SiC) papers (P120 up to P4000) and finished with micro polish (Buehler) with a grain size of 0.3

Figure 14: Orientations of the sections concerning the microstructural preparation. Section 1 and 3 involve vertical cuts and section 2 horizontal.

Figure 15: Making the thin sections of the sample using the diamond wafering blade, which cleans itself by rotating in the evaporating oil filled container at the bottom of the apparatus.

µm. Finally to improve the display of the microstructures, the samples were etched using a solution of 95% saturated NaCl solution + 5% de-ionized water containing ±0.8 wt.% $FeCl_3 \cdot 6H_2O$, rinsed with hexane and dried with hot air (following the method described by Muhammad, 2015 and Ter Heege et al., 2005). The thick sections were firm enough to support their own weight, therefore the sections were not placed on a glass plate.

The Leica optical polarization microscope was used to make high quality images of the microstructures of the thin sections (resolution ±100 µm). This microscope was equipped with a high resolution digital image acquisition system. The samples were analysed with reflective and transmissive light and evaluated on grain size, shape, grain-to-grain contact, their interrelationship with cracks and internal structure. The grains of the sample were too large to be interpreted correctly by one photo. Therefore, multiple photos were made and stitched together to obtain a better overview of the microstructural interrelationships. Panorama photos were made using Microsoft Image Composite Editor. Measurements of the grain size pre- and post-experiment were done by using the 'linear intercept' method.
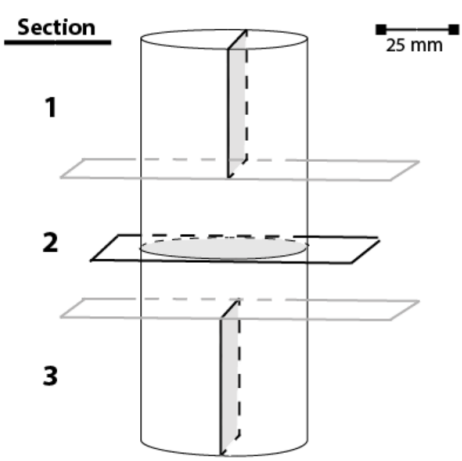
3 Experimental Results

3.1 Triaxial compression experiments

3.1.1 Dry and wet mechanical behaviour

The key mechanical data and deformation phases of the triaxial compression experiments is given in Table 1. LSS001 was performed to get a full understanding of the dry creep behaviour (under vacuum) of natural coarse-grained rocksalt, while LSS002 has a dry and a wet (with saturated brine) stage for comparing the different types of behaviour. Both LSS001 and LSS002 are loaded at a constant strain rate of $4.5 \cdot 10^{-5}$ s^{-1}, respectively in one (P_c = 10 MPa) and three loading phase(s) (P_c = 12 MPa), of which the loading phase of LSS001 and the third loading phase of LSS002 are followed by dry stress-relaxation. The other two loading phases of LSS002 are followed by slight unloading and a permeability measurement (Figure 10). LSS002 also undergoes wet stress-relaxation after 22 days of dry deformation. The mechanical behaviour of samples is illustrated in graphs regarding differential stress and volumetric strain vs axial strain is illustrated in Figure 16, while differential stress and axial creep strain rate vs time curves in Figure 17. Figure 18 shows the complete deformation history of LSS002. The permeability data of LSS002 is given in Table 2. Note that dilation of the samples is recorded as positive volumetric strain.

Table 1: Test conditions and deformation phases of the triaxial and unconfined compression experiments, where the letters A, B, C refer to the deformation phases described in Figures 9 and 12, respectively the loading phase, dry stress-relaxation phase and wet stress-relaxation phase. See Figures 10 and 13 for a schematic overview of the deformation phases of respectively the triaxial and unconfined compression experiments.

Sample	Deformation phases	Test environment	Experiment duration	Pc [MPa]	$\dot{\varepsilon}$ [s^{-1}]	$(\sigma_1-\sigma_3)_{max}$ [MPa]	ε_{axial} [-]
Triaxial compression experiments							
LSS001	A, B	Dry vacuum	3.8 days	10	4.5×10^{-5}	47.6	9.85%
LSS002	A, B, A, B, A, B, C	Dry vacuum	22 days	5-12	4.5×10^{-5}	30.1 51.9 55.3	2.4% 12.5% 17%
		Saturated brine	10 days	5	-	No additional displacement	17%
Unconfined compression experiments							
LSS003	A, B, A, B	Lab air	1 day 1 day	n.a.	4.5×10^{-6}	18.6 20.5	1.2% 2.9%
LSS007	A, B, C	Dry vacuum	1 day	n.a.	10^{-5}	21.5	2%
		Saturated brine	2 days	n.a.	-	No additional displacement	2%
LSS008	A, B, A, C	Dry vacuum	3 days	n.a.	10^{-5}	20.8	1.3%
		Saturated brine	5 days	n.a.	10^{-5}	20.8	1.5%

Pc: effective confining pressure

$\dot{\varepsilon}$: Constant strain rate during loading

$\sigma_1-\sigma_{3\,max}$: Max differential stress immediately after loading

ε_{axial}: Total axial strain at peak differential stress

All experiments are performed at room temperature.

The stress-strain diagram shows a near-linear relationship up to an axial strain of ±0.4-0.5% (±8-10 MPa), indicating the elastic behaviour of the rocksalt (Figure 16a). Upon further loading, the behaviour deviates from linearity, displaying continuous work hardening, where with increasing axial strain the hardening rate decreases. However, steady state flow is never reached. Note the close resemblance of the stress-axial strain behaviour of the samples in terms of elastic behaviour and the hardening rate (Figure 16a) plus the initial compaction during each loading phase, followed by dilatation (positive going volume change) (Figure 16b). While LSS001 instantly is loaded up to a total axial strain ε_{axial} of 9.85%, LSS002 has two permeability measurements at ε_{axial} 2.4% and 12.5% (Figure 16a). Prior to these measurements the sample is slightly unloaded at 2.4% strain from 30 to 12.5 MPa and at 12.5% strain from 52 to 30 MPa. When the LSS002 sample was reloaded after the permeability measurement, the differential stress vs axial strain plot followed the same trend as before the unloading.
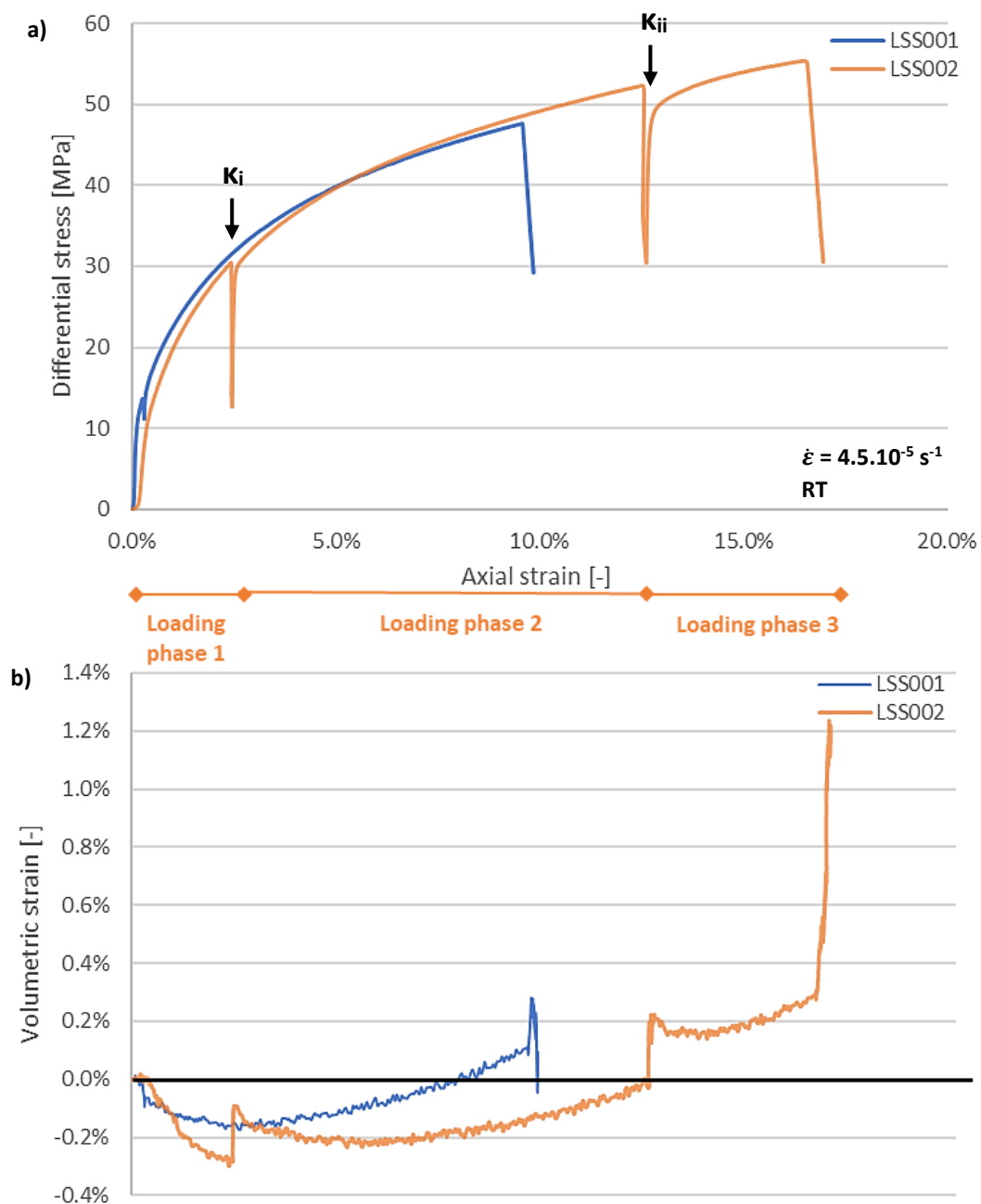

Figure 16: The full deformation of the triaxial experiments (LSS001: blue and LSS002: orange) a) differential stress and b) volumetric strain (black line divides dilation (+) and compression (-) domain) vs axial strain. κ refers to the permeability measurements of LSS002 done in-between loading phases.

During the initial loading phase, the volumetric strain ε_{vol} of LSS001 and LSS002 decreased (compaction) to respectively -0.15% and -0.30% at ε_{axial} = 2.4% (Figure 16b). For LSS001 dilatation is initiated by the ongoing loading of the sample resulting in dilation of the sample from 8% axial strain on. On the other hand, the volumetric strain slowly recovers as LSS002 is slightly unloaded for the permeability measurements at ε_{axial} 2.4% and 12.5%, resulting in an instant ε_{vol} increase of respectively -0.30% to -0.10% and 0.0% to 0.2%. As the sample is reloaded after the first permeability measurement at 2.4% ε_{axial}, the sample is compressed again until cracks form at an axial strain of 5% initiating dilatation from -0.2% to 0.0% volumetric strain. A similar behaviour is seen for the third loading phase after the second permeability measurement at 12.5% ε_{axial}: the sample is first compressed up to an axial strain of 13.7%, followed by dilation from 0.14% to 0.28% volumetric strain.

During dry stress-relaxation, LSS001 and LSS002 show similar behaviour (Figure 17). During the first 24 hours after piston arrest the differential stress of both LSS001 and LSS002 relaxed by ±16-18 MPa, respectively from 47.6 to 31.4 MPa and from 55.3 to 37.2 MPa (Figure 17a) and the axial creep strain rate $\dot{\varepsilon}_{cr}$ simultaneously dropped from ±10^{-6} s^{-1} to ±10^{-9} s^{-1} (Figure 17b). From this point on
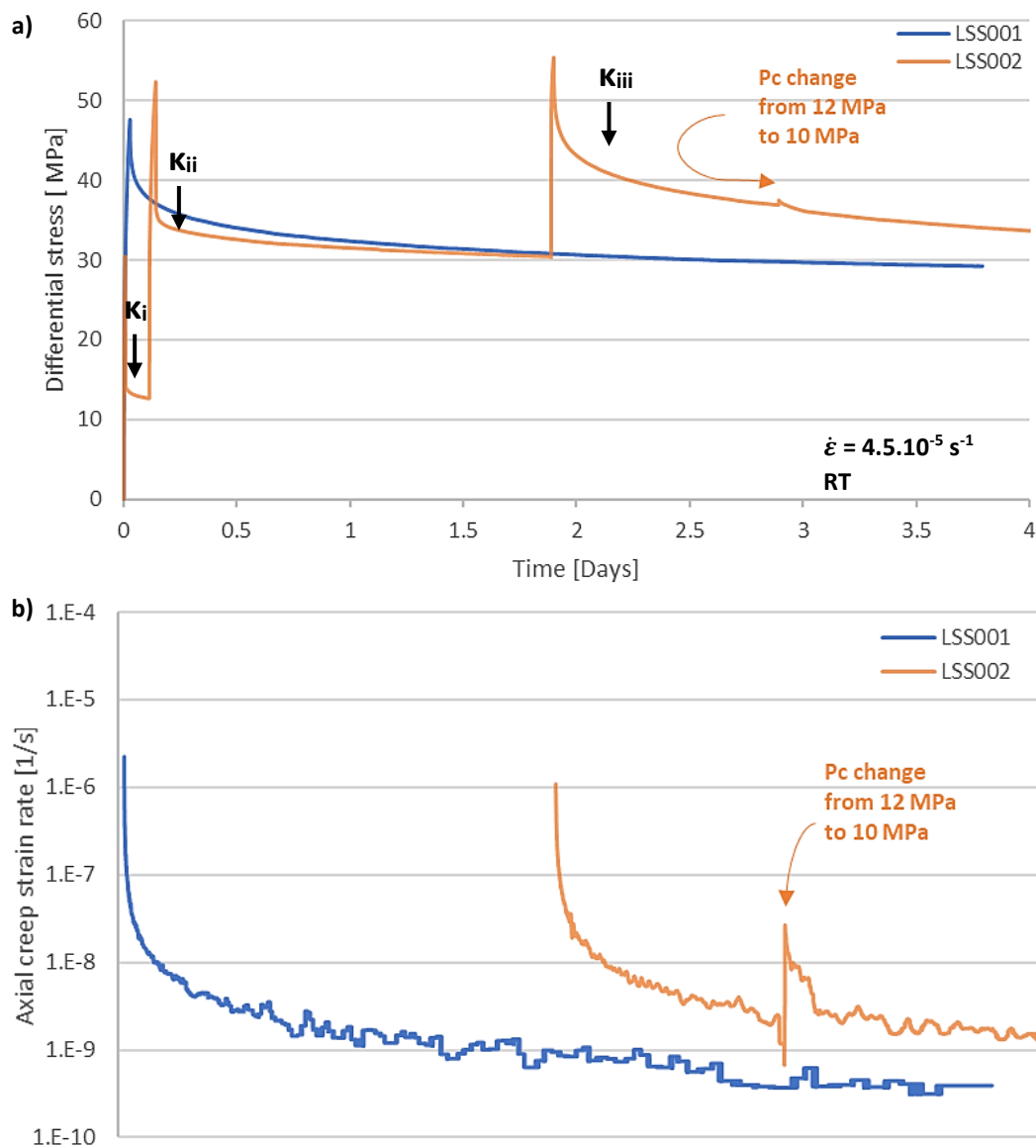

Figure 17: The mechanical behaviour of the triaxial experiments (LSS001: blue and LSS002: orange) for the first four days a) differential stress, b) volumetric strain (black line divides dilation (+) and compression (-) domain) and c) axial creep strain rate (log scale) vs time. κ refers to the permeability measurements of LSS002 done under dry conditions.

the differential stress and the axial creep strain rate of both experiments are nearly stable, respectively ±30 MPa and ±4.10^{-10} s^{-1}, but steady state flow is never reached. Also, the creep of the samples leads to a slight increase in axial strain during the stress-relaxation phases (Figure 16a). The volumetric strain ε_{vol} of both experiments never falls below 0.0% (Figure 16b). During the dry stress-relaxation of LSS002 the confining pressure was dropped from 12 MPa to 10 MPa to promote the formation of microcracks. This led to an instantaneous increase in ε_{vol} from 0.7% to 1%, a rapid increase of $\dot{\varepsilon}_{cr}$ by an order of magnitude and a minor reaction on the differential stress. $\dot{\varepsilon}_{cr}$ follows the same trend as before after a couple of hours. Around day 15 the confining pressure of LSS002 was lowered from 10 to 7 MPa, but its effect on the mechanical behaviour cannot be established as the logging apparatus crashed and the data was lost.

The influence of brine was only studied for sample LSS002. After 22 days of dry deformation the confining pressure was increased to 7.5 MPa and saturated brine is injected in LSS002 (with a pore fluid pressure of 2.5 MPa). The immediate reaction of the sample was a minor increase in volumetric strain due to the lowering of the effective confining pressure from 7 to 5 MPa ($P_e = P_c - P_f$) and a slightly
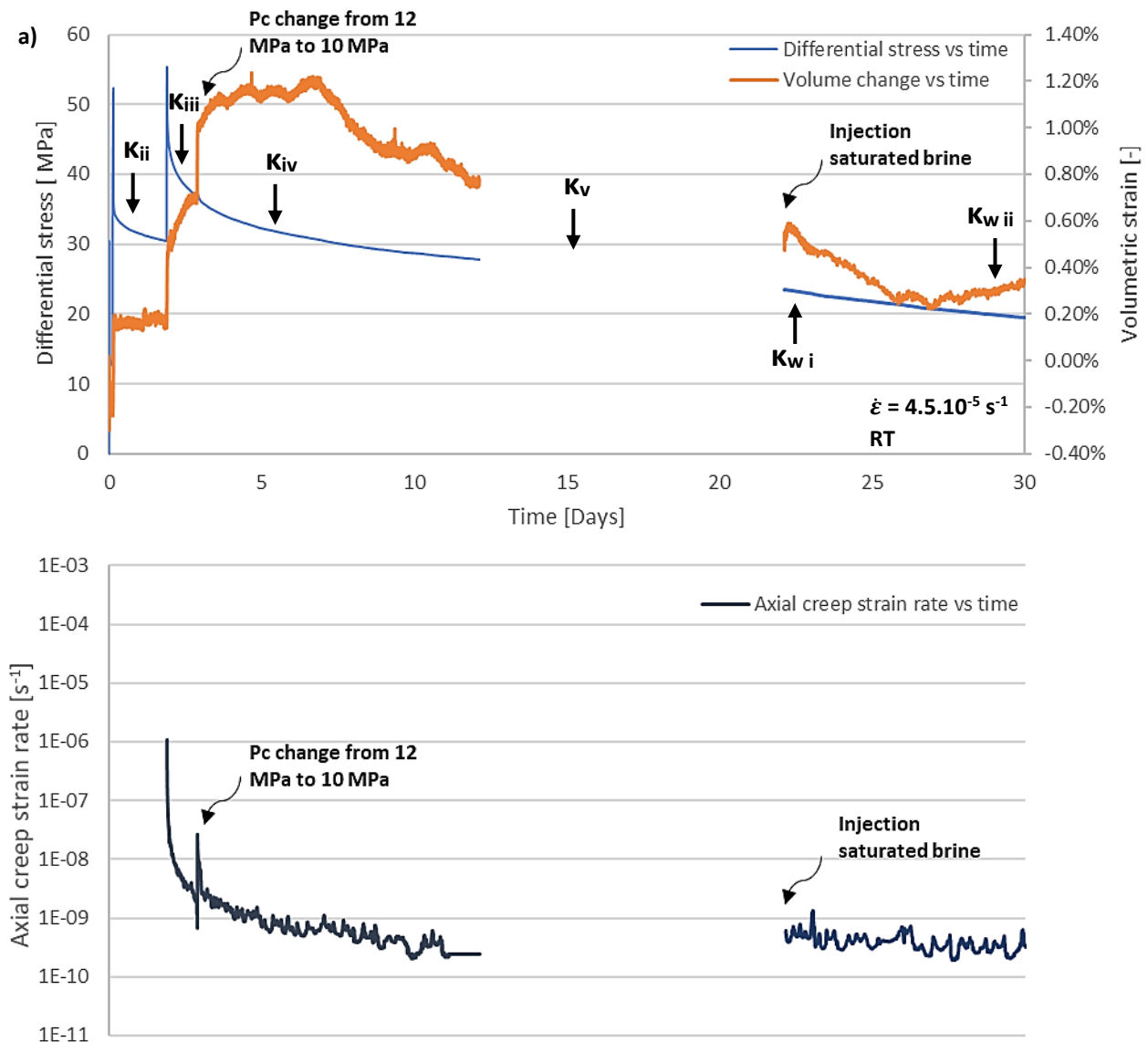
Figure 18: The full deformation record of 32 days of LSS002. a) Differential stress and volumetric strain vs time. b) Axial creep strain rate vs time. κ refers to the permeability measurements of LSS002 done in which κ_i indicates a permeability measurement under dry conditions and κ_w under wet conditions. κ_v was performed around day 15. However, the corresponding data is missing from day 12 to 22 due to the crashing of the logging program of the 'Heard' apparatus.

higher rate in stress reduction (Figure 18a and b). The axial creep rate stays constant around 10^{-10} s^{-1} during the whole wet phase and the volumetric strain evolves towards 0.30%. The differential stress relaxed by ±4 MPa during the wet stress-relaxation phase. Overall, no significant change in mechanical behaviour and no steady state creep are observed after 10 days of wet deformation.

In order to have a first order assessment of the dependence of creep strain rate of differential stress, a log stress-log strain rate graph is presented in Figure 19 (cf. Section 2.2.4). , Plotting the logarithmic values of stress and strain rate against each other, leads to a relatively linear correlation where the slope is equal to the stress component n of the power law. The dry and wet relaxation phases are plotted separately plus three curves representing n-values of 1, 5 and 10 in log-log space (Figure 19). As can be observed, mean n-values are high for the dry phases (n = 9-15), while a low average n-value is observed for the wet phase (n = 2.8). A rapid increase in slope is observed when the confining pressure of LSS002 is decreased from 12 to 10 MPa, but quickly decreases to later follow the same trend as before.
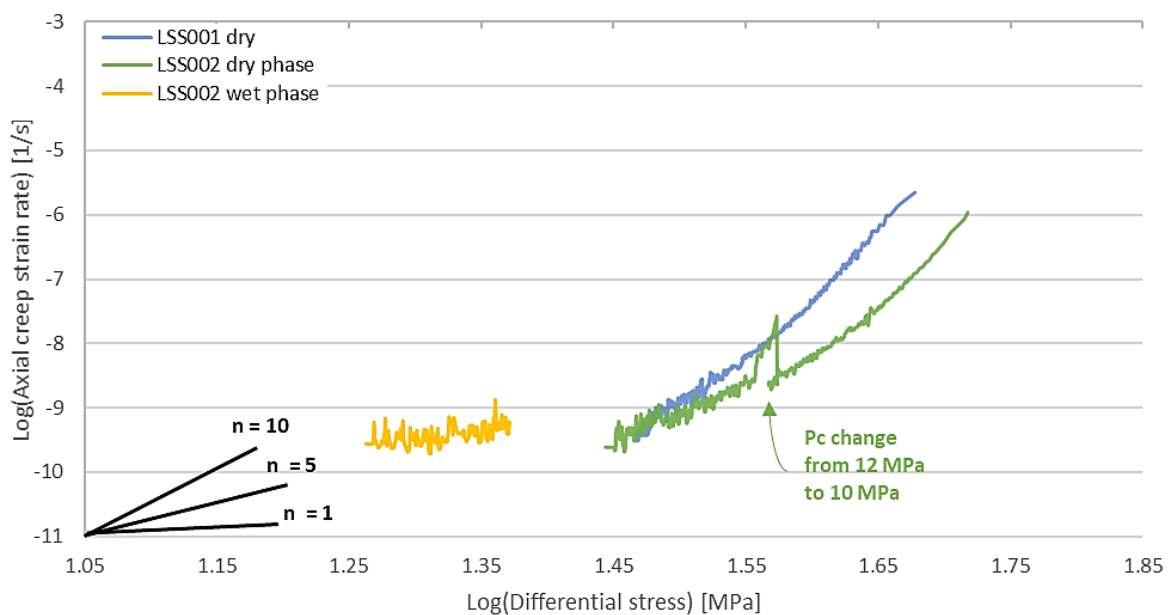

Figure 19: The log-log plot of axial creep strain rate vs differential stress for each stress-relaxation phase of the triaxially deformed samples. Three slopes representing n = 1, 5 and 10 (black lines) are included as comparison between the trends.

During experiment LSS002 six permeability measurements are performed: two in-between loading phases (κ_i, κ_{ii}) three during dry stress-relaxation (κ_{iii}, κ_{iv}, κ_v) and two during wet stress-relaxation ($\kappa_{w\,i}$, $\kappa_{w\,ii}$) (Table 2 and Figure 10). The first three permeability measurements are done at P_c = 12 MPa (κ_i, κ_{ii}, κ_{iii}) and are lower than 10^{-21} m^2, which is the measuring limit of the permeameter. After the confining pressure is decreased from 12 MPa to 10 MPa, a permeability of 9.5×10^{-19} m^2 and 3.3×10^{-20} m^2 as upper and lower limit is measured. This means that the Argon has penetrated the sample and the corresponding pore fluid pressure (2.0 MPa) now affects the effective pressure ($P_e = P_c - P_f = 8.0$ MPa). When the confining pressure was decreased to 7 MPa, the permeability is still in the same order of magnitude as before. Although the logging program crashed during the lowering of the confining pressure, we can positively say that the effective confining pressure was 5 MPa for the last part of the dry stress-relaxation phase. When saturated brine was injected, there was no immediate increase in permeability. However, at the end of the wet stress-relaxation the permeability did increase by an order of magnitude to 4.3×10^{-18} m^2. The lower limit of the permeabilities during the wet stress-relaxation could not be determined as pump B was open to the atmospheric pressure.

Table 2: The permeability measurements performed in LSS002. See Figures 10, 17a and 18a for an overview of the time placements of each measurement. The upper and lower limit refer to possible leaks and the true permeability of the sample will lay between these values.

Measurement #	Time	Pressure conditions	Permeability [m^2]	
			Upper Limit	*Lower Limit*
DRY PHASE				
K_i	Between loading phase 1 and 2		>10^{-21}	n.a.
K_{ii}	Between loading phase 2 and 3	P_c = 12.0 MPa P_f = 0.0 MPa	>10^{-21}	n.a.
K_{iii}			>10^{-21}	n.a.
K_{iv}	Stress-relaxation	P_c = 10 MPa P_f = 2.0 MPa P_e = 8.0 MPa	9.5x10^{-19}	3.3x10^{-20}
K_v		P_c = 7.0 MPa P_f = 2.0 MPa P_e = 5.0 MPa	1.47x10^{-19}	4.12x10^{-19}
WET PHASE				
$K_{w\ i}$	Stress-relaxation	P_c = 7.5 MPa P_f = 2.5 MPa P_e = 5.0 MPa	2.5x10^{-19}	Not determined
$K_{w\ ii}$			4.3x10^{-18}	Not determined

Pc: confining pressure
P_f: pore fluid pressure
Pe: effective pressure, defined as $P_e = P_c - P_f$

3.1.2 Microstructural analyses

Both LSS001 and LSS002 were prepared for microstructural study. Small grains that surrounded the coarser grains of LSS001 were visible with the naked eye. This caused the coarse grains to fall out during the microstructural preparation. The sections were coated with blue epoxy to prevent any further damage.

3.1.2.1 LSS001: only dry deformation and stress-relaxation

The dry deformation microstructure of the LSS001 rocksalt is different compared to the undeformed material. The halite grains still have (sub)idiomorphic and irregular shapes and are coarse (0.7-8.3 mm) with a mean grain size of 4.6 mm (see Table 3). However, a strong increase in 90° angles of the grain boundaries of white coloured recrystallized grains is noticeable (Figure 20a, b and c). These grains overgrow the older grains. Figure 20d shows that the grain boundaries occasionally intersect at 120° triple junction, but in these cases are always coupled with open/dilated grain boundaries indicating grain boundary sliding. These open grain boundaries are recognizable by the epoxy and oil stains and are predominantly parallel to the loading direction. The injection of epoxy in the dilated areas resulted in less defined structures making the possible microstructures invisible on the photos.

In reflected light the subgrain development is strongly faded and is only found scarcely and less defined in a couple of grains along the grain boundaries as seen in Figure 20e. The subgrain have a diameter in the order of 50-100 µm. In transmitted light the dark rims along the grain boundaries are clearly visible (Figure 20f). This indicates intergranular microcracking, which explains why the section wasn't stable during microstructural preparation. The crack opening between the grains has a maximum width of 30 µm. However, if the grains overgrow an old grain, the dilation is less defined and in these idiomorphic grains and along the grain boundaries tabular and sub-spherical shaped fluid inclusions are found (Figure 20g). While the grain boundaries are dilated to different extents, the former smaller transgranular cracks (crack width is less than few micrometers) can contain fluid inclusions that are trapped by crack healing (Figure 20b, f and h). However, the abundance of fluid inclusions along the grain boundaries is less than the undeformed material and most probably no network of fluid inclusions along the grain boundaries is possible due to the amount of dilation along the grain boundaries. This indicates that fluid-assisted recrystallization was only possible at areas where the fluid did not escape along wide cracks.
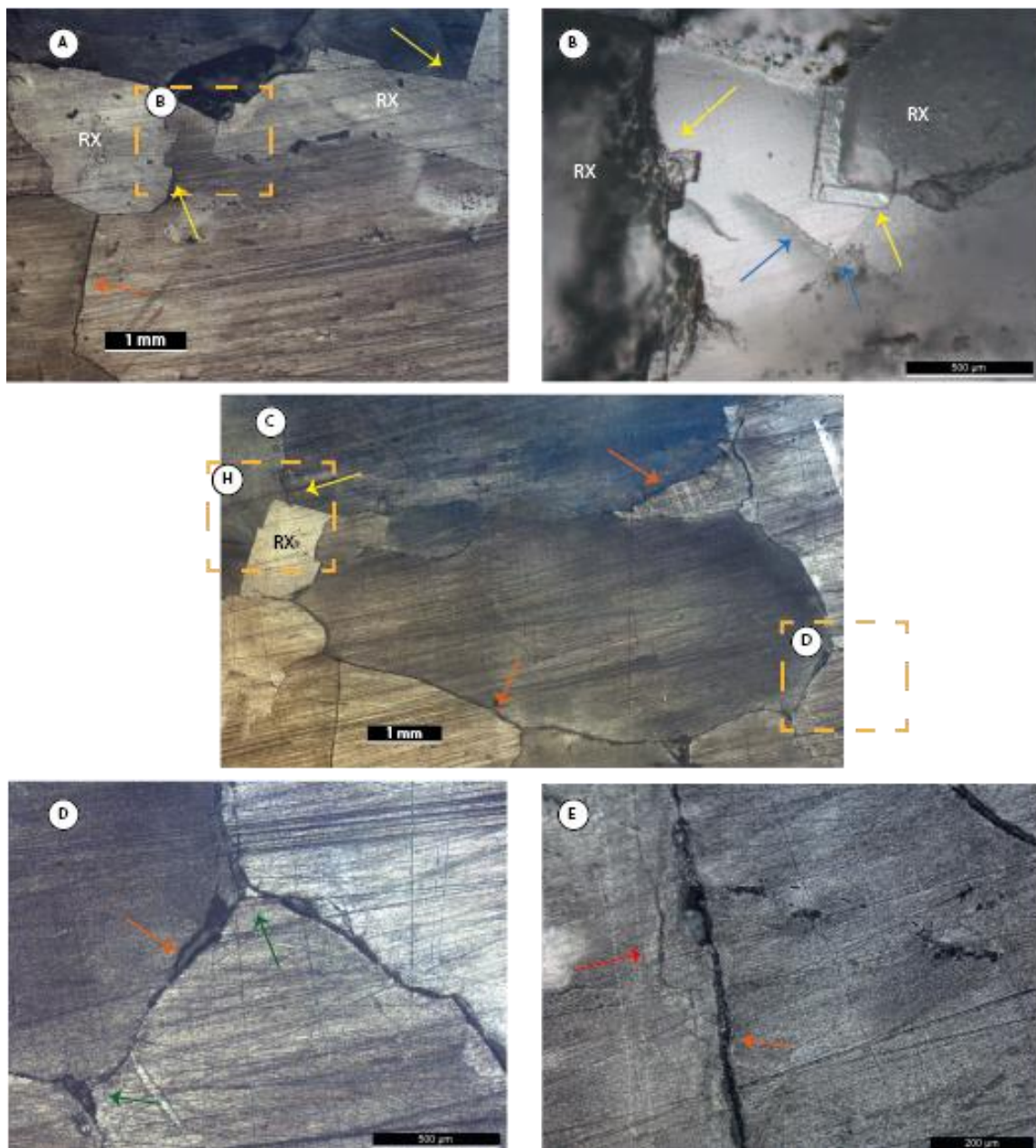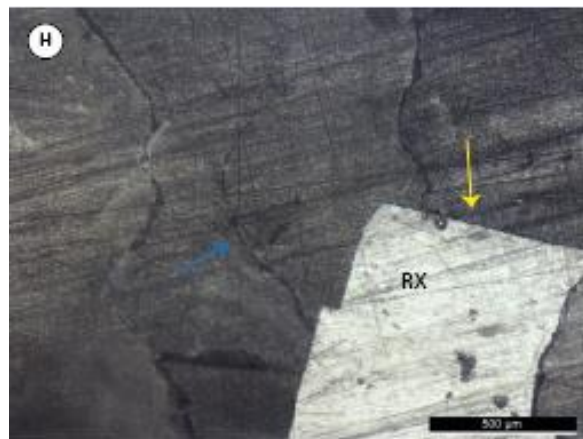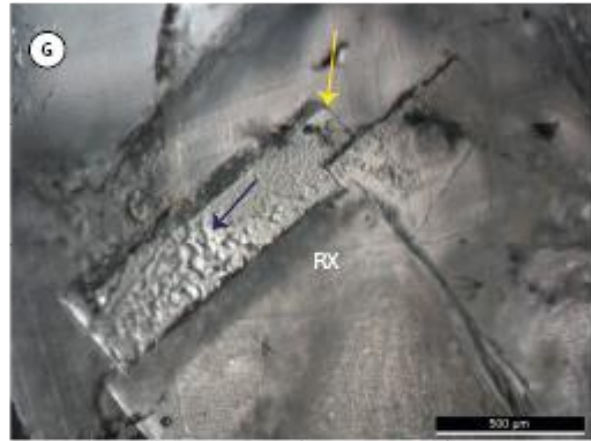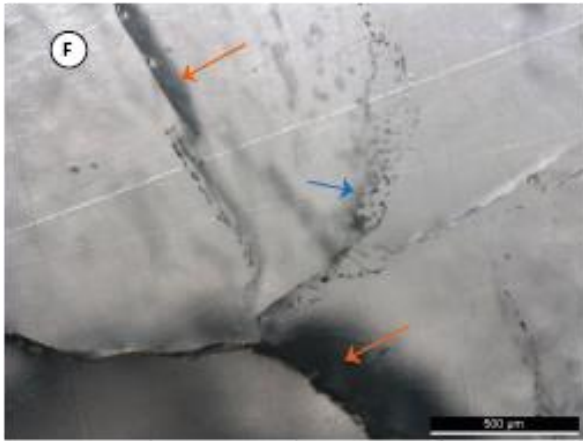
Figure 20: Photos of the dry triaxially deformed Leine Steinsalz in reflective and transmissive light a) Two grains with idiomorphic faces (yellow arrow) overgrow an older grain. b) Higher magnification photo of (a) with large fluid inclusions in the overgrowths and expanding idiomorphic grain boundaries. Fluid array in the old grain indicating the former position of a small crack (blue arrow). c) Open triple junction (green arrow), dilated grain boundaries (orange arrow) and idiomorphic faces of the intergranular overgrowth. d) Dilated grain boundaries of the triple junction of (c). e) Poorly developed subgrain structure in the left grain (red arrow) and dilated grain boundaries. f) Dilated grain boundary and partly healed cracks (blue arrow). g) Overgrowth with idiomorphic face with tabular fluid inclusions. h) A close-up of (c) of the intergranular overgrowth and the fluid inclusion trail. All photos are parallel to the dominant vertical compression direction σ_1.

3.1.2.2   LSS002: dry deformation, and dry and wet stress-relaxation

The wet triaxial deformed material LSS002 shows an increase in (sub)idiomorphic grain shapes (Figure 21a), but also extensive migrational recrystallization indicated by lobate grain boundaries (Figure 21b and c). The grains are flattened in the σ_1 compression direction and have a grain size in the range of 0.8-7.5 mm (mean grain size of 3.6 mm – see Table 3). There is no subgrain development found in the grains. The thin sections made parallel to the σ_1 compression direction clearly show both intergranular and large transgranular cracks, both dominantly parallel to the principal compression direction (Figure 21d). These cracks have a maximal length and width of approximately 3.3 mm and 75 µm respectively. However, the cracks in the thin sections perpendicular to the compression direction are less wide, scarcer and have a random orientation. Here, the dilation of the sample is more concentrated along the grain boundaries. In every thin section the cracks influence the recrystallization of the grains: in the section parallel to the principal compression direction the recrystallized grain (shown in white) grows around the transgranular crack with 90° angle (Figure 21e) and in the horizontal section the larger cracks seem to stop the recrystallization in that direction (Figure 21f). In the latter the triple junction has, similar to LSS001, open grain boundaries, but they are scarcer and the angles deviate from 120°.

LSS002 contains a minor amount of fluid inclusions along the grain boundaries and are more commonly found in the grains themselves. In transmissive light the fluid inclusions, found throughout the grain, have a tabular shape (Figure 21g). However occasionally trails of spherical fluid inclusions are visible in reflected light (Figure 21g and h). This illustrates an overprint of the old 'ghost' grain boundaries by grain boundary migration. The cracks that have a maximum width of a few micrometers

are closed by crack healing and leave a fluid inclusion trail (Figure 21e, f and h). Some cracks are only healed around the crack tip. A clear network of inclusions along the grain boundaries is absent.
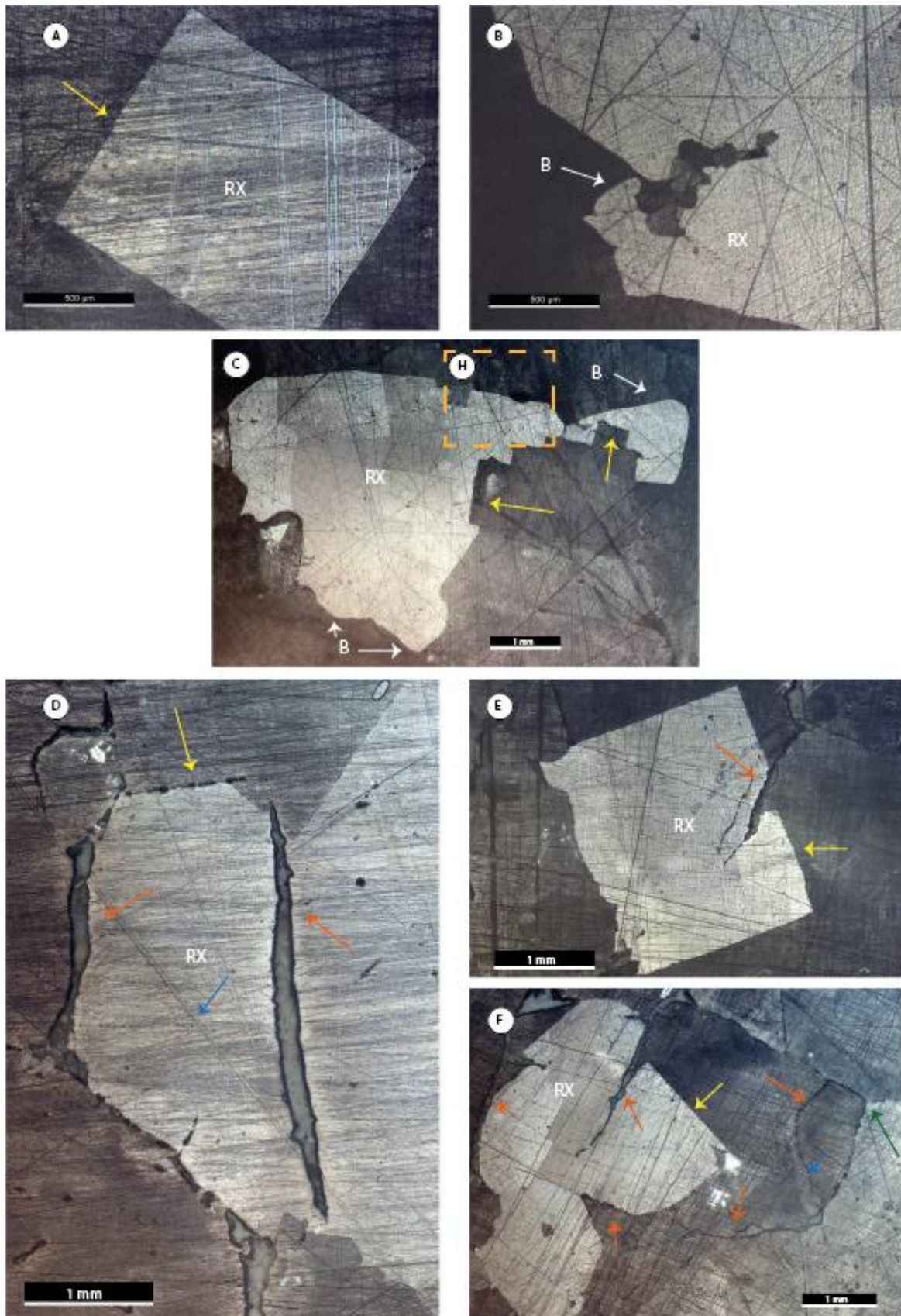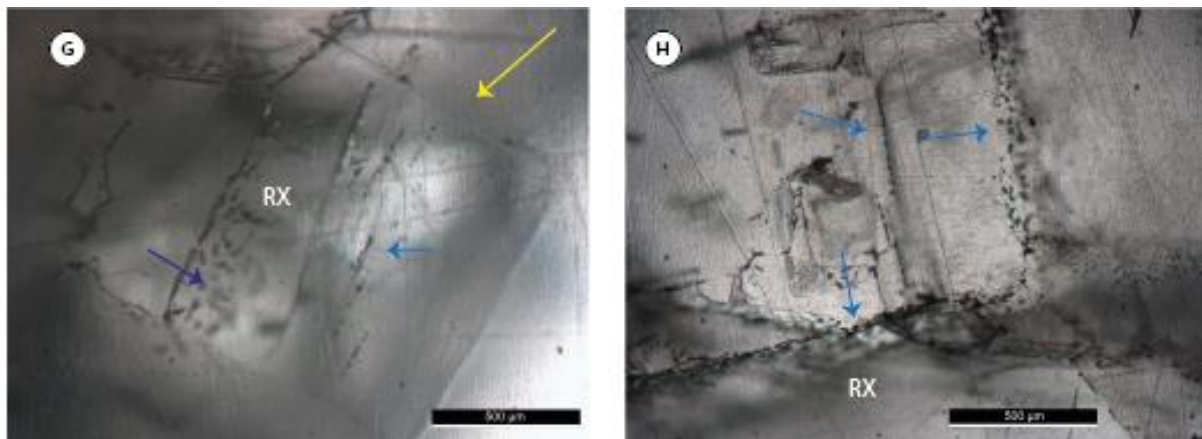
Figure 21: Microstructures of the wet triaxially deformed rocksalt in reflective and transmissive light. a) Idiomorphic grain overgrowing older grains (yellow arrow). b) Grain with no internal structure bulging (B) into another grain. c) Grain overgrowing the older grains with idiomorphic faces and also bulges (B) into the same grains d) Large transgranular cracks parallel to the compression direction (orange arrow). The left crack follows the grain boundary of the angular recrystallized grain. Trail of fluid inclusions indicating the former position of the grain boundary (blue arrow). e) The idiomorphic shaped grain overgrowing the tip of the crack and then growing around the wider parts of the crack. f) White grain bounded by cracks and growing around a crack. Open crack with a healed crack tip, leaving trail of fluid inclusions. Triple point junction with open grain boundaries (green arrow). g) Multiple arrays of fluid inclusions in an idiomorphic grain, all representing the old grain boundaries. Tabular fluid inclusions close to the new grain boundary (purple arrow). h) A higher magnification photo of (c). A 90-degree angle between two fluid inclusions arrays, representing older grain boundaries. In-between another fluid inclusion trail represents a presently-healed crack. Photos (a), (b), (d), (e) and (g) are parallel to the vertical σ_1 compression direction and photos (c), (f) and (h) are made from Section 2 and thereby the loading direction cf. Figure 14.

3.1.2.3   Summary of microstructural observations of the triaxially deformed samples

The dry LSS001 has a slightly larger mean grain size than the undeformed material, while the wet LSS002 has a smaller mean grain size (Table 3). Both of the triaxially deformed samples contain less fluid inclusions compared to the undeformed material and the inclusions do not form a network along the grain boundaries. The fluid probably partly escaped during the dry loading phase of the experiments, leaving fluid-free, dilated intergranular and/or transgranular cracks. Intracrystalline trails of fluid inclusions indicating 'ghost' grain boundaries are found in both samples, but is stronger developed in LSS002. A clear difference between the dry and wet microstructures is the less extensive recrystallization and the absence of strongly intergrown and bulging halite grains in the dry material.

The dry LSS001 does show overgrowth of the grains, but there are no bulging grain boundaries. The dilation of the dry material is strongly concentrated along the grain boundaries, but at the areas where the cracks don't form a network and/or are thin the fluid did not escape. This allowed for the recrystallization of the grains and thereby the fluid-assisted migration of the grain boundaries. The dilation of the dry material is mostly focussed along the grain boundaries by intergranular cracks, while LSS002 consists of large transgranular cracks parallel to the principal compression direction. The smaller transgranular cracks are healed completely or only partly, as the cracks can open up in the direction of the grain boundaries. The strong subgrain development of the undeformed material is not observable in the deformed samples. LSS001 does show a faint subgrain structure, but that is completely absent in LSS002.

Table 3: The microstructural grain size data of the undeformed and deformed samples. In addition, the percentage of recrystallised grains in the deformed samples is indicated. Note that LSS003 broke down when removing the sample from the apparatus, resulting in no microstructural data.

Sample	Mean grain size [mm]	Maximum grain size [mm]	Minimum grain size [mm]	Maximum recrystallized grain size [mm]	Minimum recrystallized grain size [mm]	Recrystallization percentage [-]
Undeformed	4.4	8.0	0.7	n.a.	n.a.	n.a.
Triaxial compression experiments						
LSS001	4.6	8.3	0.7	3.5	0.5	15.55%
LSS002	3.6	7.5	0.9	3.8	0.6	29.61%
Unconfined compression experiments						
LSS007	4.7	10.2	1.0	10.2	0.9	49.35 %
LSS008	3.2	6.0	0.4	3.0	0.2	30.76%

3.2 Unconfined compression experiments

3.2.1 Dry and wet mechanical behaviour

Table 1 lists the test conditions and deformation phases (in the form of a sequence of letters) of the performed unconfined compression experiments. The samples have undergone less strain than the triaxial samples as the absence of confining pressure results in more dilation of the samples, and potential brittle failure of the material. Experiment LSS003 is performed solely under dry conditions, while LSS007 and LSS008 illustrate the change in mechanical behaviour when saturated brine penetrates the sample. Experiment LSS003 is loaded two times, both followed by a period of dry stress-relaxation and LSS007 is loaded once and subsequently underwent dry and wet stress-relaxation. LSS008 underwent two loading phases up to the same peak stress where the first loading phase is followed by dry stress-relaxation and the second one by wet stress-relaxation. The mechanical behaviour of samples is shown in graphs with differential stress vs axial strain (Figure 22) and differential stress and axial creep strain rate vs time curves in Figure 23.

The dry mechanical data of LSS003, LSS007 and LSS008 show similar behaviour during the loading and the stress-relaxation, respectively presented in blue, orange and green in Figure 22. Note that the LVDT of the unconfined experiments is not positioned right for LSS003 and LSS007, resulting in no LVDT signal for the first ±2 MPa for LSS003 and no LVDT signal for LSS007 during loading and dry stress-relaxation. This led the stress-axial strain curve of LSS003 not to commence at the zero point and the axial strain data for LSS007 is calculated from the position of the Instron loading frame. Up to an axial strain ε_{axial} of 0.25-0.30% and a differential stress of 10 MPa, the near-linear trend between differential stress and strain indicates that the samples behave predominantly elastic. As axial strain keeps increasing, a sharp yield point followed and the relation becomes non-linear. Therefore, inelastic deformation becomes dominant, leading to strain hardening until the maximum differential stress of 18.6, 21.5 and 20.8 MPa is reached for respectively LSS003, LSS007 and LSS008. It should be noted that samples LSS003 (lab dry) and LSS007 (vacuum dry) show very reproducible behaviour, whereas LSS008 (vacuum dry) appears to be slightly stronger. The second loading phase of the LSS003 experiment shows work hardening up to a peak stress of 20.5 MPa at 2.1% axial strain, followed by
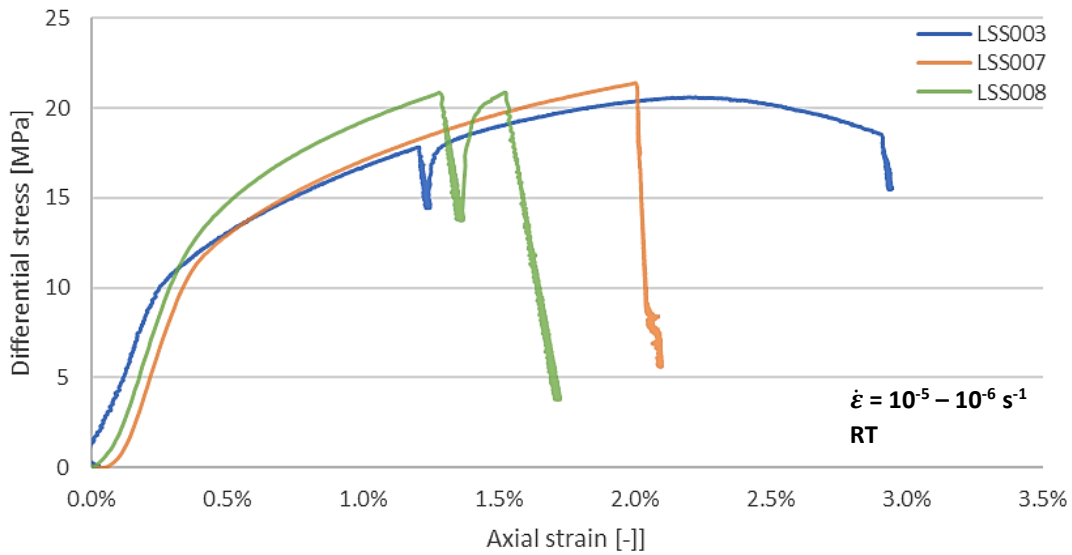
Figure 22: Differential stress vs axial strain plot of the unconfined experiments LSS003 (blue), LSS007 (orange) and LSS008 (green). Note that the LVDT of LSS003 and LSS007 is not positioned correctly, causing the axial strain curve of LSS003 not to commence at the zero point and the activation of the LVDT in the wet stress-relaxation phase of LSS007.
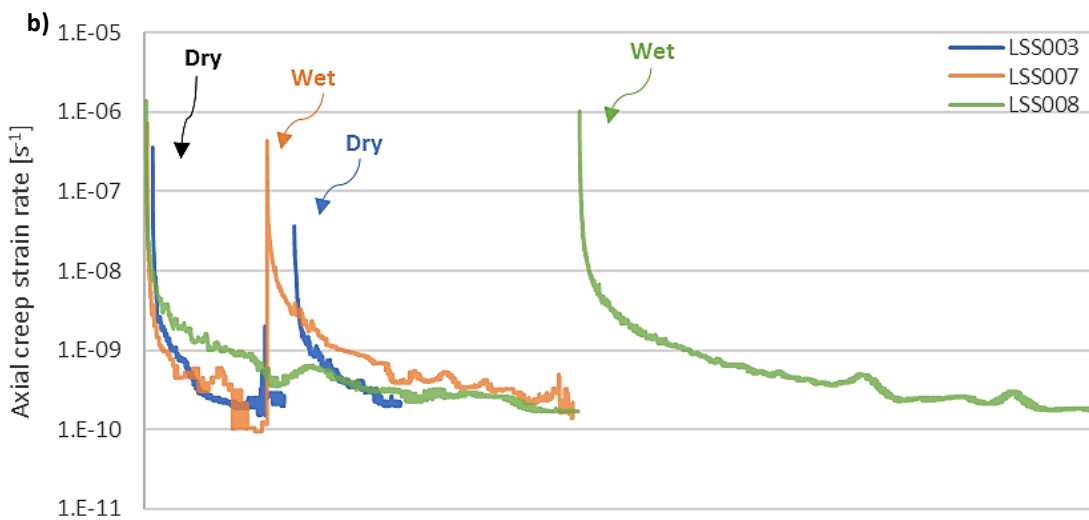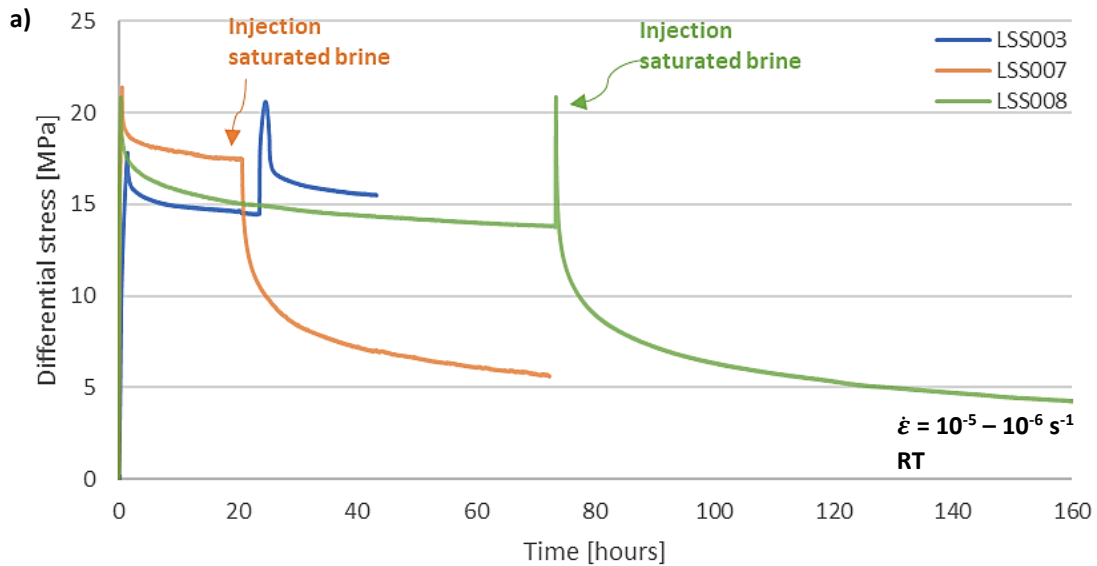

Figure 23: The mechanical behaviour of the unconfined compression experiments (LSS003: blue, LSS007: orange and LSS008: green) a) differential stress and b) axial creep strain rate (log scale) vs time.

gradual strain weakening with a 2 MPa drop in stress up to ε_{axial} = 2.9%, when grains are visibly popping out of the sample. After attaining the peak stress, the dry stress-relaxation phase is introduced. All of the dry stress-relaxation phases show a stress drop of ±4-6 MPa and a shift in axial creep strain rate $\dot{\varepsilon}_{cr}$ from ±10^{-6} s^{-1} to ±10^{-9}-10^{-10} s^{-1} over 15 hours after piston arrest (Figure 23a and b). The creep of the samples leads to a slight increase in ε_{axial} during the stress-relaxation phases (Figure 22). The stress drop of LSS008 is slightly larger and $\dot{\varepsilon}_{cr}$ stays a bit faster over time compared to the other samples. The axial creep strain rate of the second stress-relaxation phase of LSS003 already starts an order of magnitude slower than the other dry phases, but evolves towards the same rate at the end of the stress-relaxation phase. Note that the LVDT during the LSS007 experiment is just activated at the beginning of the wet stress-relaxation phase due to incorrect placement of the LVDT.

The injection of saturated brine resulted in strong weakening of the samples (Figure 23a and b). In contrast with the dry stress-relaxation phase, the stress drops significantly by ±10 and ±14 MPa for respectively LSS007 and LSS008 and $\dot{\varepsilon}_{cr}$ shifts from ±10^{-6} s^{-1} to ±10^{-9} s^{-1} over 15 hours after the injection of the fluid. Also, the axial creep strain rate stays faster for a longer time period compared to the dry stress-relaxation phase. The samples LSS007 and LSS008 continue to creep at low stresses of respectively 6 and 4 MPa, but are unloaded nevertheless to prevent further weakening and possible collapse of the samples. After unloading the samples were both still intact and brought to the low humidity room for further thin sectioning.

Plotting the logarithms of the differential stress and axial creep strain rate leads to very high n-values in the dry stress-relaxation phase for LSS003 and LSS007 (up to n = 36) (Figure 24). This implies that the differential stress is not strongly strain rate-dependent. LSS008 has the same initial response as the other two experiments, but the n-value keeps decreasing during the dry stress-relaxation phase from 33.5 to 15.2, which is notably lower than the other dry phases. The moment saturated brine is injected in LSS007 and LSS008 the flow stress becomes progressively more dependent on strain rate: the slope of the curves starts to drop over time from 15 to 4 and 17.8 to 2.3 respectively.
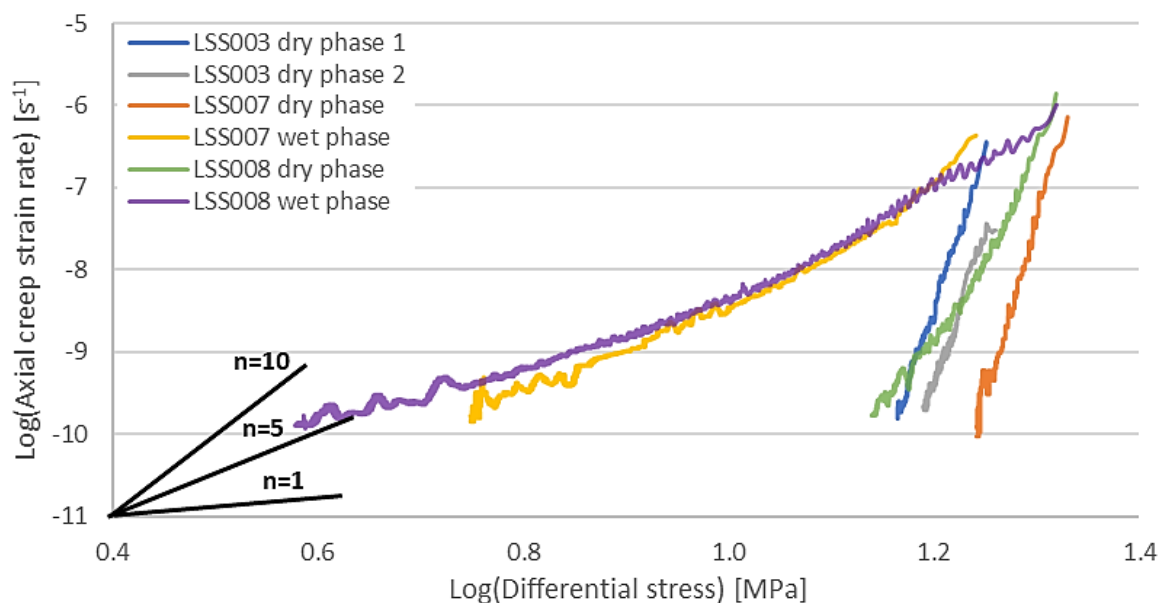

Figure 24: The log-log plot of axial creep strain rate vs differential stress for each stress-relaxation phase of the unconfined deformed samples. Three slopes representing n=1, 5 and 10 (black lines) are included as comparison between the trends.

3.2.2 Microstructural analysis

No microstructural analysis could be performed on sample LSS003, as the sample crumbled apart when removing the sample from the Instron apparatus. After cutting LSS007 and LSS008, it was chosen to apply surface impregnation to the samples to avoid the secondary polishing effect and etching damage of the surface.

3.2.2.1   *LSS007: dry deformation and stress-relaxation, followed by wet stress-relaxation*

After removal from the set-up, wet experiment LSS007 has rested on one side for 55 days. The side that was resting on the table showed efflorescence. This was not found on the side directly in contact with the air. The sections show clear grains, large enough to be identified with the naked eye. Sections parallel to the compression direction have a distinct increase in grain size towards the 'resting' side (6-10 mm at resting side, 1-5 mm non-resting side) (Figure 25a), while sections perpendicular to the compression direction show a clear band of large angular grains through the centre of the sample (Figure 25b).
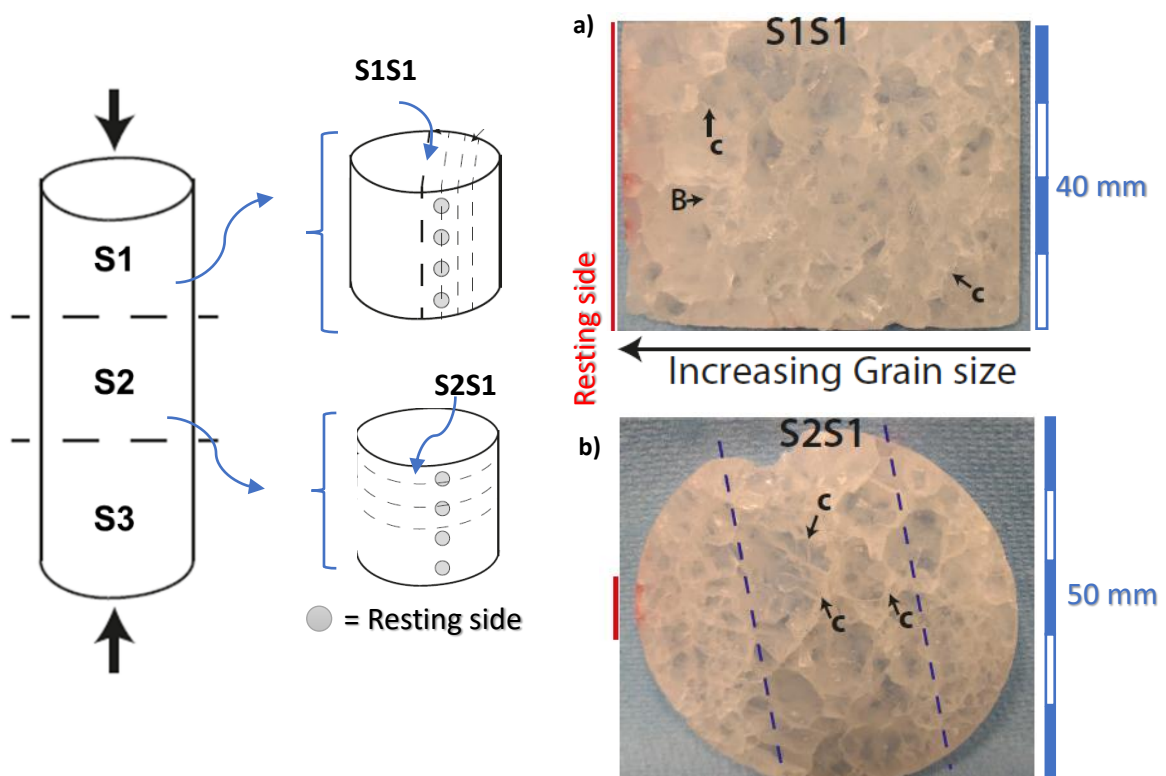
Figure 25: The thin sectioning of the unconfined deformed LSS007 where the red line indicates 'the resting side' on which the sample was laying down for 55 days. The bulging (B) of the grain boundaries and the transgranular cracks (c) are visible with the naked eye in both sections. a) The S1S1 thin section parallel to the compression direction with a substantial increase in grain size towards the resting side. b) The S2S1 thin section perpendicular to the compression direction with a band of coarser angular grains between the dashed purple lines.

The microstructure of LSS007 is dominated by grain boundary migration resulting in irregular grain shapes (Figure 26a). This bulging of the grain boundaries is more dominant than the idiomorphic overgrowth of the recrystallized grains (Figure 26b). The internal structure of some of the grains have a strong subgrain development with a mean size of 100-150 µm (Figure 26c). These subgrains are commonly found along open grain boundaries and less in the larger grains that bulge into each other. The non-dilated grain boundaries are more commonly found than the dilated grain boundaries.

However, the dilated grain boundaries are dominantly parallel to the compression direction and form a network resulting in open triple junctions along the smaller grains of the section (Figure 26d). The triple junctions insect at angles deviating from 120°. The halite grains that were positioned in the upper dry 1.26 cm of the wet stress-relaxation stage, do not show significant change compared to the wet material below. This suggests that capillary forces drew the fluid up into the dilated sample.

There are numerous intergranular cracks and occasional transgranular cracks. The intergranular cracks are wider than the transgranular cracks (respectively 20 µm and a few micrometers), where the smaller transgranular cracks are (mostly) healed, leaving a trial of spherical shaped fluid inclusions (Figure 26e). These spherical shaped fluid inclusions are also found in the non-dilated grain boundaries, while tabular shaped fluid inclusions are solely found in the grains (Figure 26f). Not every grain contains fluid inclusions, but they are always found in the newly recrystallized grains (also at the idiomorphic faces). Some grains contain fluid arrays indicating the former positions of the grain boundaries (Figure 23f and g).
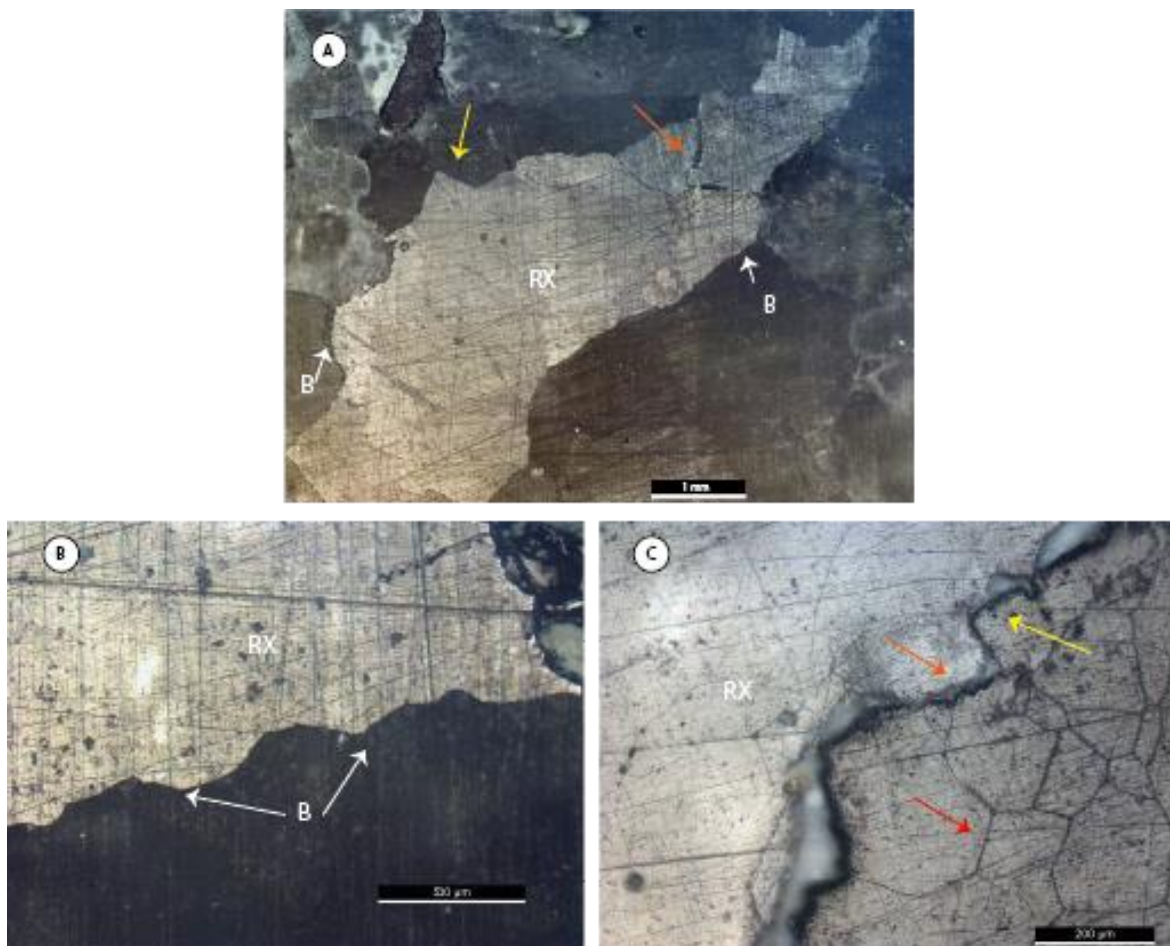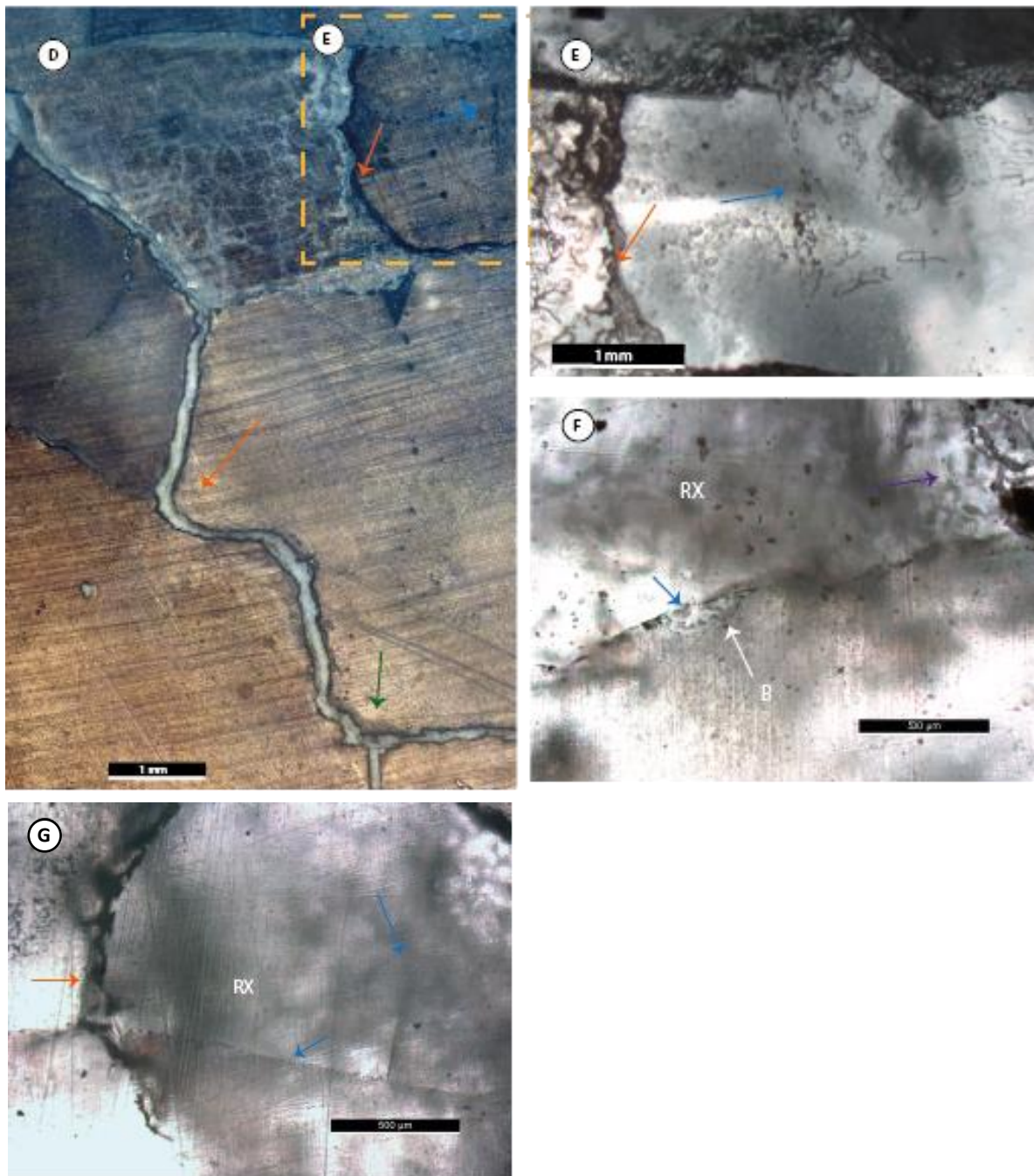
Figure 26: Photos of the wet unconfined LSS007 experiment in reflective and transmissive light. a) Grain boundary migration illustrated by the bulging grain boundary (white arrow (B)) and idiomorphic faces (yellow arrow). b) Serrated grain boundaries. c) New grain with no internal structures 'eats' the grain with a well-developed subgrain structure (red arrow). The grain boundary is slightly open (orange arrow). d) Open grain boundaries and triple junction (green arrow). e) Higher magnification of (d) in transmissive light of a fluid inclusion trail representing a healed transgranular crack (blue arrow). f) Photo (b) in transmissive light with the bulging grain boundary leaving a fluid array representing its former position plus tabular fluid inclusions in the same grain (purple arrow). g) Dilated grain boundary with two fluid arrays representing former position of grain boundaries. Photos (a), (b), (c), (f) and (g) are parallel to the vertical σ₁ compression direction and photos (d) and (e) are made perpendicular to the loading direction.

3.2.2.2 LSS008: dry deformation and stress-relaxation, followed by reloading and wet stress-relaxation

Experiment LSS008 has undergone loading twice up to the same peak stress, once followed by dry stress-relaxation and once by wet stress-relaxation. An immediate observation in reflective light is the strongly reduced grain size (0.2-6.0 mm) and lower mean grain size (3.2 mm) compared to LSS007 (Figure 27a and Table 3). The grains have dominantly lobate and bulged grain boundaries indicating dynamic recrystallization and some white coloured recrystallized grains have small idiomorphic faces (Figure 27b and c). There is no preferential growth direction or area of the recrystallized grains. Overall, there is no optical evidence for well-developed substructures in the sample. While the dry part of the sample during wet stress-relaxation is quite large (top 2.5 cm), no different structures can be found compared to the wet lower portion of the sample (Figure 27b vs c).

The transgranular and intergranular cracks are dominantly parallel to the compression direction and the transgranular cracks have a length of 1 mm and a width of 100 μm. Intergranular cracks are still the dominant crack type in LSS008 (Figure 27a and d). Some smaller grains are completely surrounded by intergranular cracks. In transmissive light tabular shaped fluid inclusions are observable in several grains (Figure 27e). The halite grains are either full of tabular shaped fluid inclusions, or have none at all. They are more commonly found in recrystallized grains. There are occasionally the spherical-shaped fluid inclusion trails next to bulging grain boundaries, representing the 'ghost' grain boundaries before grain boundary migration (Figure 27f).
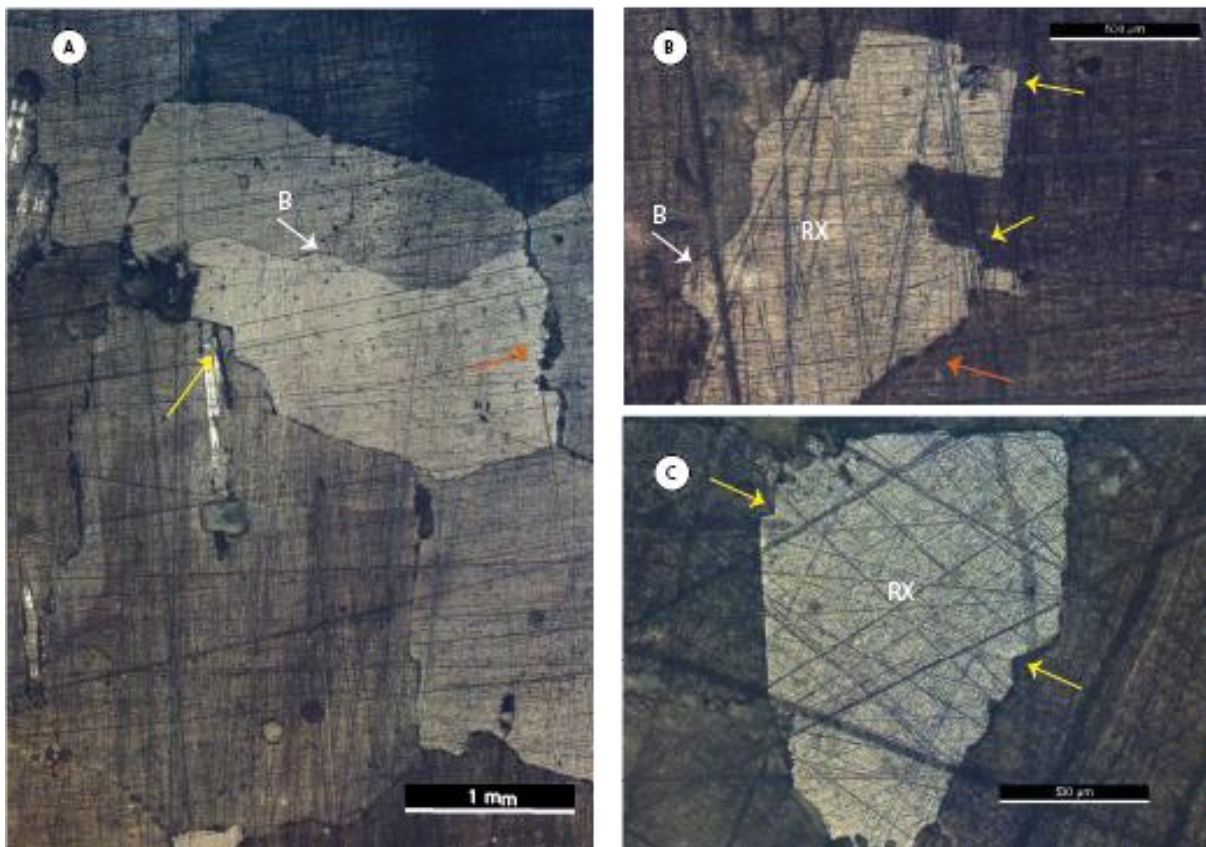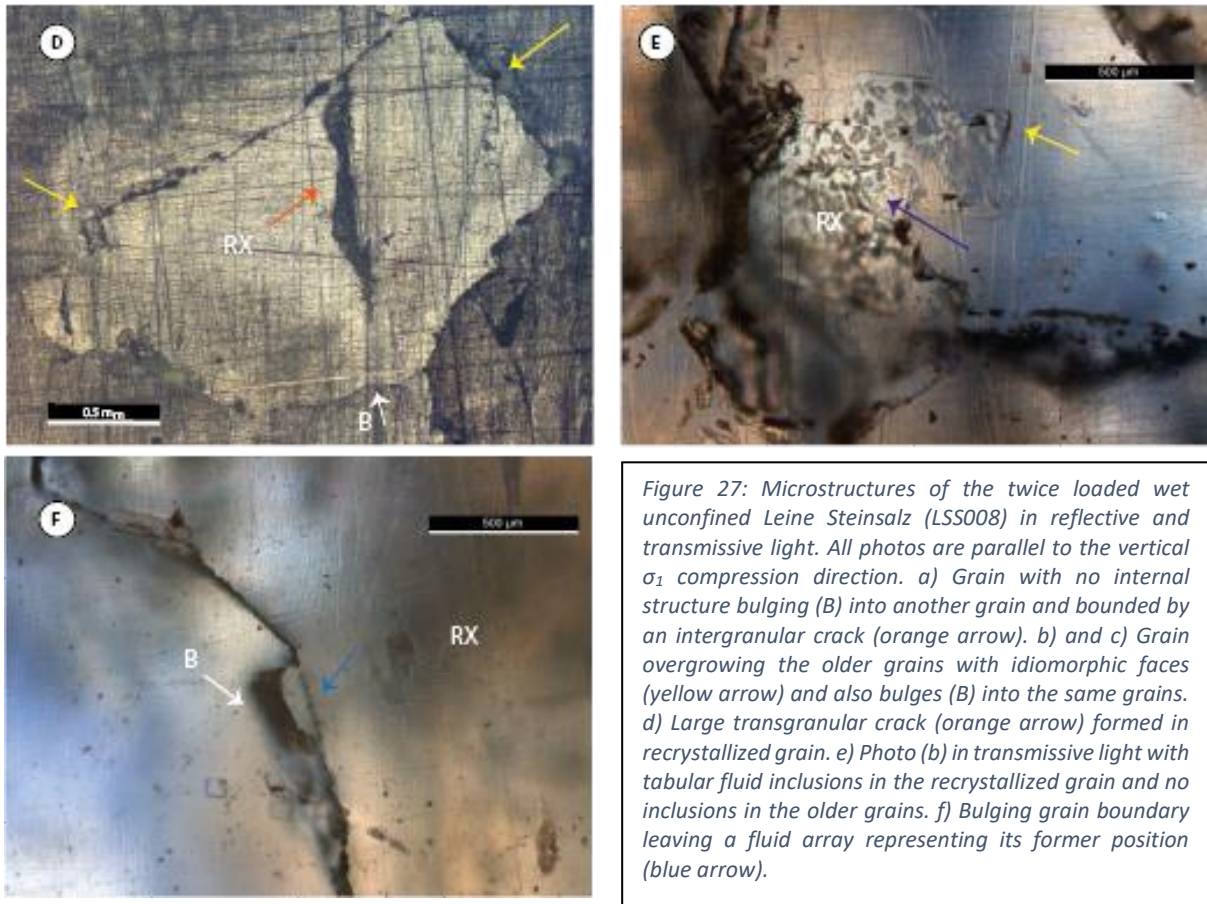
Figure 27: Microstructures of the twice loaded wet unconfined Leine Steinsalz (LSS008) in reflective and transmissive light. All photos are parallel to the vertical σ_1 compression direction. a) Grain with no internal structure bulging (B) into another grain and bounded by an intergranular crack (orange arrow). b) and c) Grain overgrowing the older grains with idiomorphic faces (yellow arrow) and also bulges (B) into the same grains. d) Large transgranular crack (orange arrow) formed in recrystallized grain. e) Photo (b) in transmissive light with tabular fluid inclusions in the recrystallized grain and no inclusions in the older grains. f) Bulging grain boundary leaving a fluid array representing its former position (blue arrow).

3.2.2.3   Summary of microstructural observations of the unconfined deformed samples

Overall, the microstructures of the unconfined experiments are similar, except for grain size and recrystallization percentage: both are larger for LSS007 (Table 3). LSS007 has a slightly larger mean grain size than the undeformed material, while LSS008 has a smaller mean grain size. This is probably the result of the resting period of 55 days of LSS007, allowing for extensive static recrystallization and thereby replacing the higher energy grains filled with subgrains. These subgrains are not seen in LSS008, but low energy grains are bulging into high energy grains. The dilation along the grain boundaries is significantly less than in the triaxial experiments, leading to more sub spherical fluid inclusions along the grain boundaries and a more defined network of inclusions. However, the open grain boundaries and transgranular cracks, dominantly parallel to the compression direction, still influence the interrelationship of the grains, where the larger intergranular cracks halt the grain boundary migration in that direction. Transgranular cracks are commonly healed, leaving fluid inclusion trails. These trails are also seen at bulging grain boundaries, representing the former positions of the grain boundaries before fluid assisted grain boundary migration.

4 Discussion

The aim of this study was to investigate the relationship between plastic flow, microcracking and solution-precipitation processes at low effective stresses for dilated coarse-grained rocksalt. To distinguish the microstructural processes and their effects, we must investigate if the saturated brine penetrating the microcracks in coarse rocksalt leads to (1) crack healing and a stable deformation rate by dislocation mechanisms and/or pressure solution, or (2) crack growth and increasing deformation rates (unstable behaviour) i.e. is there a transition in creep behaviour of rocksalt when shifting from dry to wet conditions during stress-relaxation. In this section we will compare the mechanical and microstructural data of the samples and discuss the effect of saturated brine on the type of mechanical behaviour. Afterwards, the findings will be put in a broader context of the literature.

4.1 The effect of brine on the transition of deformation mechanisms

4.1.1 Stress exponent evolution: observations from mechanical and microstructural data

During loading our experiments show an initial elastic response, followed by work hardening accompanied by the formation of a dislocation substructure (cf. Figures 16, 20e, 22 and 26c). The work hardening rate decreases with increasing strain as there is increasing effect of recovery towards higher strains. For unconfined sample LSS003 it even takes over after 3% strain (Figure 22). The flow behaviour during loading suggests that the samples deformed dominantly by plastic dislocation mechanisms. The volumetric data of the triaxial experiments indicate that with increasing axial strain there is an initial compression response that slowly converts to dilatation and dilation. During dry stress-relaxation of both triaxial experiments ε_{vol} slowly decreases, but never falls below 0.0% (Figure 16b). This can be due to the intergranular slip of salt crystals as strain accumulating process during deformation. This mechanism can form an opening of a cavity at triple junction points in the sample, that cannot be easily filled in a later stage. At the triple junctions, the vertical grain contact (parallel to the load axis) may be popped open as a result of shearing along the other two boundaries. This is confirmed by the winged crack seen in Figure 21d. The stress drop during stress-relaxation is significantly less for the unconfined experiments, when comparing to the triaxial compression experiments.

The permeability measurements done in LSS002 show that the sample was not permeable until the confining pressure was decreased from 12 to 10 MPa (Table 2). However, dilation is noted before the confining pressure was decreased (Figure 16b). According to Peach & Spiers (1996) minor dilation (<0.25%) can already lead to a significant increase in permeability. This is not recorded in the LSS002 experiment. An explanation for this can be that due to the amount of stress on the sample and thereby on the glass fibre and Teflon sheets, the glass fibre sheets fully fused with the sample, allowing the Teflon sheets to flow into the cracks on top and bottom of the sample. This can clog up the formed microcracks at the ends of the sample, which can prohibit the fluids to enter the sample. The decrease in confining pressure could have reopened these microcracks allowing the fluid to penetrate the sample. As the LSS002 experiment continued and saturated brine is introduced, the permeability increased in an order of magnitude from 9.48×10^{-19} to 4.3×10^{-18} m^2 (both upper limits of the measurements). However, there was no immediate response in permeability as the brine was injected.

As described in Section 2.2.4, the differential stress-strain rate data have a relation that can be described with the conventional power law creep in the form of $\dot{\varepsilon} = A(T)\sigma^n$. The larger the n-value is, the less the dependence of stress on strain rate is. Since each deformation mechanism has its own stress dependence, i.e. its own (range of) n-values, this makes it perfect for assessing the microphysical processes dominating deformation. The n-value for steady state flow has a range of ~1

up to 10+. Grain size sensitive (GSS) processes like pressure solution have a n-value of ~1 (Muhammad, 2015; Spiers et al., 1990). N-values which are larger than 3 can generally be described by grain size insensitive (GSI) creep, where 3 < n < 6 and n > 10 respectively relate to dislocation climb and cross-slip (Carter et al., 1993) and dislocation glide (De Bresser et al., 2002). The commonly used creep rate equations of cross slip (cs), dislocation climb (cl) and pressure solution (ps) are:

$$\dot{\varepsilon}_{cs} = 1.6 * 10^{-4} \exp(\frac{-68100}{RT})\sigma^{5.3} \qquad Carter\ el\ al.\,(1993) \qquad (11)$$

$$\dot{\varepsilon}_{cl} = 8.1 * 10^{-5} \exp(\frac{-51600}{RT})\sigma^{3.4} \qquad Carter\ el\ al.\,(1993) \qquad (12)$$

$$\dot{\varepsilon}_{ps} = 4.7 * 10^{-4} \exp(\frac{-24530}{RT})\frac{\sigma}{Td^3} \qquad Spiers\ et\ al.\,(1990) \qquad (13)$$

Where strain rate $\dot{\varepsilon}$ is given in s^{-1}, R is the gas constant [J/(mol.K)], T the absolute temperature [K], σ the flow stress [MPa] and d the grain size [mm]. The theoretical total creep rate is equal to:

$$\dot{\varepsilon}_{total} = \dot{\varepsilon}_{cs} + \dot{\varepsilon}_{cl} + \dot{\varepsilon}_{ps} \qquad (14)$$

Since our experiments did not achieve steady state creep and also underwent strong work hardening resulting into the tangling of the dislocations, the n-values of the dry stress-relaxation phase are noticeably higher (n=9-35) than expected at steady state creep. The n-values first decrease rapidly as the dry relaxation continues and the creep rate decreases and become approximately constant as steady state approaches (Figure 28). This initial decline in n-value is stronger for the triaxial experiments than the unconfined experiments with an exception for LSS008. LSS008 behaves differently than the other unconfined experiments in the dry phase as the vacuum was poor during deformation, meaning that the room humidity could affect deformation. During the experiment the room humidity of the lab was 1.5 times as high (average of 45%) as normal (30%) (Figure 29) and as salt is hygroscopic and a miniscule amount of atmospheric water can affect the deformation drastically, resulting in a change in the relaxation rate of the experiment. Although LSS003 was
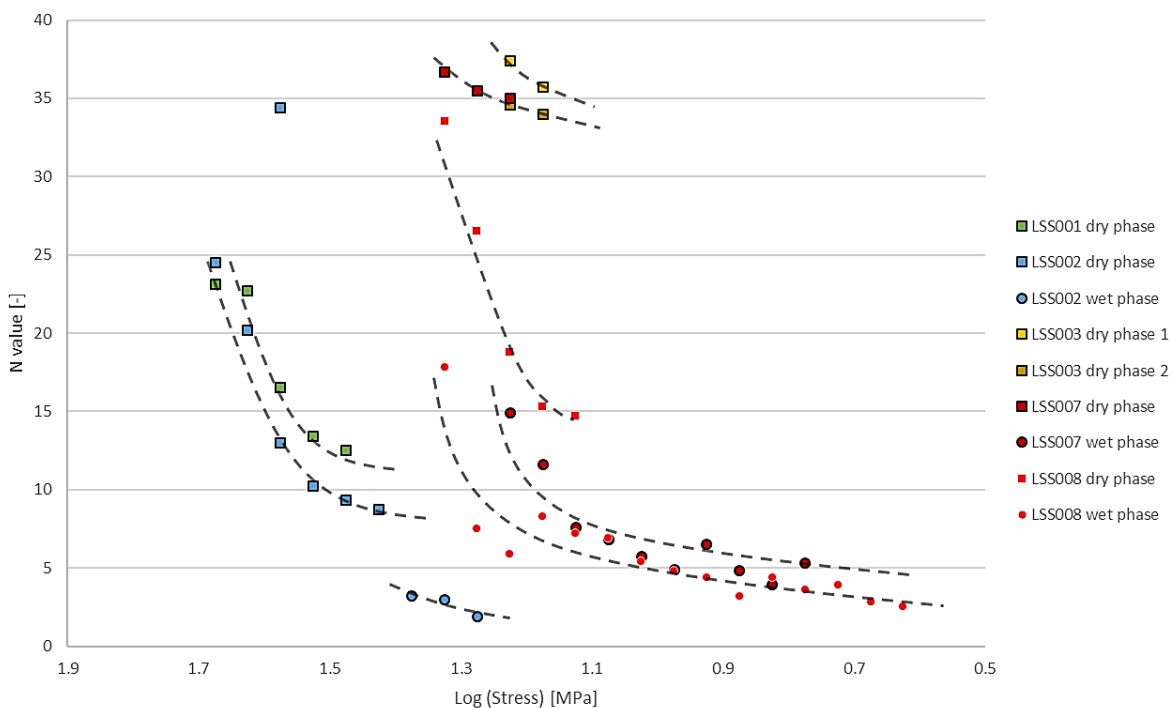

Figure 28: The evolution of the n-values during stress-relaxation phases. The mean n-value was calculated for every Log(stress) 0.05 MPa interval. The dotted lines illustrate the overall trend of the n-values vs the stress drop for every stress-relaxation.
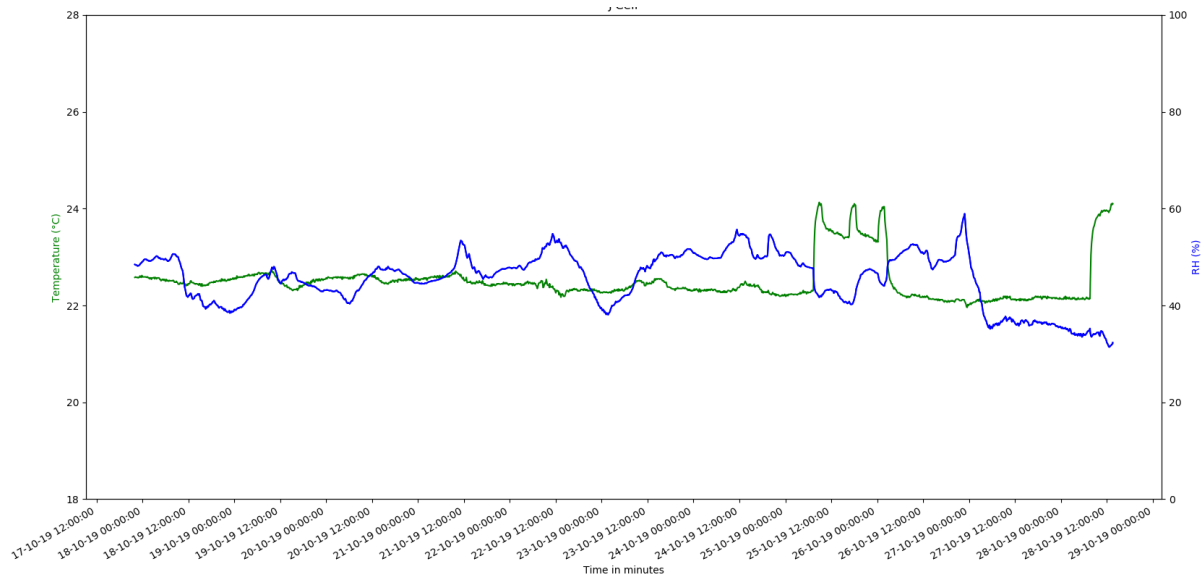
Figure 29: The temperature and room humidity during the loading and dry stress-relaxation phase of the unconfined LSS008 experiment. Due to the poor vacuum of the experiment, it is likely that the room humidity affected the creep of the sample to some extent.

performed under lab air conditions, it does not seem to react the same way on the room humidity as LSS008. As we do not have any room humidity data during the LSS003 experiment, we can only speculate that the room humidity was much lower during the LSS003 experiment. The dry phase of LSS008 behaves more like the dry stress-relaxation phases seen in the triaxial experiments. It is likely that the intergranular water didn't fully escape for all of the triaxial experiments and initiates localized deformation. It could be that the effect of a high room humidity on the creep rate is similar to the effect of remaining intergranular water. This would mean that intergranular water did completely escape for the unconfined samples LSS003 and LSS007. Still, these obtained preliminary n-values indicate that dislocation glide as dominant deformation mechanism and thereby a near stress-independent strain rate in the dry phase. This corresponds to the expected deformation mechanism according to the deformation map of Spiers & Carter (1998) (Figure 30) and suggested for dry halite by Poirier (1985). The microstructures of the dry phases of the experiments i.e. dislocation substructures are (partly) overgrown by the recrystallized grains. A more intense subgrain structure was expected for LSS001, however the deformation conditions were around the transition of compaction to dilation, resulting in a semi-disruption of the intracrystalline fluid films. If the LSS001 sample was fully in dilatant conditions, the intergranular fluid would have escaped along the grain boundary microcracks, prohibiting fluid-assisted recrystallization (Peach et al., 2001). The LSS001 and LSS007 samples weren't immediately sectioned, allowing for mechanisms like static recrystallization to occur, resulting in an increase in mean grain size as a consequence.

Once saturated brine is injected into samples LSS002, LSS007 and LSS008, the same type of n-value evolution for the dry phases is seen for the wet phases: a strong decline in n-value in the beginning of the relaxation phase and slowly approaching a more stable value as steady state approaches (Figure 28). The flow stress becomes progressively more dependent on strain rate: the n-value gradually drops with decreasing stress and strain rate from 3.2 to 1.9, 14.9 to 4.0 and 17.8 to 2.3, respectively for LSS002, LSS007 and LSS008, over time, illustrating the effect of brine on the change in dominant deformation mechanism. This transition from a dry to a wet environment is also seen when plotting the wet data on the deformation map (Figure 30). At low stresses and low strain rates (below 10^{-9} s^{-1}) the σ-$\dot{\varepsilon}$ dependence becomes increasingly linear, however solely grain sensitive flow is never reached (n-value ≠ ±1) (Figures 19 and 24). This is confirmed by the experimental results
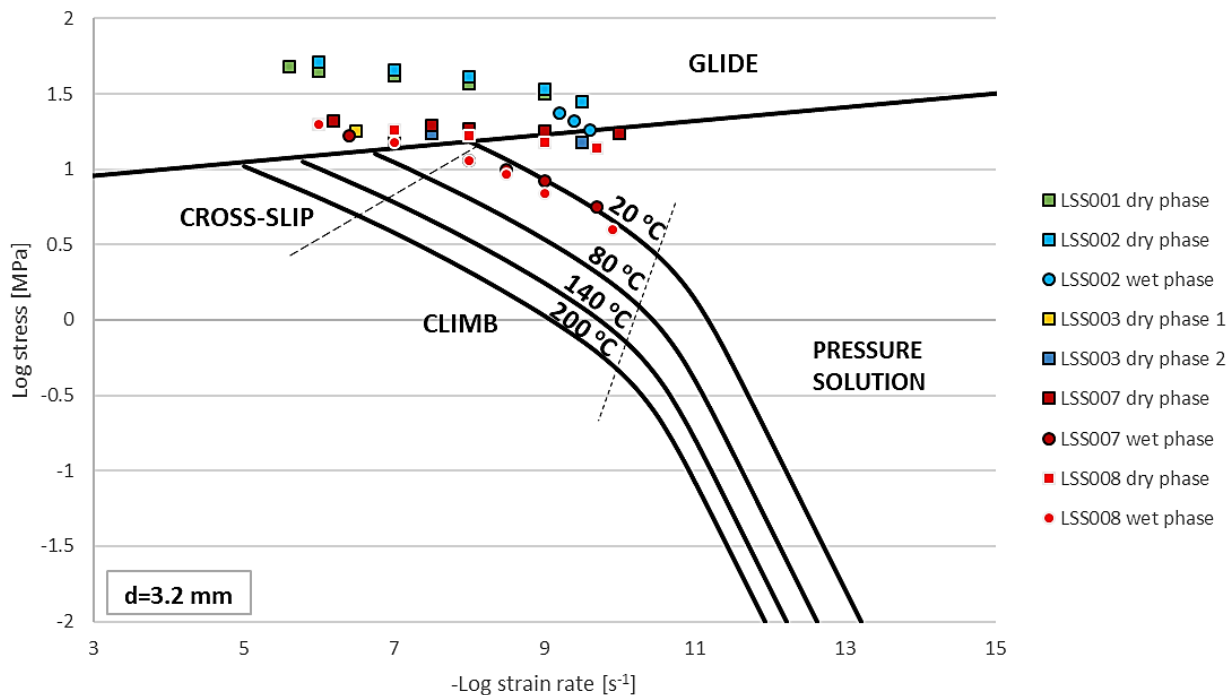
Figure 30: The deformation map for natural rocksalt adapted from Spiers & Carter (1998) with the experimental results of the relaxation phases presented in this study. The dotted lines indicate the transition in dominant deformation mechanism from cross-slip to climb and from climb to pressure solution. Note that the mean grain size of LSS008 (d=3.2mm) is taken as reference. The deformation map will be different for every grain size as pressure solution is a grain size sensitive process.

that do not plot in the pressure solution regime of the deformation map. Furthermore, steady state flow was not reached in all of the wet stress-relaxation phases, as for the unconfined experiments the stress was so low due to the large amount of weakening, that the experiment had to be terminated to preserve the samples. LSS002 and LSS008 both showed grain size reduction (Table 3), absent subgrain development (Figures 21a and 27a), fluid inclusion trails representing 'ghost' grain boundaries (Figures 21g and 27f) and strong irregular/lobate grain boundaries (Figures 21b and 27a), all indications for extensive recrystallization where the strain hardened grains are replaced by grains with a low internal energy. Multiple studies have shown that in deformed natural and synthetic samples idiomorphic crystal faces of the recrystallized grains, as seen in every section of this study, are conceivable (Peach et al., 2001; Ter Heege et al., 2005a; Urai et al., 1986). The new grain boundaries and recrystallized grains were full of fluid inclusions suggesting fluid assisted grain boundary migration (Figure 27e). An estimate of the rate of recrystallization can be made by dividing the recrystallized grain size (Table 3) by the duration of the wet phase of the experiments (2-7 days) and the total time of the 'resting' phase. This results in an average recrystallization rate of 0.35 mm per day for LSS002 and LSS008 and 0.15 mm per day for LSS001 and LSS007 as they are not sectioned immediately. When saturated brine is present in the sample, the narrow (parts of the) cracks are healed, leaving a fluid trail behind (Figure 21f). Some inter- and transgranular seem to be too wide to overcome by diffusive transfer via the fluid film, prohibiting grain boundary migration, pressure solution and crack healing as healing mechanisms (Figure 21d).

4.1.2 Rheological weakening by the injection of saturated brine

It is important to understand what can significantly influence the dislocation mobility of rocksalt when saturated brine is introduced into the sample. There are multiple processes that could have caused this rapid acceleration in strain rate and increase in stress-strain rate dependence. The enhancement of the dislocation mobility can be due to hydrolytic weakening (intracrystalline water), the saturation difference between the saturated brine and the deformed sample, the increased likelihood of grain size sensitive processes like pressure solution by intragranular cracking, stress enhancement by microcracking, the effect of subcritical crack growth and/or the diminishing of the dislocation density by activating dynamic recrystallization. In this section I will systematically investigate each of these hypotheses to determine the main mechanism leading to weakening in the presence of brine.

4.1.2.1   The effect of water incorporation in the grain structure: hydrolytic weakening

Trace amounts of brine can affect the type of salt creep as fluid films allow for fast diffusional transfer enhancing dynamic recrystallization and water can be incorporated in the grain structure of salt (Urai et al., 1986). Exclusively dry microstructures are impossible to achieve in natural salt, as the water content of natural salt is always higher (>9 ppm) than the threshold concentration of 5 ppm (Ter Heege et al., 2005b). It is observed that the undeformed samples are full with fluid inclusions in the grain boundaries and in the grain structure. The trace amounts of brine along the grain boundaries imply that grain boundary migration would be possible in non-dilatant conditions (Peach et al., 2001) which is seen in the triaxial experiment LSS001 containing recrystallized grains full with fluid inclusions (see Figures 20g). However, although some trace amounts of fluid are found to be structurally incorporated in the salt grains, there is no indication in the presented samples or evidence in the literature that the intracrystalline water affects the dislocation mobility in rocksalt.

4.1.2.2   The effect of the enhancement of solubility of deformed grains

Another candidate for the increase in strain rate and decrease in n-value when injecting saturated brine is the dissolution of the stressed sample into the fluid as material under stress has a slightly higher solubility than unstressed material. For this model, the experiment is defined as a closed system and an initial state of the material can be described by spherical grains with a simple cubic packing (Figure 31). As stress is applied to the grains a gradient in chemical potential and in solubility of the solid between the stressed grain contact and the unstressed pore wall area starts to develop (Pluymakers & Spiers, 2014; Spiers et al., 2003). If there is a diffusive medium, such as a pore fluid, the material will dissolve at the stressed grain contacts and precipitate on the stress-free pore walls. This will lead to the growth of intergranular contact areas during deformation (Renard et al., 1999). Since the sample used in this study continue to compact during stress-relaxation, interfacial surface energy between the solid and liquid will not be of importance when discussing the chemical potential gradient during pressure solution (Spiers et al., 2004). The chemical potential energy of the stressed grain boundaries and pore walls can respectively be expressed by:
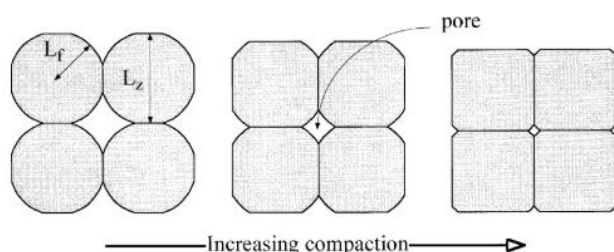

Figure 31: A cubic packed cluster of spherical NaCl grains. As compaction, and thereby pressure solution, goes on the grain shape eventually evolves to flattened grain boundaries resulting in the decrease in porosity (Renard et al. 1999).

$$\mu_{gb} \approx f + \sigma_n \Omega \tag{15}$$

$$\mu_{pw} \approx f + P_f \Omega$$

Where f is the Helmholtz free energy of the solid [J], σ_n the normal stress on the grain contact [MPa], P_f the pore fluid pressure [MPa] and Ω the molar volume of the solid phase [m³]. Provided that the stress is high enough, resulting in $\mu_{gb} - \mu_{pw} > 0$, then the driving force for pressure solution can be described by $\Delta\mu = \mu_{gb} - \mu_{pw}$. It is generally accepted that we can neglect the difference between Helmholtz energy within the grains (de Meer & Spiers, 1997). If we assume free pore walls, then the normal chemical potential can be defined as:

$$\Delta\mu_n = \Delta\sigma_n \Omega \tag{16}$$

The chemical potential of the dissolved material and its concentration (C [m³/m³]) for ideal mixtures can be described by:

$$\mu = \mu_o + RTln\frac{C}{C_o} \tag{17}$$

$$\Delta\mu_n = RTln\frac{\Delta C}{C_o}$$

$$\frac{\Delta\mu_n}{RT} = \frac{\Delta C}{C_o} \tag{18}$$

where R is the gas constant [J/(K.mol)], T the absolute temperature [K], ΔC the enhancement of the solubility of the solid at stressed grain contacts [m³/m³] and C_o the solubility of an unstressed reference condition [m³/m³] (Pluymakers & Spiers, 2014; Spiers et al., 1990). Equation (18) gives the relative stress-induced solubility enhancement in relation to the chemical potential.

Table 4: Values of terms appearing in the pressure solution equations

SYMBOL	VALUE	SOURCE
$\Delta\sigma_n$	20.8 x10⁶ Pa	Presented data LSS008
R	9.31 J/(mol.K)	Universal gas constant
T	295.35 K	Presented data LSS008
Ω	2.693 x 10⁻⁵ m³	Spiers et al. (1990)
C_o	0.165 m³/m³	Koelemeijer et al. (2012)

If we calculate the chemical potential with the presented values of Table 4 and equation (16), we obtain $\Delta\mu_n = 560.14\,J$. Substituting the chemical potential term into the relative stress-induced solubility enhancement equation (18), we obtain: $\frac{\Delta C}{C_o} = 0.203$ and $\Delta C = 0.033$ m³/m³. This means that per 100 ml saturated brine an additional NaCl mass of 7.1 g can be dissolved at the high-stressed grain boundary contacts. Comparing the initial and final sample volumes of the unconfined samples, the porosity increases by 20 times from 0.05% to approximately 1%, with is an increase in sample volume of 1.9 cm³ for LSS008. Therefore, we can assume that a maximum of 1.9 ml of brine went into the sample, resulting in a maximum of 134.9 mg of salt could have been dissolved. The axial strain increase during wet stress-relaxation of experiment LSS008 is 0.19%, which is equal to a shortening of the sample of 0.23 mm. If this would be solely due to mass loss by dissolution, we would expect that at least 975 mg of the sample would have been dissolved. The small amount of mass loss of the sample due to enhancement of solubility of deformed grains cannot explain the strain increase when saturated brine is injected.

All of the samples presented in this study have test conditions in the dilatant field, or right on the boundary of the transition from compaction to dilatancy. In the dilatant field the number of microcracks, as well as permeability, increases. It is important to understand to what extent the microcracks influence the rate of the possible deformation mechanisms. Microcracks can impact the deformation behaviour by enhanced pressure solution rate and stress enhancement. The geometry of the microcracks can also change due to subcritical crack behaviour and if the cracks are wide enough (including the corresponding fluid film), diffusive mass transfer processes can be prohibited. These possibilities are investigated below.

Figure 21e shows a recrystallized grain with a discontinuous transgranular crack of which the narrower part of the crack is healed while the wider parts of the crack are not. Similarly, possible healing mechanisms can be crack healing, fluid-assisted grain boundary migration and pressure solution followed by necking, respectively driven by changes in the radius of curvature of the salt/brine interface at any point along the crack, Helmholtz energy and normal stress. If a transgranular crack completely cuts through a grain then the mean grain size of the sample will be lowered. This could lead to grain size sensitive flow mechanisms like pressure solution, in which the smaller the grain size, the faster the pressure solution creep is (see strain rate equation (13) from Spiers et al. (1990)). If we assume that the crack goes right through the middle, the grain size will be halved, leading to:

$$\dot{\varepsilon}_{ps}^* = 4.7 * 10^{-4} \exp(\frac{-24530}{RT}) \frac{\sigma}{T(0.5d)^3}$$

$$\dot{\varepsilon}_{ps}^* = 8 * \dot{\varepsilon}_{ps} \tag{19}$$

Where $\dot{\varepsilon}_{ps}^*$ is the microcracking-enhanced pressure solution creep rate, i.e. by grain size (d) reduction, and $\dot{\varepsilon}_{ps}$ is the pressure solution creep rate equation of Spiers et al. (1990) (equation 13). This results in an increase of almost an order of magnitude in the strain rate if controlled by pressure solution. This effect will increase further if the rocksalt is dilated even further e.g. if the grains break into four pieces then the rate of pressure solution $\dot{\varepsilon}_{ps}^*$ become 256 times $\dot{\varepsilon}_{ps}$ (which is equal to an increases of two orders of magnitude). The cracks can have the possibility to have grain-to-grain contacts in the narrower part of the cracks, i.e. where crack planes are touching. These narrow parts of the crack are found when the crack starts off parallel to the principal compression direction, but later curve and end up perpendicular to the principal compression direction (see Figure 21f). These grain-to-grain contacts are especially important for pressure solution as stress concentrates on these contacts. As the rate of pressure solution increases rapidly if there is microcracking, it will become the dominant deformation mechanism at higher strain rates than previously assumed. Therefore microcracking-enhanced pressure solution must be taken into account when constructing a model to describe the steady-state creep of dilated rocksalt.

The resulting permanent damage of cracks that are too wide to heal, influences the type of deformation mechanism by enhancing the stress. As microcracks start to form, the porosity of the sample increases and therefore the surface area of the sample will decrease. This will enhance the stress as it is equal to force over area. As established in Section 4.1.2.2. the porosity of the unconfined samples increases by 20 times from 0.05% to approximately 1%. This leads to:

$$\sigma_{enh} = \frac{F}{A*(1-\varphi)} = \frac{1}{1-\varphi} * \sigma \tag{20}$$

Where σ_{enh} is the enhanced contact stress for dilated samples [MPa], F the applied force [N], A the surface area [mm^2], φ the porosity of the sample [-] and σ the applied stress prior to porosity changes [MPa]. For the used Leine Steinsalz samples, filling in equation (20) leads to $\sigma_{enh} = 1.01 *$

σ.. At the stresses investigated and considering the amount of dilation noted in the performed experiments, stress enhancement plays a small role in the weakening of the sample when saturated brine is injected. However, this effect will become more extensive if the hydrostatic stress and porosity increase even more, which is the case for the damage zone during well bore placement: the damaged zone can have a porosity of 5% at the in-situ isotropic stress is 53 MPa at 2500m depth (established from Orlic et al. (2019)). Therefore, even if stress enhancement doesn't affect the presented experimental results extensively, it must be certainly taken into consideration when constructing a model to describe the steady-state creep of dilated rocksalt.

As said before, during the loading of the samples microcracks start to form. At the crack tip, stress localization takes place due to local elastic strain. The Griffith theory quantifies the critical crack tip stress magnitude, meaning whether failure occurs at the given conditions (Griffith, 1920). Under dry conditions, crack propagation will always be critical, which means that the crack propagation is abrupt. The Griffith theory states for critical behaviour is given as:

$$K_c = \left[\frac{\sigma_r}{\sqrt{2}} \sqrt{\pi a} \right]_{crit} = \sqrt{\gamma_s E} \tag{21}$$

Where K_c represents the critical stress intensity factor, σ_r the remote applied stress [Pa], a ½ of the crack width [m], γ_s the specific surface energy [J] and E the Young's modulus [Pa]. If the right side of the equation is equal to or higher than K_c, then abrupt failure will occur. However, the value for K_c decreases when in a chemically active environment, such as the addition of water, as it lowers the surface energy γ_s of the cracks due to the adsorption of water molecules. This means that in wet environments less stress is needed to propagate the cracks. Therefore, the injection of saturated brine can lead to subcritical crack behaviour, i.e. crack propagation at stress conditions lower than those suggested by Griffith's theory. This could explain the permeability increase of LSS002 during the wet stress-relaxation phase (cf. Table 2). As flow stress is rapidly decreasing during the wet stress-relaxation phase subcritical crack behaviour will come to a halt and healing mechanisms, driven by the change in Helmholtz energy and normal stress, will take over at the narrow parts of the cracks. However, as said before, some parts of the cracks, and thereby the associated fluid film, are too wide too overcome by diffusive processes, resulting in crystal growth around the cracks by the recrystallized grains and/or in inhibition of recrystallization in that direction as indicated by the overgrowths of Figure 21f. Therefore, the geometry of the cracks does influence the flow of the salt and subcritical crack behaviour must be taken into account when discussing dilated natural rocksalt. More experiments are required to quantify the possible effect of subcritical crack growth, as no dry microstructures before the injection of saturated brine could be saved to compare the geometry of the cracks in dry and wet settings.

4.1.2.4 The effect of activating fluid-assisted dynamic recrystallization

Houben et al. (2013) states that under dry conditions diffusive mass transfer and recrystallization are slow. This is in agreement with our dry stress-relaxation phases, were the strain rates are significantly lower compared to the wet stress-relaxation phase. The strain increase during the wet relaxation phases is potentially due to processes like dynamic recrystallization and solution-precipitation creep and the accompanying redistribution of the grains. The thermodynamics of dynamic recrystallization is based on the removal of high energy grains i.e. with well-developed dislocation substructure, by the growth of grains with a limited internal structure by grain boundary migration. In wet settings, grain boundary migration is very fast, leading to a rapid decrease in flow stress and weakening of the sample as the resistance to deformation diminishes by reducing the dislocation density. We can assume that at the peak stress the microstructure was fully hardened and

during wet stress-relaxation was party replaced by recrystallization. However, some grains were very dark after etching, making it impossible to accurately determine the internal structure of the grains. Therefore, the recrystallization percentage of the samples can be higher than determined (see Table 3).

Ter Heege et al. (2005a) and De Bresser et al. (2001) suggest that the rheology of wet rocksalt at steady state creep can be described by a combination of grain size insensitive (GSI) dislocation creep and grain size sensitive (GSS) diffusion creep. They state that in an initially coarse material, dislocation creep co-occurring with grain boundary migration, including bulge nucleation and subgrain rotation nucleation, produces grain size reduction. The nucleation of new grains by rotation recrystallization can form fine-grained grains with a maximum grain size of 200 μm (i.e. the maximum subgrain size of undeformed Leine Steinsalz – Figure 5d). The nucleation of new grains will enhance grain size sensitive (GSS) flow, which will be counterbalanced by grain growth as they have strain free interiors. If there is an equally contribution of both GSS and GSI flow to the creep rate, suggesting dynamic recrystallization by grain boundary migration, a n-value of 3-4.5 and minor weakening (< 20%) is expected at steady state flow. Since our samples show a much more dramatic weakening when saturated brine is injected (up to 80% for LSS008), we cannot compare the weakening relaxation data to steady state creep shown by De Bresser et al. (2001). Therefore, a quantitative analysis is needed to fully understand the contribution of GSS flow vs. GSI flow to the observed deformation. The strain rate equation can be in the form of:

$$\dot{\varepsilon} = A\sigma^n + B\sigma d^{-p} \qquad (Muhammed, 2015) \qquad (22)$$

Where A and B are constants at a given temperature, n the stress exponent, d the grain size [mm], p is the grain size exponent for dilated wet salt, $A\sigma^n$ represents GSI flow and $B\sigma d^{-p}$ GSS flow. However, not enough data is obtained in this study to adapt this formula for the specific values for A, B and p.

4.1.3 Final remarks

Section 4.1.2. lists the hypotheses that can explain the amount of weakening seen in the experiments in the presence of saturated brine. Hydrolytic weakening cannot explain the enhancement of the dislocation mobility as there is no evidence that intracrystalline water can affect the dislocation mobility in rocksalt. The effect of the saturation difference between the control fluid and the deformed sample is minuscule and cannot account for the total weakening effect. The rapid acceleration in strain rate and increase in stress-strain rate dependence is more likely to be due to the effect of subcritical crack growth, the diminishing of the dislocation density by activating dynamic recrystallization and/or microcracking that leads to stress enhancement and an increased likelihood of grain size sensitive processes like pressure solution. The geometry of the cracks influences the flow of the salt by inhibition of recrystallization along the wide cracks as they are too wide to overcome by diffusive processes.

The obtained n-values for the wet phase of the experiments and the observed microstructures suggest that dynamic recrystallization is the dominant deformation mechanism. However, the n-value of LSS002 and LSS008 during the wet stress-relaxation phases does drop slightly below 3 and the trend seems to continue to drop after the termination of the experiments (Figure 28). Also, the mean grain size of the Leine Steinsalz was reduced (3.2 mm) compared to the undeformed material (Table 3). A smaller grain size promotes the likelihood of pressure solution. Therefore, we can infer that solution-precipitation processes like pressure solution must play a more important role than expected when looking solely at the microstructures. This is in agreement with Ter Heege et al. (2005a), who states

that the documentation of dislocation creep in the microstructures is dominant over the evidence of solution-precipitation creep. Following the pressure solution creep equation (13) and the deformation map of Spiers & Carter (1998) (Figure 30), pressure solution creep is bound to become more important in the wet samples, at the lower strain rates that are seen in nature (10^{-8}-10^{-15} s^{-1}) (Jackson & Talbot, 1986). This is confirmed by calculating the influence of the solution precipitation creep (equation 13) on the total creep rate (equation 14) for the wet phases of the unconfined experiments. At the start of the wet stress-relaxation phase the solution precipitation creep only contributes 0.02% to the total creep rate, while at the end it accounts for approximately 25%. This suggests a smaller contribution of pressure solution than the n-value implies. However, these strain rate equations are established for non-dilatant salt and therefore neglect the influence of microcracking described in this thesis. The same accounts for the presented strain rate equation (22) from Muhammed (2015). He tested natural halite samples with a similar grain size (3-10 mm) for a change in creep behaviour during stress-relaxation after triaxial deformation. He observed a transition in rate-controlling step from dislocation creep (n = 11) to pressure solution (n = 1). These low n-values can be explained by the high confining pressure (50 MPa) and temperature (125°C) during the triaxial experiments, causing the deformation conditions to be in the non-dilatant field and thereby resulting in no intergranular escape of the water (Peach et al., 2001) and enhancing the creep rate as it is temperature driven. Also, the extent of open grain boundaries and transgranular cracks noted in this study could not have been formed in his samples. Therefore, we suggest a total creep equation with dislocation and pressure solution creep that does include the effect of microcracking on the stress and grain size (i.e. inserting equations (19) and (20) in (22)):
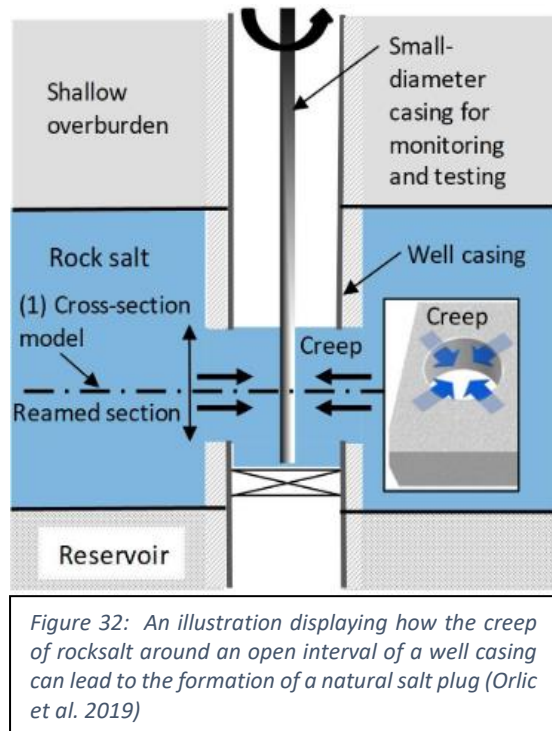
$$\dot{\varepsilon} = A \left(\frac{1}{1-\varphi} \sigma \right)^{n} + B \left(\frac{1}{1-\varphi} \sigma \right) d^{*-p} \tag{23}$$

In which the porosity enhances the stress and microcracking leads to the reduced grain size d^{x}. However, more research is required to quantify and determine the definite interplay between plastic flow, microcracking and solution-precipitation processes in coarse-grained dilated rocksalt e.g. how does the geometry of the cracks influence the grain size exponent p.

4.2   Implications

The transition in deformation mechanism between dry and wet conditions seen in our experimental results is highly important for modelling the sealing capacity of salt layers after disturbance by solution mining or wellbore placement related to oil and gas extraction. During the construction of the wellbore and the active mining, the rocksalt surrounding the openings that mining creates (along the wellbore and cavern walls) tends to be mechanically, geochemically and hydraulically changed (Cai & Kaiser, 2005). This rocksalt becomes damaged and permeable, creating a damage zone around the wellbore. The Hou/Lux model can be used to identify the size and development of these kind of damage zones (Hou, 2003). This model is based on the interplay between diffusion, dislocation creep, strain recovery and hardening, damage and damage healing. Although, the Hou/Lux model can directly predict the extent of the damaged zone and its potential closure, it is only based on the mechanical and hydraulic behaviour of the rocksalt e.g. how confining pressure affects the mechanical closure of cracks. In this thesis, we established that the geochemical environment, i.e. dry or wet, is of importance when describing the crack healing vs crack growth and the creep of the rocksalt. Therefore, the availability of saturated brine, which is commonly present at solution mined caverns, must be taken into account when identifying the damage zones in rocksalt.

Existing models used for assessing cavern and/or wellbore closure must be adjusted for this chemical effect.

Figure 32: An illustration displaying how the creep of rocksalt around an open interval of a well casing can lead to the formation of a natural salt plug (Orlic et al. 2019)

The constitutive models for the creep of rocksalt generally use formulas that combine the dislocation and solution-precipitation creep laws that are respectively represented by a non-linear (i.e. n >> 1) and linear (i.e. n = 1) stress-dependent term. Orlic et al. (2019) modelled the formation of natural salt plugs for well abandonment. In his model part of the casing of the wellbore was removed, allowing for creep of the rocksalt (Figure 32). When the rocksalt touched the smaller monitoring casing, a natural salt plug was considered to be formed. A working salt plug is characterized by a similar porosity and permeability as seen in undeformed rocksalt and accordingly, this plug seals off any remaining fluids from the underlying reservoir. It is important to establish how long this process takes. Therefore, we must fully understand the creep rate and sealing rate of the surrounding rocksalt. To describe the flow of rocksalt in the entire formation, Orlic et al. (2019) used a formula that assumed volume-constant deformation throughout the whole rocksalt formation. This neglects any pre-existing damage and dilatancy; any potential crack formation during the flow of the rocksalt and the possibility that the dilated salt along the wellbore behaves differently than the non-dilatant salt further from the well casing. However, the results in this study do imply that dilated salt behaves differently than intact salt as microcracking enhances the rate of pressure solution (equation 19) and the stress (equation 20). Furthermore, in wet environments the cracks can propagate resulting in larger cracks. These cracks can only be partly healed as they are too wide to overcome by diffusive processes, affecting the creep rate and direction of recrystallization. This implies that during the flow of the dilated rocksalt not all of the microcracks can be healed. Also, because of the low density of gases (and brine) to rocksalt, low effective stresses can develop at the salt plug. These stresses can be low enough to allow semi-brittle deformation and therefore microcracking. Both of the mentioned processes affect the sealing capacity of the salt plug and can result into leakage of the stored fluid which is highly unfavourable. Therefore, (the amount of) microcracking and the geochemical environment must be taken into account when establishing the creep laws. The proposed creep law combines the dislocation and solution-precipitation creep laws including the previous mentioned variables (equation (23)). The creep law can be used and adapted for identifying the damage zones around well bores, predicting the occurrence of cavern instability (i.e. crack growth is dominant) and modelling the formation of a sealing salt plug for well abandonment.

5 Recommendations and future work

5.1 Improvements experimental proceeding

The fluid flow and injection technique must be improved for both the triaxial and unconfined experiments. The set-up of the triaxial experiments contains i.e. glass fibre and Teflon sheets for respectively improving the distribution the fluid flow and preventing the clamping effect. Due to the amount of stress on the sample and thereby on the glass fibre and Teflon sheets, the glass fibre sheets fully fused with the sample, allowing the Teflon sheets to flow into the cracks on top and bottom of the sample. Both of these events lead to complicating getting the fluid into the sample. We recommend to have a total of three glass fibre sheets on both side of the sample.

For the unconfined experiments the vacuum was poor, resulting in a semi-dry environment during the dry stress-relaxation and a non-submerged upper part of the samples during the wet stress-relaxation phase. The top parts of our samples aren't likely to be dry due to capillary suction effects. However, samples with different dimensions could not include these effects. The effect of the room humidity was strongly visible in experiment LSS008, as during the dry stress-relaxation phase the stress dropped significantly more compared to the other two experiments. The room humidity data during the experiment revealed that during the dry phase of LSS008 the room humidity was twice as high as normal (45% vs 30% normally). This must have influence on the results as salt is strongly hygroscopic and we prefer an environment with less than 15% room humidity, which should be achievable by a proper vacuum. To examine only the effect of the saturated brine, this must be solved. Apart from this, a procedure needs to be made for recover samples of unconfined experiments that are only deformed dry as the LSS003 sample crumbled apart after unloading.

5.2 Improvements microstructural work

The microstructural preparation of natural coarse-grained dilated salt is more complex compared to fine-grained synthetic salt due to multiple factors. First, these dilated natural samples have cracks in which dust, older polished material and etching fluid can get stuck in. This results in a secondary polishing effect and thereby damaging the sample or for the latter leaving etching trails throughout the surface. Impregnating the sections totally with epoxy solves this problem partly, as some details along the grain boundaries are lost during the thin sectioning. Also, impregnation of the samples significantly increases the time needed for the microstructural preparation. The natural material used in this study also reacted differently to the etching fluid. This composition of the etching fluid is used before on synthetic samples resulting in an overall transparent section (see Muhammed (2015) and Ter Heege et al. (2005a)), while the older grains of the natural samples become very dark, making a definite interpretation of the internal structure of the grains, therefore the relationship between grains, more complicated. A general overview of the used thin section techniques for dilated coarse-grained rocksalt is given in Appendix A.

5.3 Future work: FTIR tracking of fluid flow

To improve the visualization of the effect of saturated brine on rocksalt samples, deuterium oxide (D_2O) can be added to the control fluid. The benefit of using D_2O is that it is distinguishable from H_2O as their molecule vibration properties, and therefore their infrared spectra, differ. The main vibration wavenumbers for H_2O are ± 3400 cm^{-1} (stretching) and ± 1650 cm^{-1} (bending) and for D_2O ± 2500 cm^{-1} (stretching) and ± 1205 cm^{-1} (bending) (Figure 33) (Chaplin, 2018; Thompson, 1965). The increase of mass of D_2O relative to H_2O results in a decrease in the frequency in vibration and therefore in wavenumber.

Figure 33: The IR spectra of heavy water (D_2O) (blue line), HOD (red line) and H_2O (green line). Each of the peaks corresponds to a vibrational mode of the molecule ((a)symmetrical stretching or bending) (edited after Chaplin, 2018).
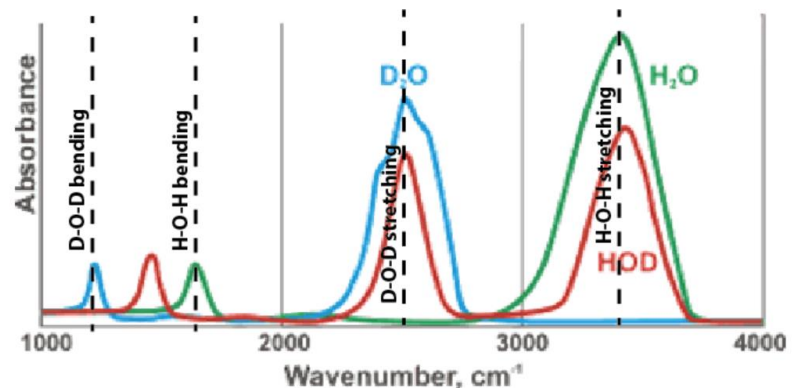
Fourier Transform Infrared (FTIR) Spectroscopy can be used to track the water content and thereby the newly formed microstructures, e.g. fluid inclusions in healed cracks or recrystallized grains. If the fluid inclusions get trapped, it can visualize any recrystallization, precipitation and redistribution of the material induced by the brine which reflects how far the brine penetrated the sample. This infrared microscope analyses the vibrational modes of the sample which absorb the some of the emitted IR radiation, which result into the IR spectra of the sample where the peaks correlates to the vibration of a chemical bond in the sample (de Meer et al., 2005; Moore, 2017).

In addition to FTIR fluid tracking the temperature of the experiments can be elevated to represent the effect of the geotherm on the deformation mechanisms as heat presumably enhances the creep in rocksalt as the mean recrystallized grain size decreases (De Bresser et al., 1998) and the creep rate of pressure solution and dislocation climb and cross-slip will be faster (See equations (11), (12) and (13) and Figure 30). A higher temperature also represents the effect of brine-thermal expansion in abandoned salt caverns. More recrystallization data needs to be obtained to complete the proposed strain rate equation (equation (23)), so it can describe the creep in the sample after saturated brine is injected. This can be done by repeating the experiments at the same temperature, but at different strain rates and/or flow stresses.

6   Conclusions

To investigate the relationship between plastic flow, microcracking and solution-precipitation processes in coarse-grained rocksalt, triaxial and unconfined compaction experiments on coarse-grained Zechstein rocksalt have been conducted at room temperature, a constant loading strain rate and under dry and wet stress-relaxation conditions. The samples were compressed until clear dilation was observed. The flow behavior of dry or wet dilated rocksalt (including injected saturated brine) shows different behavior in terms of mechanical behavior:

- The dry stress-relaxation phase of the dilated rocksalt is characterized by dislocation creep where stress is highly insensitive to strain rate. This can be described by a conventional power law creep equation with the stress exponent of n =9-35. This n-value suggests that dislocation glide is the dominant deformation mechanism in the dry phase.
- There is rapid acceleration in creep of salt and decrease in flow strength if saturated brine is injected. During the wet stress-relaxation phase, the stress exponent n decreased from 10 to 2, suggesting an increase in sensitivity of stress to strain rate. The enhancement in dislocation mobility can most likely be related to the effect of subcritical crack growth, the diminishing of the dislocation density by activating dynamic recrystallization and/or microcracking that leads to stress enhancement and an increased likelihood of grain size sensitive processes like

pressure solution. We suggest a total creep equation with dislocation and pressure solution creep that does include the effect of microcracking on the stress and grain size:

$$\dot{\varepsilon} = A \left(\frac{1}{1-\varphi} \sigma \right)^n + B \left(\frac{1}{1-\varphi} \sigma \right) d^{*-p}$$

- The injection of saturated brine leads to the activation of grain size insensitive (GSI) and grain size sensitive (GSS) processes like fluid assisted dynamic recrystallization and pressure solution. The obtained n-values for the wet phase of the experiments and the observed microstructures suggest that dynamic recrystallization is the dominant deformation mechanism. However, pressure solution is bound to become more important at the lower strain rates seen in nature (10^{-8}-10^{-15} s^{-1}).

- Microcracking can have multiple effects on the creep of rocksalt: (1) It can increase the creep rate of pressure solution with at least an order of magnitude by reducing the grain size, (2) it can enhance the stress by increasing the porosity and (3) the geometry of the cracks (length and crack width suggesting the fluid film thickness) can be too large too overcome by healing mechanisms. The latter refers to that the injection of saturated brine can instantly lead to sub-critical crack behavior. However, as flow stress rapidly decreases in wet settings this would likely be overtaken by the healing mechanisms incorporating diffusive mass transfer at the narrow parts of the cracks.

- Hydrolytic weakening and the effect of the saturation difference between the control fluid and the deformed sample are not likely to influence the dislocation mobility of rocksalt as respectively there is no evidence in the literature that intracrystalline water affects the dislocation mobility and the effect of enhanced solubility is negligible.

- Our proposed total creep equation incorporating the effect of microcracking on the grain size and stress, coupled with how the geometry of the cracks can influence the direction of deformation, demonstrate that the geochemical environment, i.e. dry or wet, is of high importance when describing crack healing vs crack growth in dilated rocksalt. This must be taken into account when predicting the occurrence of cavern instability (i.e. crack growth), identifying the damage zones around well bores and modelling the formation of a sealing salt plug for well abandonment.

- In order to determine the definite interplay between solution-precipitation processes, plastic flow and microcracking more research is needed to quantify the relationship as the number of experiments performed is limited. More experimentation at the same temperature, but at different strain rates and/or flow stresses is needed to adjust the proposed creep law so it can be used for modeling.

7 Acknowledgements

References

Alkan, H., Cinar, Y., & Pusch, G. (2007). Rock salt dilatancy boundary from combined acoustic emission and triaxial compression tests. *International Journal of Rock Mechanics and Mining Sciences*, *44*(1), 108–119. https://doi.org/10.1016/j.ijrmms.2006.05.003

Bérest, P., & Brouard, B. (2003). Safety of Salt Caverns Used for Underground Storage Blow Out ; Mechanical Instability ; Seepage ; Cavern Abandonment, *58*(3), 361–384.

Cai, M., & Kaiser, P. K. (2005). Assessment of excavation damaged zone using a micromechanics model. *Tunnelling and Underground Space Technology*, *20*, 301–310. https://doi.org/10.1016/j.tust.2004.12.002

Carter, N. L., & Hansen, F. D. (1983). Creep of Rocksalt. *Tectonophysics*, *92*, 275–333.

Carter, N. L., Horseman, S. T., Russell, J. E., & Handin, J. (1993). Rheology of rocksalt. *Journal of Structural Geology*, *15*(9–10), 1257–1271. https://doi.org/10.1016/0191-8141(93)90168-A

Chaplin, M. (2018). Water Absorption Spectrum. Retrieved December 10, 2018, from http://www1.lsbu.ac.uk/water/water_vibrational_spectrum.html

De Bresser, J. H. P., Evans, B., & Renner, J. (2002). On estimating the strength of calcite rocks under natural conditions. *Deformation Mechanisms, Rheology and Tectonics: Current Status and Future Perspectives.*, *200*, 309–329.

De Bresser, J. H. P., Peach, C. J., Reijs, J. P. J., & Spiers, C. J. (1998). On dynamic recrystallization during solid state flow : Effects of stress and temperature, *25*(18), 3457–3460.

de Meer, S., & Spiers, C. J. (1997). Uniaxial compaction creep of wet gypsum aggregates Siese de Meer 1 and, *102*(96), 875–891.

de Meer, S., Spiers, C. J., & Nakashima, S. (2005). Structure and diffusive properties of fluid-filled grain boundaries: An in-situ study using infrared (micro) spectroscopy. *Earth and Planetary Science Letters*, *232*(3–4), 403–414. https://doi.org/10.1016/j.epsl.2004.12.030

Gibbs, J. W., & Bumstead, H. A. (1906). *Thermodynamics. Longmans, Green and Company* (Vol. 1).

Griffith, A. A. (1920). The phenomena of rupture and flow in solids. *Royal Sociaty London*, *A 221*, 163–198.

Hangx, S. J. T., Spiers, C. J., & Peach, C. J. (2010). Mechanical behavior of anhydrite caprock and implications for CO2 sealing capacity. *Journal of Geophysical Research: Solid Earth*, *115*(B7), 1–22. https://doi.org/10.1029/2009JB006954

Heidug, W. K. (1991). A thermodynamic analysis of the conditions of equilibrium at nonhydrostatically stressed and curved solid-fluid interfaces. *Journal of Geophysical Research: Solid Earth*, *96*(B13), 21909–21921. https://doi.org/10.1029/91JB02173

Hickman, S. H., & Evans, B. (1991). Experimental pressure solution in halite: the effect of grain/interphase boundary structure. *Journal of the Geological Society*, *148*(3), 549–560. https://doi.org/10.1144/gsjgs.148.3.0549

Hou, M. Z., Xie, H., & Yoon, J. S. (2010). *Underground Storage of CO2 and Energy*. Leiden.

Hou, Z. (2003). Mechanical and hydraulic behavior of rock salt in the excavation disturbed zone around underground facilities. *International Journal of Rock Mechanics and Mining Sciences*, *40*(5), 725–738. https://doi.org/10.1016/S1365-1609(03)00064-9

Houben, M. E., ten Hove, A., Peach, C. J., & Spiers, C. J. (2013). Crack healing in rocksalt via diffusion in adsorbed aqueous films: Microphysical modelling versus experiments. *Physics and Chemistry*

of the Earth, *64*, 95–104. https://doi.org/10.1016/j.pce.2012.10.001

Hunsche, U., & Hampel, A. (1999). Rock salt - the mechanical properties of the host rock material for a radioactive waste repository. *Engineering Geology*, *52*(3–4), 271–291. https://doi.org/10.1016/S0013-7952(99)00011-3

Jackson, M. P. A., & Talbot, C. J. (1986). External shapes , strain rates , and dynamics of salt structures. *Geological Society of America Bulletin*, *97*(March), 305–323.

Kim, H., Rutqvist, J., Ryu, D., Choi, B., & Sunwoo, C. (2012). Exploring the concept of compressed air energy storage (CAES) in lined rock caverns at shallow depth : A modeling study of air tightness and energy balance, *92*, 653–667. https://doi.org/10.1016/j.apenergy.2011.07.013

Koelemeijer, P. J., Peach, C. J., & Spiers, C. J. (2012). Surface diffusivity of cleaved NaCl crystals as a function of humidity: Impedance spectroscopy measurements and implications for crack healing in rock salt. *Journal of Geophysical Research: Solid Earth*, *117*(1), 1–15. https://doi.org/10.1029/2011JB008627

Langer, M. (1999). Principles of geomechanical safety assessment for radioactive waste disposal in salt structures. *Engineering Geology*, *52*(1), 257–269. https://doi.org/10.1016/0304-4165(65)90244-8

Lux, K.-H. (2009). Design of salt caverns for the storage of natural gas, crude oil and compressed air: Geomechanical aspects of construction, operation and abandonment. *Geological Society, London, Special Publications*, *313*, 93–128. Retrieved from https://doi.org/10.1144/SP313.7

Moore, E. (2017). *Fourrier Transform Infrared Spectroscopy (FTIR): Methods, Analysis and Research Insights*. (E. Moore, Ed.). New York: Nova Science Publishers, Inc.

Muhammad, N. (2015). *Deformation and transport processes in salt rocks : An experimental study exploring effects of pressure and stress relaxation*.

Orlic, B., Wollenweber, J., Geel, C. R., Van de weijer, V. P., … Ter Heege, J. H. (2019). Formation of a sealing well barrier by the creep of rock salt : numerical investigations. *American Rock Mechanics Association*, 1–7.

Peach, C. J. (1991). *Influence of deformation on the fluid transport properties of salt rocks*. Utrecht University.

Peach, C. J., & Spiers, C. J. (1996). Influence of crystal plastic deformation on dilatancy and permeability development in synthetic salt rock. *Tectonophysics*, *256*, 101–128. https://doi.org/10.1016/0040-1951(95)00170-0

Peach, C. J., Spiers, C. J., & Trimby, P. W. (2001). Effect of confining pressure on dilatation, recrystallization and flow of rock salt at 150 C. *Journal of Geophysycal Research*, *106*, 13,315-13,28.

Pijnenburg, R. P. J., Verberne, B. A., Hangx, S. J. T., & Spiers, C. J. (2018). Solid Earth Deformation Behavior of Sandstones From the Seismogenic Groningen Gas Field : Role of Inelastic Versus Elastic Mechanisms. *Journal of Geophysical Research*, *123*. https://doi.org/10.1029/2018JB015673

Pluymakers, A. M. H., & Spiers, C. J. (2014). Compaction creep of simulated anhydrite fault gouge by pressure solution : theory v . experiments and implications for fault sealing. *Rock Deformation from Field, Experiments and Theory: A Volume in Honour of Ernie Rutter. Geological*, *i*, 107–124.

Poirier, J.-P. (1985). *Creep of crystals: high-temperature deformation processes in metals, ceramics and minerals*. Cambridge University Press.

Popp, T., Kern, H., & Schulze, O. (2001). Evolution of dilatancy and permeability in rock salt during hydrostatic compaction and triaxiai deformation vary between initial permeability is primarily proach the in situ matrix permeability The pore space sensitivity of P and resulting in relatively. *Journal of Geophysical Research*, *106*, 4061–4078.

Renard, F., Park, A., Ortoleva, P., & Gratier, J. (1999). An integrated model for transitional pressure solution in sandstones, *312*, 97–115.

Rutter, E H, Atkinson, B. K., & Mainprice, D. H. (1978). On the use of the stress relaxation testing method in studies of the mechanical behaviour of geological materials, 155–170.

Rutter, Ernest H, & Mainprice, D. (1978). The Effect of Water on Stress Relaxation of Faulted and Unfaulted Sandstone. *Pure and Applied Geophysics*, 635–654. https://doi.org/10.1007/BF00876530

Schutjens, P. M. T. M., & Spiers, C. J. (1999). Intergranular pressure solution in NaCl: Grain-to-grain contact experiments under the optical microscope. *Oil and Gas Science and Technology*, *54*(6), 729–750. https://doi.org/10.2516/ogst:1999062

Silberschmidt, V. G., & Silberschmidt, V. V. (2000). Analysis of cracking in rock salt. *Rock Mechanics and Rock Engineering*, *33*(1), 53–70. https://doi.org/10.1007/s006030050004

Sinn, C. J. A., Giacomel, P., Peach, C. J., & Spiers, C. J. (2018). Effects of Plastic Deformation on the Transport Properties of Rocksalt, (1).

Spiers, C., de Meer, S., Niemeijer, A., & Zhang, X. (2004). Kinetics of rock deformation by pressure solution and the role of thin aqueous films. *Frontiers Science Series*, 129–158.

Spiers, C. J., & Carter, N. L. (1998). Microphysics of rocksalt flow in nature. *Fourth Conference on the Mechanical Behavior of Salt*.

Spiers, C. J., Schutjens, P. M. T. M., Brzesowsky, R. H., Peach, C. J., … Zwart, H. J. (1990). Experimental determination of constitutive parameters governing creep of rocksalt by pressure solution. *Geological Society, London, Special Publications*, *54*(1), 215–227. https://doi.org/10.1144/GSL.SP.1990.054.01.21

Sutherland, H. J., & Cave, S. P. (1980). Argon gas permeability of New Mexico rock salt under hydrostatic compression. *Int. J.Rock Mech. Min. Sci. Geomech.*, Abstr., 17: 281-288.

Ter Heege, J. H., De Bresser, J. H. P., & Spiers, C. J. (2005a). Dynamic recrystallization of wet synthetic polycrystalline halite: Dependence of grain size distribution on flow stress, temperature and strain. *Tectonophysics*, *396*(1–2), 35–57. https://doi.org/10.1016/j.tecto.2004.10.002

Ter Heege, J. H., De Bresser, J. H. P., & Spiers, C. J. (2005b). Rheological behaviour of synthetic rocksalt: The interplay between water, dynamic recrystallization and deformation mechanisms. *Journal of Structural Geology*, *27*(6), 948–963. https://doi.org/10.1016/j.jsg.2005.04.008

Thompson, W. . (1965). Infra-Red Spectroscopic Studies of Aqueous Systems. *Trans. Faraday Soc.*, *61*, 2635–2640.

Trimby, P. W., Drury, M. R., & Spiers, C. J. (2000). Recognising the crystallographic signature of recrystallisation processes in deformed rocks: A study of experimentally deformed rocksalt. *Journal of Structural Geology*, *22*(11–12), 1609–1620. https://doi.org/10.1016/S0191-8141(00)00059-6

Urai, J. L., Schléder, Z., Spiers, C. J., Kukla, P. A., … Röhling, H.-G. (2008). Flow and Transport Properties of Salt Rocks. *Geo 2008; International Conference and 106th Annual Meeting of the Deutsche Gesellschaft Für Geowissenschaften e. V. (DGG) and 98th Annual Meeting of the Geologische Vereinigung e.V. (GV)*, *60*, 61. https://doi.org/978-3-540-85085-4

Urai, J. L., Spiers, C. J., Zwart, H. J., & Lister, G. S. (1986). Weakening of rock salt by water during long-term creep. *Nature*, *324*(11), 554–557. https://doi.org/10.1038/324227a0

Urai, J., & Spiers, C. (2007). The effect of grain boundary water on deformation mechanisms and rheology of rocksalt during long-term deformation. *The Mechanical Behaviour of Salt— …*, (May), 22–25. https://doi.org/10.1139/X10-011

van Noort, R., Visser, H. J. M., & Spiers, C. J. (2008). Influence of grain boundary structure on dissolution controlled pressure solution and retarding effects of grain boundary healing. *Journal of Geophysical Research: Solid Earth*, *113*(3), 1–15. https://doi.org/10.1029/2007JB005223

Visser, H. J. M., Spiers, C. J., & Hangx, S. J. T. (2012). Effects of interfacial energy on compaction creep by intergranular pressure solution: Theory versus experiments on a rock analog (NaNO3). *Journal of Geophysical Research B: Solid Earth*, *117*(11), 1–15. https://doi.org/10.1029/2012JB009590

Weertman, J., & Weertman, J. R. (1970). Mechanical properties, strongly temperature dependent, chapter 16. *Physical Metallurgy*, 793–819.

Zhang, X., & Spiers, C. J. (2005). Compaction of granular calcite by pressure solution at room temperature and effects of pore fluid chemistry. *International Journal of Rock Mechanics and Mining Sciences*, *42*(7-8 SPEC. ISS.), 950–960. https://doi.org/10.1016/j.ijrmms.2005.05.017

Appendix A: Thin sectioning of dilated coarse-grained rocksalt

This appendix describes the preferred method to thin section dilated coarse-grained rocksalt. It is important to immediately section your sample after deformation, so the deformation does not continue after the experiment. Also, keep a record of its height, length and how the sample is cut and mark the sample to make sure that the deformation and/or flow direction is clearly visible.

1. Preparation

The deformed sample must be brought to a low humidity room (<20%) to reduce the effect of atmospheric water on the sample. The workspace should be clean so dust will not get stuck on your thin section and ruin the polish. Put on latex gloves to avoid any water contamination and remove the deformed sample from its jacket.

2. Preliminary cutting process: metallurgical saw

First, the sample can be divided into three parts: section 1 and 3 are sliced vertically (along the length) and section 2 is sliced horizontally (perpendicular to the length) (Figure A.1). Cutting your sample like this, will give you a better understanding how the fluid affects the salt as section 1 and 3 give insight on the large vertical cracks and on the effect of upstream and downstream and section 2 shows the crack distribution in the σ_3 direction (related to confining pressure). These sections are made by using a metallurgical band saw. This saw slices the sample with a high velocity, creating a large damage zone and even causing grains to pop off if the sample is not stable. The metallurgical band saw cannot be replaced with the diamond saw for this step as the whole sample is too heavy for the diamond saw. This can cause the diamond saw to become crooked, so this is highly discouraged. By cutting the sample in three sections with a length of 40 mm and a diameter of 51 mm, the sections are light enough to be placed on the screw-grip holder of the diamond saw (step 4).
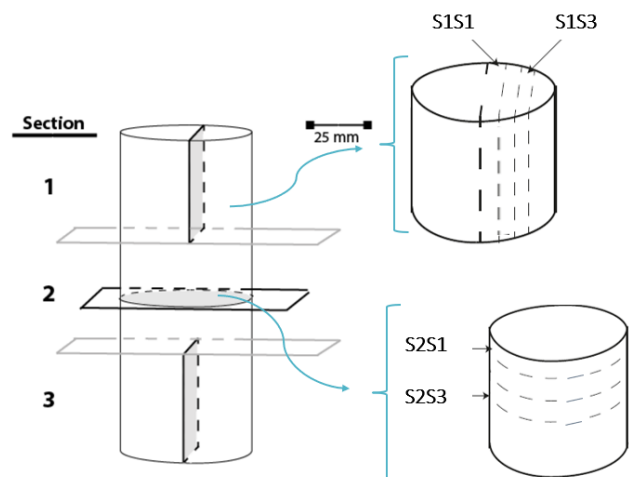

Figure A.1: Orientations of the sections concerning the microstructural preparation. Section 1 and 3 involve vertical cuts and section 2 horizontal. S1S1 indicates the first slice of the section 1 and S1S2 the second slice etc.

3. Impregnation of the cracks

For dilated coarse-grained rocksalt it is highly recommended to epoxy all sections, even if the sample is stable i.e. no grains are popping off. Otherwise, when polishing the samples small polished-off salt will get stuck in the cracks. This leads to a secondary polishing effect in step 5 as the polished-off salt is coarser than the next polishing paper and therefore it damages the polish.

The epoxy used in the HPT Lab at Utrecht University is Araldite2020, with components A and B mixed in a 100:30 ratio. You must add a miniscule amount of blue colorant in the epoxy for creating a contrast between the added epoxy and the sample as both are translucent. Curing take about 24 hours. You can impregnate the sections with epoxy resin in two ways: surface epoxy and total epoxy (Figure A.2)

Figure A.2: Two ways to apply epoxy on your sample: surface epoxy and total epoxy.

In this study, we preferred to use total epoxy as the surface epoxy did not attach perfectly to the surface of the section as salt is hygroscopic. After applying the epoxy, the sections must be placed in a vacuum chamber to extract the remaining air from the sample and fill most of the cracks with epoxy. A vacuum chamber is not needed for surface epoxy as component B will become volatile in the vacuum chamber. This leads to the not setting of the epoxy. A disadvantage of using epoxy is that it is harder than rocksalt, resulting in a significant increase in needed time to slice the sections with the diamond saw.

4. Cutting thin sections: diamond saw

Check when mounted if the surface of the section is straight, otherwise the slice will get a depth difference if it lies down, making an overview picture with the microscope difficult as the image will become unclear. If the surface is not straight, you can pre-polish the section by using the coarsest polishing paper (P120). After mounting the section in a screw-grip holder, fill up the container beneath the saw with evaporating oil (*Fenela VD 201 N*). The oil serves as a lubricant and cleans the surface of the section. This way, no grains can block the saw. The diamond saw must be used on low velocity to minimize the damage zone. The saw can make thick slices of approximately 5 mm thick, which are sturdy enough to support their own weight. Therefore, the sections do not have to be placed on a glass plate.

Figure A.3: Making the thin sections of the sample using the diamond wafering blade, which cleans itself by rotating in the evaporating oil filled container at the bottom of the apparatus.

5. Polishing

The polishing stage includes three steps: (1) low and high grade carborundum (SiC) papers (P120 up to P4000), (2) micropolish (Buehler) and (3) diamond oil suspension (MetaDi Oil) with respective grain sizes of 0.3 µm and 0.25-1.0 µm (Muhammad, 2015). The low grade SiC polishing papers (P120-P600) are used for rough polishing e.g. if the damage zone is large and the high grade papers (P800-P4000) are used for perfecting the polish work. Start by using the low grade papers and slowly change into the high grade papers. You can go up to 5 times over the same area of your polishing paper as otherwise you would polish with the pollished-off salt instead of the grid of the paper. When switching between papers, you have to clean the surface with evaporating oil to prevent any secondary polishing effects. You can choose between two polishing techniques for minimizing the amount of scratches:

making a '8' figure with the sample (Figure A.4a) or polish in a straight line and turn the sample or the polishing direction 90º when switching between polishing grades (Figure A.4b). It is important to know how much damage each polishing paper does to your surface and to get a feel how little force you have to use when polishing (especially when switching from P2500 to P4000). If you know this, then you can directly identify when something is wrong with the polishing work.
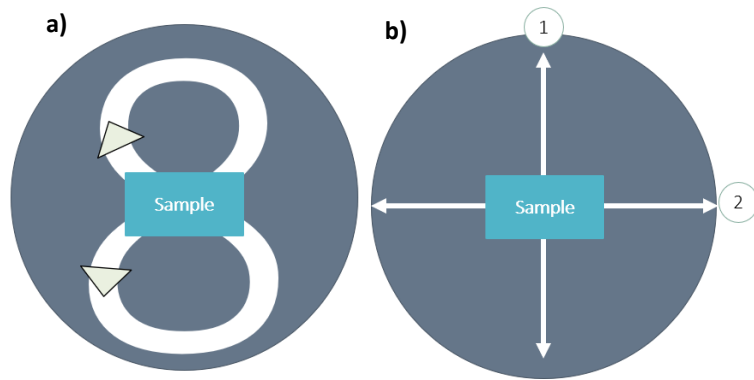

Figure A.4: The two polishing techniques on a SiC polishing paper: a) Making the '8' figure and b) Changing the polishing direction 90º when switching between polishing papers.

After the P4000 polishing paper the polishing work can be perfected by using micropolish powder and/or diamond oil suspension. When using the micropolish, it is suggested to add some evaporating oil to the micropolish to make a polishing paste and use a deconstructed latex glove as polishing cloth. This way, the polishing can be controlled more as normally the powder will fall off to quickly. The use of diamond oil suspension is not thoroughly used in this study, but it can be used in the same way as the micropolishing powder. Do not forget to clean the surface with hexane when switching to between the different polishing grades of the diamond oil suspension (as the used substances are now oil based).

6. Etching

Etching is used for optimizing the microstructures and make structures like subgrains, grain boundaries and fluid inclusions easier to identify (Figure A.5). It removes the damaged surface layer and etches the boundaries. Following the method described by Muhammed (2015) and ter Heege (2005a) the etching fluid consists of 95% saturated NaCl solution + 5% de-ionized water containing ±8g/l $FeCl_3·6H_2O$. The etching fluid is applied to the salt surface for 15 seconds and immediately rinsed thoroughly with hexane. Subsequently, the thick sections are dried with compressed air.
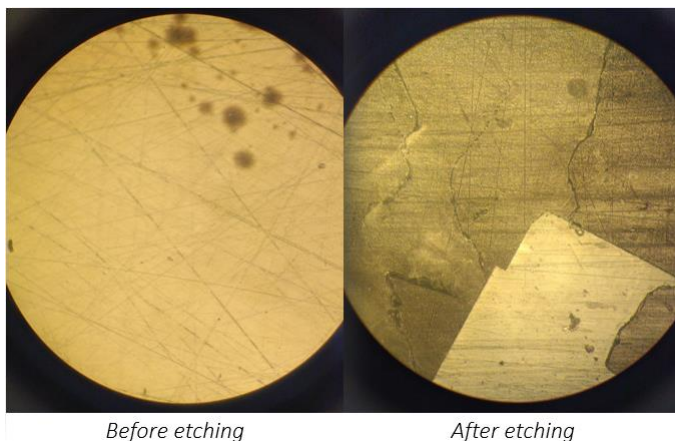

Before etching   *After etching*

Figure A.5: The two photos are taken from the same area in LSS001 and display the effect of etching e.g. fluid inclusion trail and sharp grain boundaries.